ABSTRACT

A Study of Frost Growth and Roughness
on a Cold Flat Plate under Forced Convection

Tongxin Zhang, Ph.D.

Mentor: Dennis L. O'Neal, Ph.D.

The growth and roughness of frost formed on a cold flat plate under forced convection was characterized through experimental observations and analysis. The results indicated that the evolution of frost roughness was mainly determined by the complex structures of frost crystals appearing on the top of the frost layer. The frost crystal type, frost crystal size, and frost crystal distribution were strongly affected by environmental conditions and collectively determined the formation of frost surface roughness.

Frost roughness parameters, including frost root-mean-square height and frost surface skewness, were measured by utilizing a 3-D photogrammetric method. The growth of frost roughness under various environmental conditions were then assessed. Both frost root-mean-square height and surface skewness increased with time until reaching a maximum value (up to 0.69 mm and 2.34, respectively), before starting to decrease. The frost surface skewness peak, the maximum frost root-mean-square height, and the time for the appearance of frost root-mean-square height typically varied linearly with the surrounding environmental conditions.

The experimental investigation also showed that frost roughness varied over both time and location on the test surfaces. The frost equivalent sand-grain roughness height, calculated by using the frost root-mean-square height and frost surface skewness, was applied to represent the unevenness of frost roughness on cold substrates. Through an ANOVA test on the data of the frost equivalent sand-grain roughness height, air humidity and air temperature with p-values less than 0.05 were indicated to be the key factors determining the changes in the variation of the frost roughness in space. Empirical correlations were developed to describe the relationships between the appearance of the frost roughness peak and environmental conditions.

Finally, based on the frost roughness data collected in this study, a predictive model of frost roughness parameters, including frost root-mean-square height, frost surface skewness, and frost equivalent sand-grain roughness height, was established with the R-square values of 0.57, 0.65, and 0.53, respectively.

A Study of Frost Growth and Roughness on a Cold Flat Plate under Forced Convection

by

Tongxin Zhang, B.S., M.S.M.E

A Dissertation

Approved by the Department of Mechanical Engineering

_____

Paul Ro, Ph.D., Chairperson

Submitted to the Graduate Faculty of
Baylor University in Partial Fulfillment of the
Requirements for the Degree
of

Doctor of Philosophy

Approved by the Dissertation Committee

_____

Dennis L. O'Neal, Ph.D., Chairperson

_____

Stephen T. McClain, Ph.D.

_____

Kenneth Van Treuren, Ph.D.

_____

David Jack, Ph.D.

_____

Truell Hyde, Ph.D.

Accepted by the Graduate School

May 2020

_____

J. Larry Lyon, Ph.D., Dean

Page bearing signatures is kept on file in the Graduate School.

TABLE OF CONTENTS

LIST OF FIGURES

LIST OF TABLES

ACKNOWLEDGMENTS

First and foremost, I would like to express gratitude to my mentor Dr. Dennis O'Neal. I thank him for opening his lab to me and offering me a chance to learn and grow as an engineer at Baylor University. I'm particularly grateful that he always makes himself available to me, guiding me through every difficult time of this project. I would also like to thank Dr. Stephen T. McClain, who provided me the opportunity to participate in the study of frost roughness. I am very thankful for his kind support and encouragement along this journey.

My sincere appreciations go to the committee members, Dr. David Jack, Dr. Kenneth Van Treuren, and Dr. Truell Hyde for their valuable suggestions and comments on this project. My appreciation also goes to Dr. Douglas Smith, Dr. Jill Klentzman, Dr. Yue Ling, and Dr. Lesley Wright for their help and attention inside and outside their classes.

There are many other people in the department of mechanical engineering that I want to say thanks to: Dr. Carolyn Skurla, Jodi Branch, Sara Baker, Taber Miyauchi, Zhaigui Wang, and Juan Cornejo, thanks everyone for the generous assistance and support to me and my research at various junctures.

Finally, I would like to give my heartfelt appreciation to my parents, my sister, my wife, my in-laws and my son for their uncompromising love and encouragement. Without their support, it would have been impossible for me to study abroad or complete this project. My love is with you all.

DEDICATION

To my dear parents, sister, wife, and son,
for their unconditional love and support.
谨以此献给我挚爱的父母、姐姐、妻子和儿子，感恩你们一路的相伴！

CHAPTER ONE

Introduction

Frost formation is a common phenomenon in nature as well as in engineering systems. When moist air contacts a cold surface that is below 0˚C, frost may deposit on the surface. For most engineering applications, the occurrence of frosting is undesirable. For example, increased frost thickness between heat exchanger fins results in an increase of thermal resistance between the fins and the air and additional restrictions in the airflow between the fins [1]. The additional roughness due to frost on a wing surface of an aircraft could cause an increase in the drag and affect the aerodynamic performance of the wing [2]. Over the past 70 years, many researchers have investigated frost formation and gained a better understanding of the nature of this phenomenon, particularly in refrigeration and heat pump systems. Studies [3-16] indicated that wall temperature (T_s), air velocity (V_{air}), relative humidity (RH), and air temperature (T_{air}) had primary impacts on the growth of frost deposited on cold surfaces.

Frost formation on a cold substrate usually starts with the condensation of water droplets and subsequent freezing of these super-cooled droplets. The diameter of condensate droplets decreases with decreasing cold wall temperatures and air humidity [17]. Subsequently, initial frost crystals emerge from the frozen condensate droplets. The geometries of these crystals vary according to the ambient cold wall temperature and air humidity [17-19]. As the frost crystals continue to grow and interconnect with each other, a porous frost layer with a rough surface eventually forms. During the process of frost

growth, the total amount of water vapor flowing toward the frost layer is divided into two parts. A portion of the water vapor condenses and deposits on the frost surface and increases the frost thickness. The other portion crosses the frost surface and diffuses into the inner frost layer and increases the frost density [20-25]. As a result, both frost thickness and density increase over time.

With the development of better optical technologies, researchers began investigating the variation of frost properties with respect to frost crystal structure [4, 26, 27]. Their results indicated that frost growth can be strongly influenced by the initial porosity of the frost layer [26] and present different growth rates corresponding to the variations of the frost crystal growth direction [27]. Compared to plate-type crystals which form on surfaces at high wall temperatures (e.g. -8.5˚C and above), column-shaped crystals that grow on surfaces at low surface temperatures (e.g. -14.3˚C and below) allow easier heat conduction and lead to a higher frost thermal conductivity [4]. For example, at 15 min, the thermal conductivity of frost formed under surface temperature of -14.3˚C was about 0.8 W/(mK) while that of frost growing under wall temperature of -8.5˚C was about 0.5 W/(mK) [4]. Thus, it can be concluded that frost crystal type plays an important role in the evolution of the frost layer and frost properties. Although the formation of frost crystal type has been widely investigated, the variations of other frost crystal features, such as frost crystal size and distance, have been rarely documented. Furthermore, the impacts of frost crystal structure on frost roughness formation are not well understood.

In engineering systems including evaporators, piping, and aircraft, frost roughness can have significant effects on fluid flow and heat transfer. Frictional forces generated by

the interactions between the air stream and the rough frost surface can restrict airflow across the surface [1, 28]. Frost roughness can also increase turbulence levels of air on a frost surface and further influence heat and mass transfer [1]. Moreover, the additional roughness due to frost on a wing surface of an aircraft could cause an increase in the drag and affect the aerodynamic performance of the wing [2, 29, 30]. All of these effects can result in a substantial reduction in engineering system efficiency or even safety. Therefore, it is essential to understand frost roughness growth behavior and accurately predict frost roughness on frosted surfaces.

Unfortunately, few investigations have focused on quantifying frost surface roughness. One potential reason may be due to the delicate, temperature-sensitive and partially transparent structure of frost. Any physical contact with the frost surface would damage the frost surface. Chen and Rohsenow [1] took surface images of frost growing on an optical transparent pipe. Through comparisons between the frost images and sand grain sizes, a correlation between the frost roughness and equivalent sand roughness was qualitatively established. The authors then developed a relationship between frost thickness and frost equivalent sand roughness. Later, Yun et al. [31] measured the frost height difference between frost peaks and valleys by using a micrometer with a thin needle under the help of a magnification system. An empirical correlation of frost roughness was developed as a function of time only. Furthermore, their correlation had several limitations due to the small range of experimental conditions, its high standard deviation (±29%), and lack of information related to the impacts of environmental conditions [31]. Another method of frost roughness measurement was based on lateral side 2D frost surface profiles generated during frost thickness measurements [32].

However, the 2D lateral side surface profiles provide overlapped views of frost formed at different distances from the camera which might not accurately represent the actual distribution of frost crystals over the frost surfaces.

Recently, Miyauchi et al. [33] developed a measurement method using structure-from-motion photogrammetry [34]. This technique was nonintrusive and provided an in-situ measurement of the frost roughness on a closed-loop psychrometric wind tunnel. This nonintrusive approach did not impose effects on the frost surface, structure, or temperature when frost was grown over a wide range of environmental conditions. Frost root-mean-square (RMS) height, frost skewness, and frost equivalent sand-grain roughness height can be calculated from the spatial geometry data of the frost surface model. This 3-D photogrammetric method was applied in this study.

The purpose of this study was to characterize the frost roughness evolution formed on a cold flat plate under forced convection. To satisfy this objective, a series of experiments were performed using a closed-loop psychrometric wind tunnel. A digital microscopy system was used to monitor and record frost forming on a small aluminum surface. The variation of environmental parameters, including wall temperature (T_s), air velocity (V_{air}), relative humidity (RH), and air temperature (T_{air}), were evaluated. Frost roughness was analyzed from the perspective of frost crystal structure to reveal its growth mechanism and trends. The impacts of environmental conditions on frost roughness evolution were also explored. In the end, an empirical model for estimating frost growth and frost roughness was established. Collectively, this research should increase the overall understanding of frost roughness formation on a cold flat plate. It is also

anticipated that this research will eventually contribute towards both characterizing the mass and heat transfer or the aerodynamic performance of frosted surfaces.

This dissertation is divided into seven chapters. Chapter Two provides a review of supporting pertinent literature. Chapter Three presents the characteristics of frost crystal formation in the initial period of frosting. Next, Chapter Four outlines the general mechanism of frost roughness evolution from the perspective of frost crystal structure variation. Chapter Five then describes the uniformity of frost roughness growth over the cold test surface. Chapter Six provides an empirical model for predicting frost roughness formed on a cold flat plate. Finally, Chapter Seven provides the overall conclusions and recommendations for future work.

CHAPTER TWO

Literature Review

Frost forming on cold metal surfaces is an undesirable phenomenon in refrigeration, heat pumps, aerospace, and other engineering systems. A wide range of studies have been conducted by researchers to characterize the fundamental mechanisms affecting frost growth. In this section, three areas relevant to this study will be reviewed: frost formation mechanisms, frost crystal shapes, and frost roughness.

Frost Formation Mechanisms

Most investigators have treated the frost layer as a porous medium in which water vapor from the air diffuses into the frost layer during the growth of the frost. During this transient process of frosting, heat and mass transfer occur simultaneously. Brian et al. [20], Jones and Parker [21], Tao et al. [22], Le Gall et al. [23], El Cheikh and Jacobi [24], Breque and Nemer [25] assumed the total amount of water vapor flowing toward the frost layer is divided into two parts: one directly deposits on the frost surface and increases the frost thickness, and the other crosses the frost surface into the inner frost layer and thickens the frost density (as shown in Figure 2.1). As a result, both frost thickness and density increase over time.

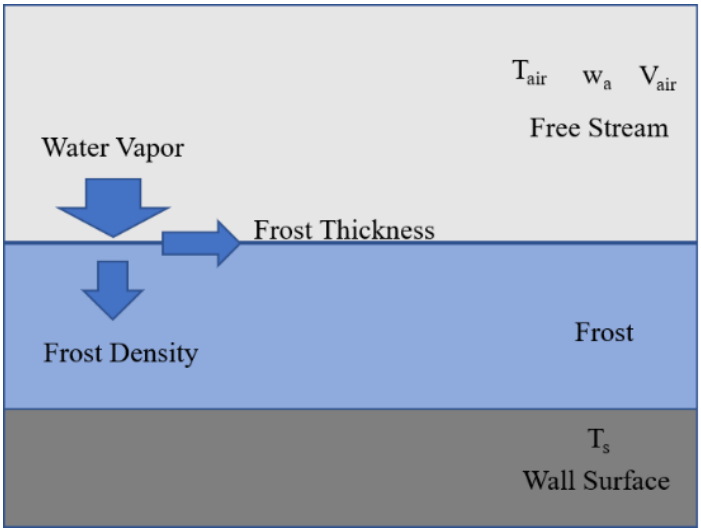

Figure 2.1. Diagram of the frosting process.

To better characterize frost formation, researches usually divide the whole transient frosting process into several periods. Hayashi et al.[19] studied frost formation on a cold flat plate under forced convective flow and proposed a three-period model of frost growth (see Figure 2.2): (a) crystal growth, with frost nucleation and growth in the direction vertical to the cold wall surface; (b) frost layer growth, when frost crystals expand in multiple directions and interact with other crystals and (c) fully developed frost layer growth when the top part of frost reaches frost melting temperature (0˚C) and eventually frost growth stops. During the process of frosting, two frost growth patterns may be observed [6], monotonic growth and cyclic growth. The latter growth pattern usually occurs in cases in which the wall temperature is below -10˚C and air humidity is above 50%. Frost melting on the frost surface generates tiny water droplets that penetrates into the frost layer. The frost thermal resistance is reduced because of an increase in frost density when this liquid refreezes inside the frost matrix. As a result, the frost surface temperature drops and the frost begins to grow again.

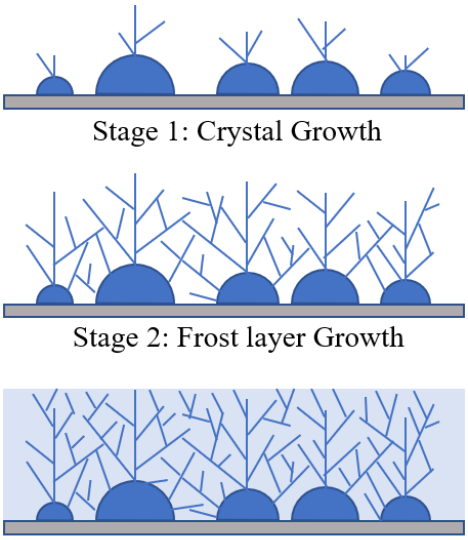

Figure 2.2. Process of frost formation

In the past 70 years, the dependence of frost growth under different atmospheric and surface conditions has been investigated extensively, specifically on flat plates. Researchers [3-16] indicated that air humidity, air velocity, wall temperature, and air temperature had primary impacts on the microstructure and properties of frost deposited on a cold surface. The effects of these parameters on frost growth, however, could vary by an order of magnitude. Moreover, data provided by the previous studies [4-6] reveal that key parameters affecting frost growth are the cold wall temperature and air humidity. Typically, lower cold wall temperatures mainly affect frost thickness, while higher absolute humidity leads to both higher frost thickness and density. In terms of the role played by other parameters, conclusions pertaining air velocity effects are inconsistent from different studies. O'Neal and Tree [7] and Lee et al. [8] observed that frost thickness increases with air velocity until the Reynolds number reaches a critical value: 15900 for O'Neal and Tree and 17000 for Lee et al. Östin & Andersson [6] and Tokura et al. [9], however, concluded that increasing air velocity turned out not to affect frost

thickness growth, but only increases frost density. Similar inconsistencies are reported for the effects of air temperature. With the absolute humidity kept constant, a thinner and denser frost layer was observed at a higher air temperature [4, 10-12], while others found that there was no appreciable effect of air temperature on frost thickness [7, 13]. It was also found that under a constant relative humidity, frost thickness increases with air temperature in a case with a lower air velocity (2.3 m/s compared to 5.3 m/s) [14]. However, when relative humidity gets close to 80%, frost thickness only increases slightly with air temperature [4]. All in all, the fundamental mechanism of frost formation is still not fully understood.

Frost was found to form unevenly on the test surfaces when frosting experiments are conducted on cold flat plates under forced convection [8, 14, 35-38]. Thus, frost properties, such as frost thickness, frost density, and frost thermal conductivity, would vary at different locations of the test surfaces. At the leading edge of the cold plate, frost crystals would grow in a radial direction to form a frost layer with a ‘round head’. This part of the frost had a rather smooth profile, a smaller frost thickness, and a large frost density [14]. On the other hand, frost crystals would grow approximately at the same rate to form a uniform thickness in the downstream region of the test surface [14]. Researchers tried to capture the spatial variation of frost properties through some frost modeling [35-38]. The results from these frost models indicated that the water vapor mass fraction was higher near the leading edge of the cold substrate surfaces. The moist air was cooled to create a faster phase change mass transfer, which created a denser frost. In the downstream region, the gradient of air humidity was smaller compared to that in the front, which generated a lower frost density. Furthermore, frost thermal conductivity

was unevenly distributed along the cold surface due to the frost density variations by location [38].

Surface wettability of a substrate has been proven to play an important role in frost formation [39-41]. The surface wettability is represented in terms of the water static contact angle (SCA). A surface is called hydrophilic if it has a water SCA less than 90° (see Figure 2.3). On the contrary, if a surface has a water SCA greater than 90°, it is defined as a hydrophobic substrate. A hydrophilic surface has lower surface energy than a hydrophobic substrate [42]. Na and Webb [39] hypothesized that the surface energy could affect the frost nucleation through changing the supersaturation degree of air at the cold surface. They found that a higher supersaturation degree was required for frost nucleation on a surface with lower surface energy. Shin et al. [40] experimentally studied the effects of surface energy on frost formation. The author pointed out that the frost density and the thermal conductivity increased as the SCA of the tested surface raised from 23° to 88°. A higher frost thermal conductivity could result in a faster frost growth on hydrophilic surfaces than that on hydrophobic substrates during the fully developed period of frost formation [41].

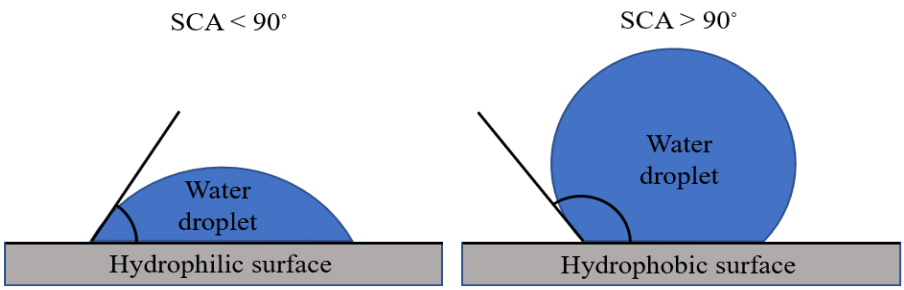

Figure 2.3. SCAs of hydrophilic and hydrophobic surfaces

With the development of advanced materials, hydrophobic surfaces have been evaluated for their potential to retard frost formation. Cai et al. [43] applied hydrophobic

coatings and hygroscopic coatings on regular copper surfaces and compared their abilities to disrupt the frost formation process. Their results demonstrated a measurable effect of these coatings on the initial growth of frost. The growth of frost formed on these coated surfaces was delayed and smaller frost heights were produced. There was also a sparser distribution of frost crystals. Liu et al. [44] observed the progress of frost deposition on a cold hydrophobic substrate where SCA with water droplets was 162°. Compared to the conventional copper surface, the hydrophobic surface showed a strong ability to retard frost formation. The frost layer structure formed on the hydrophobic surface did not adhere to the surfaces well as on the copper surface and was easier to be removed.

A number of models [25, 26, 45-58] of frost formation have been presented and reviewed in the literature, including mathematical models based on the conservation of mass and energy principles, and empirical correlations obtained from experimental data. Léoni et al. [45] conducted a review on the predictive methods of frost thickness and density from previous literature. A thickness database was given as shown in Table 2.1. The range of these experimental conditions was quite wide: air temperatures (T_{air}) from -8˚C to 25˚C, wall temperatures (T_s) from -30˚C to -4˚C, air velocities (V_{air}) from 0.18 m/s to 6.00 m/s, and relative humidities (RH) from 12% to 80%. It can be concluded that a reliable prediction of frost thickness can usually be obtained under low wall temperatures (examples were given at T_w = -7.0˚C and T_w = -19.9˚C), and high air velocities (examples were given at V_{air} = 2.6 m/s and V_{air} = 5.7 m/s). On the other hand, experimental data for frost density are better predicted at lower air velocities and lower wall temperatures. Additionally, most of investigators' models fit well with their own experimental data but poorly with experimental data from other studies.

Table 2.1. Range of values of the author's thickness database [45]

Authors	Air Temperature (˚C)	Wall Temperature (˚C)	Relative Humidity (%)	Air velocity (m/s)
Yonko and Sepsy (1967)	21 ~ 23	-28 ~ -8	57 ~ 80	0.27 ~ 2.96
Jones and Parker (1975)	22 ~ 25	-30 ~ -8	38 ~ 66	1.19 ~ 2.96
Lee et al. (1997)	25	-15	50 ~ 80	0.18 ~ 5.00
Lee at al. (2003)	5 ~ 15	-20 ~ -15	60 ~ 70	1.0 ~ 2.5
Hermes et al. (2009)	16 ~ 22	-16 ~ -4	50 ~ 80	0.7 ~ 1.0
Cai et al. (2011)	15	-10	65	0.25
Wang et al. (2012)	-8 ~ 19	-16 ~ -8	42 ~ 80	2.22 ~ 5.00
Kandula (2014)	22.1	-9.1	72	1.77
Total	-8 ~ 25	-30 ~ -4	38 ~ 80	0.18 ~ 5.00

During the modeling of frost formation [25, 26, 45-58], many assumptions were needed to simplify the predictive models. Breque and Nemer [25] investigated the impact of the different assumptions on the accuracy of the different models. The authors indicated that improving the accuracy of correlations of the convective heat and mass transfer coefficients was one promising approach to increase the accuracy of frost modeling. The heat and mass transfer coefficients did not only depend on the thickness and density of frost, but also on the morphology of frost surface. Therefore, assuming the frost layer is a smooth wall during frost modeling can result in errors or inaccuracies [25]. Information about frost surface roughness is essential for developing accurate models of frost growth and heat transfer.

Frost Crystal Shape

With the development of better optical technologies, researchers are now able to study the microstructure of frost, particularly the frost crystal shape to gain a better understanding of the frost growth behavior.

In 1955, Shaw and Mason [59] investigated ice crystal growth. They indicated that at constant temperature and supersaturation, the ice crystal growth ratio between axial and lateral directions approximates a limiting value dependent on the temperature. As a result, different types of hexagonal columns may be formed. Later, Kobayashi [60] explored the types of ice crystals formed in cold air and generated a graphic representation of the ice crystal growth as a function of air temperature and air supersaturation. Ice crystals tended to grow in faceted crystals if air supersaturation, the crystal size, and/or the background gas pressure was small enough. When the combination of these factors was sufficiently large, branching eventually occurs to form complex structures [61, 62].

Hayashi et al. [63] proposed a rough crystal formation map (as shown in Figure 2.4.) of frost formed on a cold flat plate when studying the relation between the frost properties and frost formation phenomena. The shape of the frost crystal was dependent on the cold wall temperature as well as the water vapor concentration difference between the free stream and the cold wall surface. Four frost crystal structures were characterized: types A, B, C, and D. Specifically, type A frost grew with feather-type branches and expanded almost upward from the cold surface. Type B had similar characteristics to type A, but with plate-type branches instead of feather-type branches. Types C frost had a smaller rate of the upward growth rate compared to type A and B, because the frost was formed not only on the top of the crystal but also on the sides and on the bottom of it. At last, type D frost formed as regular square plate crystals or thin irregular crystals.

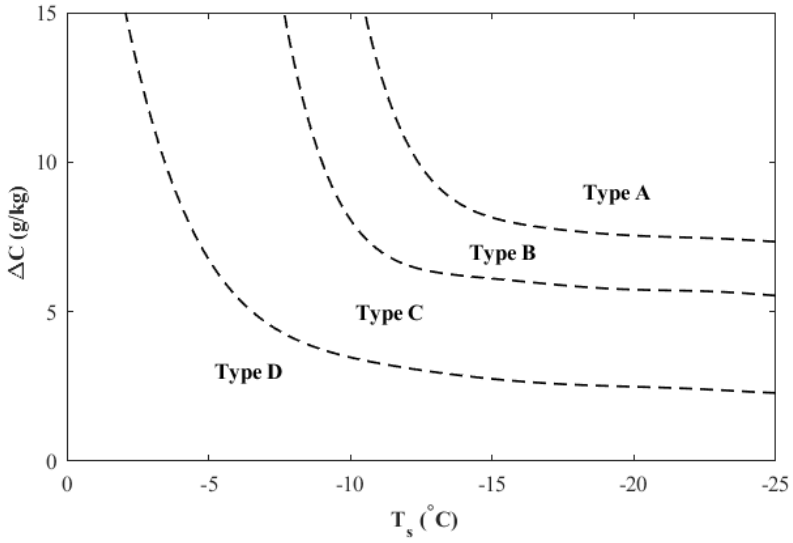

Figure 2.4. Changes of frost crystal shape with various water vapor concentration difference (ΔC) and cold surface temperature (T_s) [63].

Using a microscopic system, Cheng and Shiu [14] recorded the transient variation of the crystal patterns when investigating the dependence of crystal structures under various atmospheric conditions. The authors showed the involvement of atmospheric conditions in the frost crystal patterns. Therefore, the assumptions of frost structures in modeling must be carefully made.

To further study frost crystal structures, researchers presented descriptive frost maps based on their experimental observation. Lee et al.[18] classified frost crystals into three types: feather-type, grass-type, and plate-type. Frost with plate-type has the highest density and lowest thickness compared to feather-type and grass-type frost. Similarly, Wu et al. [17] investigated frost formation in its initial stages and proposed an informative map of frost crystal type related to cold wall temperature (T_s) and water vapor humidity difference between free stream and cold surface (ΔC). As illustrated in Figures 2.5 and 2.6, five types of frost morphologies were proposed, including super-

cooled water droplets, irregular crystals, flake crystals, needle and pole crystals, and feather crystals.

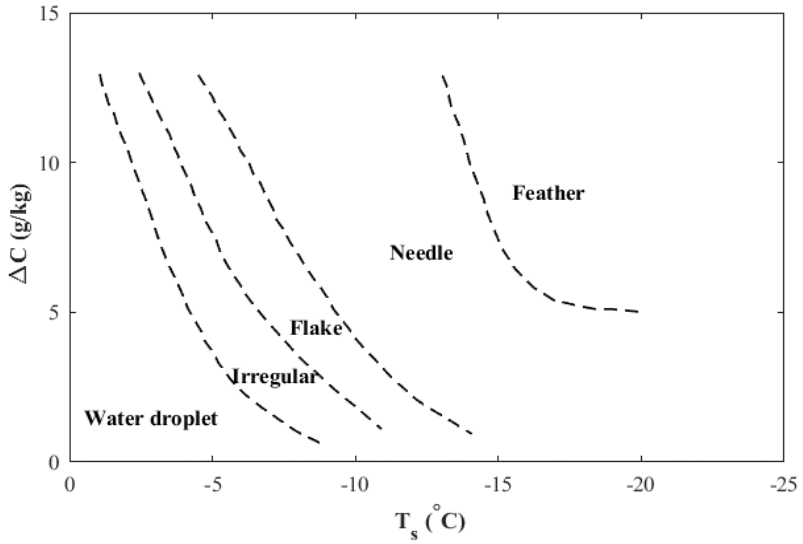

Figure 2.5. Dependence of initial frost crystal shape on surface temperature and humidity I: super-cooled water droplets, II: irregular crystals, III: flake crystals, IV: needle and pole crystals, V: feather crystals [17].

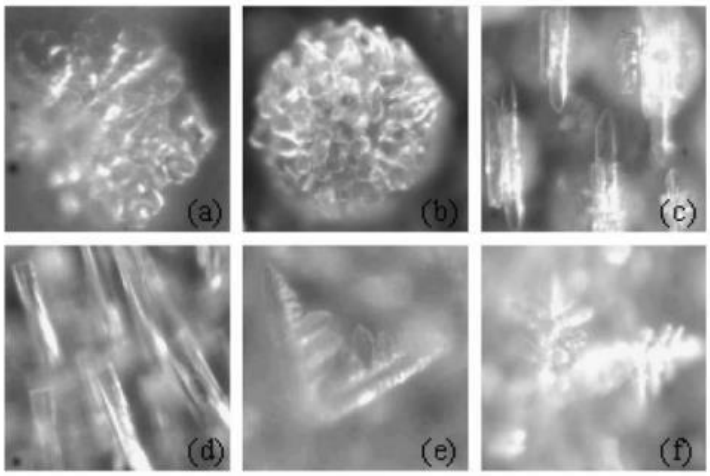

Figure 2.6. Four typical shapes of initial frost crystals (a) irregular crystals (b) flake crystals (c, d) needle and pole crystals (e, f) feather crystals [17].

Researchers have noticed that the variation of frost crystal structure had significant impacts on frost properties. Frost growth could be strongly influenced by the

initial porosity of the frost layer [26] and present different rates corresponding to the variations of the frost crystal growth direction [27]. A thick and porous frost resulted in a high average roughness while a thin and dense frost led to a low average frost roughness [32]. In 2015, Chen et al. [64] explored the effects of low atmospheric pressure on frost formation. They indicated that the water vapor concentration gradient was reduced as the atmospheric pressure decreased. As a result, the frost crystal shapes were changed, which led to a slow growth of frost thickness. Recently, Leoni et al. [4] analyzed the frost conductivity modification from the perspective of frost crystal formation. Compared to plate-type crystals formed in high wall temperature, column-shaped crystals that grew in low surface temperature allowed easier heat conduction and led to a higher frost thermal conductivity. Based on these observations, the authors highlighted the critical role of frost crystal shapes (morphology) in understanding the frost growth and density.

Frost crystal type plays an important role in the evolution of frost formation. However, the influences of environmental conditions on frost morphology, such as frost crystal type, size, and distance between crystals, were not fully documented or explained in the open literature. The investigations of Hayashi et al. [63] and Wu et al. [17] were conducted at constant air temperatures of 25°C and 22°C, respectively. For air source heat pump and refrigeration systems, frosting occurs at much lower air temperatures than 22°C [4, 65-67]. None of the previous studies have analyzed the impacts of air temperature changes on frost crystal formation nor have they investigated frost crystal structures at much lower air temperatures closer to those where frost forms on heat pump evaporators. Thus, it is important to examine the role of air temperature changes on frost crystal formation.

Frost Roughness

Aerodynamically, frost formed on a surface increases the surface roughness and increases the frictional drag of the air across the surface. The additional drag can significantly hamper the performance of engineering systems by raising the pressure drop in heat exchangers [1, 28] or reducing the lift during the takeoff of aircraft [2, 29, 30].

Chen and Rohsenow [1] investigated the pressure drop on a frosted pipe and found that the measured pressure drop was greater than the expected pressure drop caused only by the flow area reduction from the formed frost. The authors indicated that these observed trends were attributed to the surface roughness of the frost layer. A correlation between the frost roughness and equivalent sand roughness was qualitatively established via comparisons between frost images and sand grain sizes. Following this approach, a relationship between frost thickness and frost equivalent sand roughness was developed as shown in Figure 2.7. According to Chen and Rohsenow, frost roughness was proportional to frost thickness in the initial growth stage, and gradually climbed to a plateau as the thickness continued to grow.

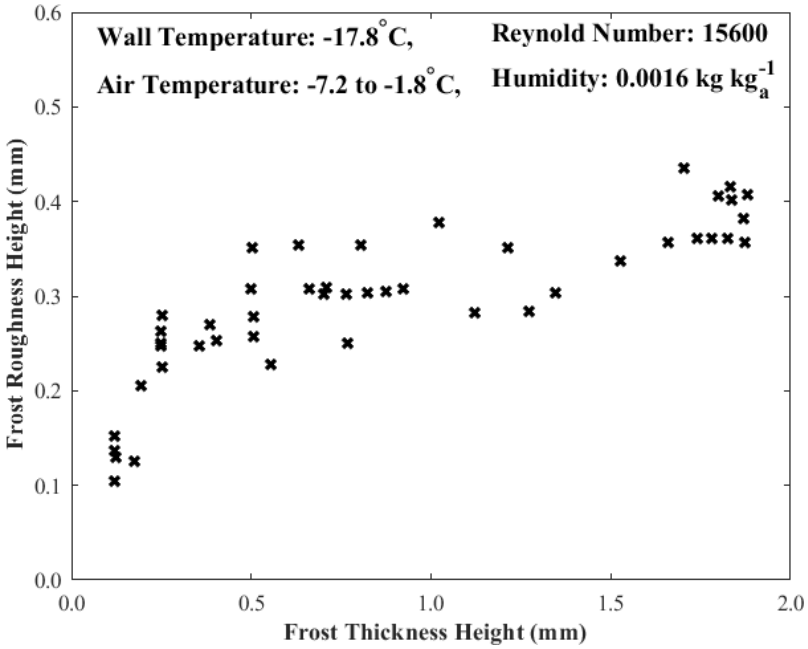

Figure 2.7. Relationship between frost roughness height and frost thickness height [1].

To investigate the aerodynamic impacts of wing surface contaminations, Dietenberger [2] presented an empirical relationship to demonstrate the effects of frost roughness height on relative lift coefficient degradation ($\Delta C_L/C_L$), relative attack angle increment ($\Delta\alpha/\alpha$), and drag coefficient increment (ΔC_d). The results pointed out that the reduction of maximum lift coefficient may be as high as 33.3% and the reduction of maximum angle of attack may be as high as 24.1%. Therefore, for a safe takeoff, the maximum gross weight of an aircraft with surface contaminations was recommended to be reduced as much as 33%. The height of the frost investigated in his study was from 0.1 mm to1.0 mm.

Yun et al. [31] developed an empirical correlation of frost roughness (y) with time (t) on a flat plate (128 mm wide and 500 mm long) at subfreezing temperatures. The correlation is given in Equation 2.1.

$$y(t) = 3.92 * 10^{-3} + 0.069 \cdot t - 0.0023 \cdot t^2 + 2.84 * 10^{-5} \cdot t^3 - 1.28 * 10^{-7} \cdot t^4 \quad (2.1)$$

The correlation is shown in Figure 2.8. Frost roughness peaked at about 25 minutes, then decreased over time. The frost roughness was defined as the height difference between frost hill and valley. It was measured under magnification using a micrometer with a thin needle to ensure the needle tip/frost contact. Figure 2.8 shows the time variation of frost roughness and the initial frost formation shape.

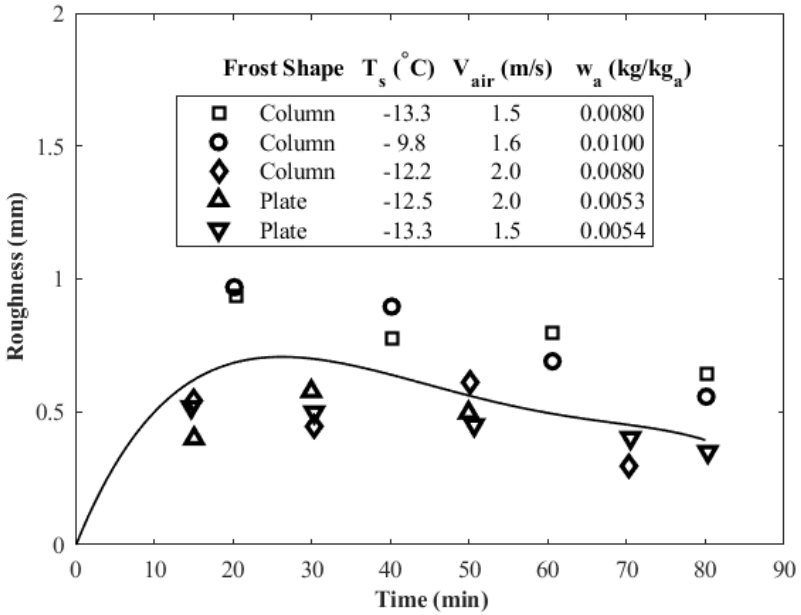

Figure 2.8. Time Variation of Frost Roughness at Constant T_{air} 26.85°C (300 K) [31].

In Figure 2.8, frost increased in roughness rapidly during the crystal growth period and gradually reduced with time during the frost layer growth period. The authors employed the frost formation type map from Hayashi et al. [19] and described the frost roughness change as follows: column-shaped crystals grow almost normal to the frost surface so that a rough frost is formed; while plate-type crystals make the frost layer dense and flat.

Nevertheless, Yun et al.'s frost roughness correlation had several limitations due to the small range of experimental conditions and its high standard deviation (±29%). The

roughness data were based on one local measurement (250 mm away from the leading edge of the 500 mm-long flat plate), which limited the ability to collect root-mean-square (RMS) height and skewness of the frost surface. The correlation was only a function of time, but the frost roughness was known to be strongly influenced by several other environmental and surface conditions, such as air temperature, wall temperature, air velocity, and air humidity. Moreover, the physical contact from the thin needle could have altered the local frost structure and induced errors in the results. All of these concerns require caution in using the correlation (Equation 2.1) to characterize frost roughness.

Although the importance of frost roughness has been well acknowledged in the literature, there have been few measurements of frost roughness due to the delicate, temperature-sensitive and partially transparent structure of frost. Any physical contact with the surface or thermal effects from a measurement operation could disrupt the state of the frost surface. Conventional noncontact methods, such as NASA laser scanner [68], electromagnetic wave interferometry [69], and chromatic confocal profilometry [70], however, lack adequate accuracy with transparent objects such as frost crystals. Additionally, white paint must be applied on the measured surface to reduce the reflection of light from a laser scanner. The paint can alter the frost surface, which reduces the accuracy of the laser measurements.

Conventional methods of frost roughness measurement [31, 32] were based on lateral side 2D frost surface profiles generated during frost thickness measurements. It should be noted that frosting usually presents nonhomogeneous nucleation along the edges of test surfaces. Moreover, the 2D lateral side surface profiles provide overlapped

views of the frost formed at different distances from the camera. These different views might not represent the actual distribution of frost crystals over the frost surfaces. Another approach of frost or ice roughness measurement was to apply 3-D photogrammetry to derive the spatial and geometrical information of the frost surface. In 1985, Mikkelson et al. [71] used two cameras to capture peaks and valleys of ice formed on the wing of aircraft, then applied an analytical plotter to obtain a measurement of ice surface roughness. Later, Collier et al. [72] utilized close-range photogrammetry to build a 3-D model for studying ice accretion over time. Their methods established a noninvasive measurement process that allowed maximum data acquisition at a minimal time cost.

Recently, Miyauchi et al. [33] demonstrated and validated a measurement method using structure-from-motion photogrammetry [34] to fulfill the purpose of nonintrusive and in-situ measuring of the frost roughness on a closed-loop psychrometric wind tunnel. This method was noncontact and required rapid data acquisition. This approach was non-intrusive and did not impose changes to the frost surface, structure, or temperature when frost was grown over a wide range of environmental conditions. In his study, two primary parameters of frost roughness statistics, RMS height (R_q) and skewness (Skw), were calculated from the spatial geometry data of frost surface model. The author then calculated equivalent sand-grain roughness height (k_s) from an empirical formula (Equation 2.2) proposed by Flack and Schultz [73].

$$k_s = 4.43R_q(1 + \mathrm{Skw})^{1.37} \tag{2.2}$$

The equivalent sand-grain roughness height (k_s) was considered more advantageous in the field of aerodynamics. It has been used to predict the frictional drag coefficient (C_f) by using boundary-layer similarity scaling. For a fully rough regime, Flack and Schultz [73] presented an empirical equation to calculate the overall frictional drag coefficient (C_f).

$$\sqrt{\frac{2}{C_f}} = -2.186 \ln\left(\frac{k_s}{L}\right) + 0.495 \tag{2.3}$$

In the above equation, L was the overall length of the plate. The uncertainty in the overall frictional drag coefficient (C_f) was ±2% for $\frac{k_s}{L} = 0.001$, and less than ±1% for $\frac{k_s}{L} = 0.00001$.

Summary

A number of conclusions could be drawn from this literature review:

1) Researchers have developed relationships between the initial frost crystal type and environmental parameters, including the cold wall temperature and the air supersaturation. However, there has been no investigation analyzing the impacts of air temperature on frost crystal structure. In addition, none of the prior investigators looked at the changes of frost crystal size and distance during the initial period of frost formation. Consequently, exploring how the initial frost crystal structure varies under various environmental conditions may lead to a better understanding of frost growth.
2) The role of frost crystal shape in affecting frost growth has been highlighted. Researchers have analyzed frost properties, such as frost thickness, frost density,

and frost thermal conductivity, from the perspective of frost crystal formation. However, few investigators have related to the change of frost roughness as the frost layer growth. Thus, quantifying how frost roughness changes under various testing conditions could be beneficial for better understanding frost.

3) Although the unevenness of frost properties over the test surfaces have been widely observed and well explained, none of the investigators have related to frost surface roughness. The influence of environmental parameters on the uniformity of frost surface roughness has not been evaluated. Therefore, it is essential to experimentally investigate the spatial distribution of frost surface roughness.
4) A predictive method of frost surface roughness is desirable for investigating the aerodynamic degradation caused by frost. A model of frost roughness can be helpful not only for improving the estimates of the heat and mass transfer on a frost layer, but also for quantifying the impact of frost on the aerodynamic performance of a surface.

CHAPTER THREE

Impact of Environmental Conditions on Frost Crystal Structure
(Accepted by International Journal of Air-conditioning and Refrigeration)

Abstract

Frost crystal type and distribution were characterized in the initial periods of frost growth on an aluminum surface. Experiments were carried out for a range of wall temperatures from -25 to -5˚C, air temperatures from 6 to 22˚C, relative humidities from 15 to 85%, and air velocities from 0.5 to 5.0 m/s. The results showed that frost crystal type was strongly dependent on the wall temperature and humidity. Changing the air temperature shifted the region of some frost crystal types. Decreasing the air temperature from 22 down to either 12 or 6˚C led to the decrease of feather crystals but increased the region of scroll crystals. Air velocity had smaller impacts on frost crystal type but had a strong influence on the distance between the crystals, particularly at lower air velocities. The results were compared to prior researchers. The results should provide a better understanding of frost morphology during the early stages of frost growth on metal surfaces.

Key Words

Frost formation, frost crystal type, crystal distance, frost microstructure

Introduction

Frost formation is an undesirable phenomenon in refrigeration, heat pumps, aerospace, and other engineering systems. Frost growth between heat exchanger fins

results in a reduction in performance due to the increase of thermal resistance between the fins and the air and increased restriction in the airflow between the fins [1]. Frost forming on a cold airfoil surface can increase the surface roughness and result in a decline in lift and an increase in drag [2].

In the past 70 years, frost growth under different atmospheric and surface conditions has been investigated extensively, specifically on flat plates. Researchers [3-14] indicated that air relative humidity (RH), air velocity (V_{air}), wall surface temperature (T_s), and air temperature (T_{air}) have primary impacts on the structure and properties of frost deposited on a cold surface. Frost formation usually starts with condensation of water droplets and the subsequent freezing of these super-cooled droplets. Frost crystals then emerge on the frozen condensate droplets. As these crystals grow and overlap with their neighboring crystals, a frost surface or layer then forms. Hayashi et al. [19] studied frost formation on a cold flat plate under forced convective flow and proposed a three-period model of frost growth: (a) crystal growth, with frost nucleation and growth in the direction vertical to the cold wall surface; (b) frost layer growth, when frost crystals expand in multiple direction and interact with other crystals to form a porous frost with a rough surface, and (c) fully developed frost layer growth, when the top part of frost reaches the melting temperature (0˚C) and eventually frost growth stops.

With the development of optical technologies, researchers [14, 17, 18, 59, 60, 63] have been able to study the microstructure of frost in the initial frost growth period to gain a better understanding of the initial stages of frost formation. Shaw and Mason [59] investigated ice crystal growth and found that at a constant cold air temperature and supersaturation, the ice crystal growth ratio between the axial and lateral directions

approximated a limiting value dependent on the ambient temperature. As a result, different types of crystals may form, such as column or plate shapes. A few years later, Kobayashi [60] generated a graphic representation of ice crystal growth as a function of air temperature and air supersaturation. Generally, with supersaturation, the crystal size, and/or the background gas pressure is small enough, the ice crystals tend to grow in faceted crystals. When the combination of these factors is sufficiently large, branching eventually occurs to form complex structures [61, 62].

In 1977, Hayashi et al. [63] proposed a map (see Figure 3.1) of frost crystal type on a cold wall surface in the initial stage of frost forming on a cold surface. The experiments for developing their map were carried out for a fixed air temperature at 25˚C, wall temperatures ranging from -25 to 0˚C, specific humidities ranging from 4.5 to 10 g/kg, and air velocities ranging from 1.0 to 6.0 m/s. This air temperature was much higher than air temperatures where frost often occurs on heat pump or refrigeration systems. In these types of equipment, frosting often only happens at air temperatures below about 5 to 10ºC [74]. Thus, the results from Hayashi may not be relevant to many frosting applications. Their results showed the frost crystal structure was dependent on the cold wall temperature (T_s) and the water vapor concentration difference between the free stream and the cold wall surface (ΔC). Four frost crystal structures were classified: A, B, C, and D, as shown in Figure 3.1. In the initial period of frost formation, type A frost grew almost linearly upward from the cold surface and generated feather-type branches around the top of the crystals. Type B had similar characteristics to type A. However, type B frost developed plate-type branches instead of feather-type branches. Types C formed a dense frost layer. The upward growth rate of the frost crystal was

smaller, because the frost was formed not only on the top of the crystal but also on the sides and on the bottom of it. Type D looked almost the same as the frost crystal pattern as type C. Regular square plate crystals or thin irregularly formed crystals were observed in type D frost.

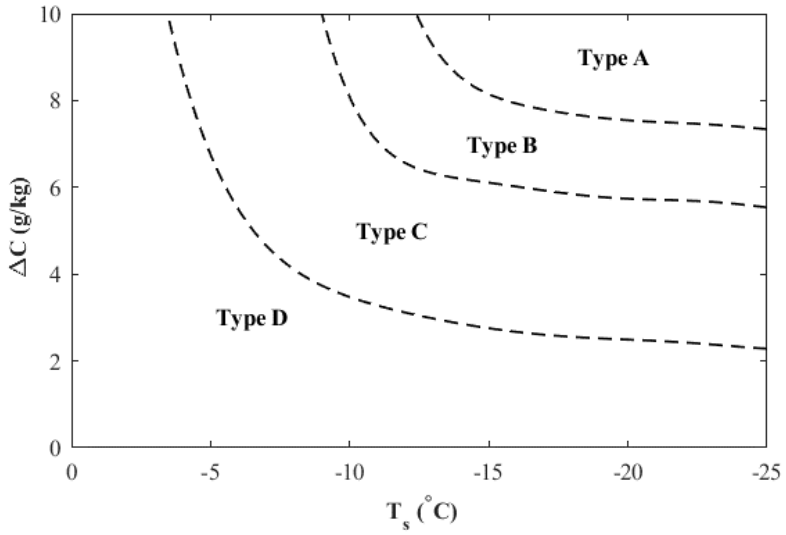

Figure 3.1. Changes of frost crystal formation with water vapor concentration difference (ΔC) and cold surface temperature (T_s) presented by Hayashi et al. [63].

Using a microscopic system, Cheng and Shiu [14] recorded the transient variation of frost crystal patterns when investigating the dependence of crystal structures under different atmospheric conditions. The authors included the involvement of atmospheric conditions in the frost crystal patterns. Their analysis showed that frost crystal structure should be considered when modeling frost growth.

Other researchers have presented alternative frost crystal maps based on their experimental observations during the frost crystal growth period. Lee et al.[18] classified frost crystals into three types: feather-type, grass-type, and plate-type. The distribution of these three crystal types was similar to those of Hayashi et al. [63]. Feather-type, grass-type, and plate-type crystals covered the Hayashi et al. regions of type A and B, type C,

and type D, respectively. Frost with plate-type crystals had the highest density and lowest thickness compared to feather-type and grass-type frosts. Similarly, Wu et al. [17] investigated frost formation in its initial stage and presented a more informative map of frost crystal type as illustrated in Figure 3.2. Their experiments were carried out for air temperatures at 22˚C, wall temperatures ranging from -20 to 0˚C, and relative humidities ranging from 15 to 85%. Four types of frost crystals were proposed, including feather crystals, needle and pole crystals, flake crystals, and irregular crystals. As with the Hayashi et al. [17] study, the air temperatures for Wu et al. [19] were much higher than the normal air temperatures where frost would form on heat pump evaporator surfaces. Compared to previous studies [18, 63], the classification of Wu et al. [17] were more specific, and the formation regions of different types of frost crystals were more precise.

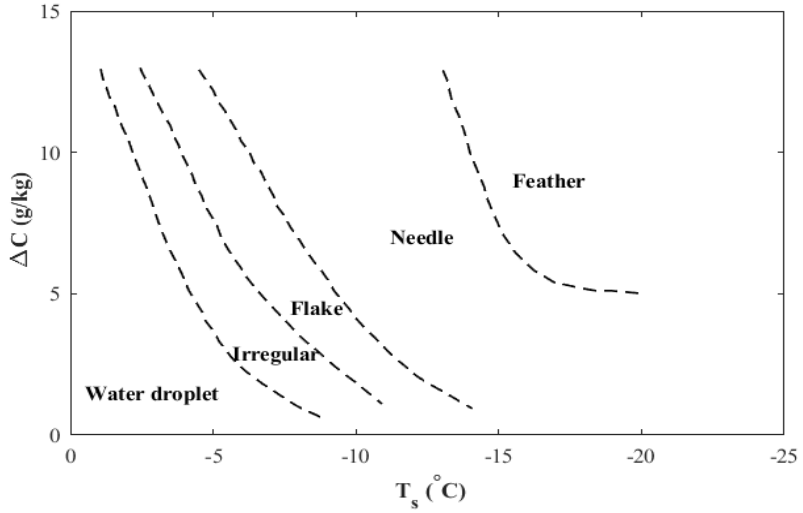

Figure 3.2. Dependence of initial frost crystal shape on surface temperature (T_s) and humidity difference (ΔC) as presented by Wu et al. [17].

In recent years, more researchers have investigated the variation of frost properties from the perspective of frost morphology. Lee and Ro [26] analyzed the frost growth on a flat plate and found that the initial porosity of the frost layer played an important role in

determining the frost layer growth characteristic. Qu et al. [27] carried out a visual analysis of frost formation on flat surfaces and observed that the frost growth rate changed due to the variations of the frost crystal growth direction. Recently, Chen et al. [64] analyzed the changes of frost morphology under low atmospheric pressure and indicated that reducing atmospheric pressure can affect the frost crystals shape and then the frost layer thickness due to the reduction of the water vapor concentration gradient. In 2017, Da Silva et al. [28] produced experiments on the thermal hydraulic performance of fan-supplied tube-fin evaporators. The experiments revealed that equal amounts of frost may cause different air pressure drops depending on the operating conditions that affect the frost morphology and, therefore, the frost density. By applying the map of Wu et al. [17], Leoni et al. [4] described how frost crystal shapes affected frost thermal conductivities. Compared to flake crystals formed at high wall temperatures, needle crystals grew at lower surface temperatures and had higher heat conduction which led to a higher frost thermal conductivity. Based on these observations, the authors highlighted the critical role of frost crystal shapes in understanding frost growth and density.

Besides the influence on frost density and thickness, frost crystal structure can also play a role in frost roughness formation. Yun et al. [31] experimentally explored frost roughness evolution on a flat plate at subfreezing temperatures. The authors explained the frost roughness change by applying the initial frost crystal formation map of Hayashi et al. [63]: needle type crystals grew almost normal to the frost surface so that a rough frost was formed; plate type crystals made the frost layer dense and flat. Recently, Niroomand et al. [32] investigated frost growth in a horizontal plate under natural convection. They indicated that a thick, porous frost layer resulted in a high average roughness and negative

skewness of frost surface while a thin and dense frost layer led to a low average frost roughness and positive frost skewness.

Frost morphology plays a critical role in studying frost formation. However, the influences of environmental conditions on frost morphology, such as frost crystal type, size, and distance between crystals, are not fully understood in the open literature. Hayashi et al. [63] and Wu et al. [17] carried out their experiments and measurements at constant air temperature, 25°C for Hayashi et al. [63] and 22°C for Wu et al.. For air source heat pump and refrigeration systems, researchers are more likely to run tests under much lower air temperature than 22°C [4, 65-67]. None of Hayashi et al. and Wu et al. analyzed the impacts of air temperature changes on frost crystal type. In addition, none of the prior investigators looked at how frost crystal distance and crystal size were affected under different environmental conditions. In this study, the changes of frost crystal type, size and distance during the initial period of frost growth were evaluated under a range of environmental conditions, including surface temperature (T_s), air velocity (V_{air}), relative humidity (RH), and air temperature (T_{air}). Because aluminum is the most common material used for fins in heat pumps and refrigeration evaporators, the base material for the frosting surfaces was chosen to be aluminum. The results of this study should help extend the understanding of frost crystal structure and early frost growth behavior on cold surfaces at lower air temperatures than has been investigated previously. In addition, the results from this study can be used to explain the changes of frost surface morphology which is directly related to frost surface roughness evolution.

Experimental Apparatus

To explore the effect of environmental variables on frost crystal formation, a closed-loop psychrometric wind tunnel was used in this study. It included several modular sections, including an adjustable-speed blower, two cooling coils, a duct heater, a humidification system and a dry gas (zero-grade nitrogen gas) injection system. Figure 3.3 shows the schematic drawing of the wind tunnel loop system with the relative locations of these components. The function of the wind tunnel was to provide continuous, conditioned airflow over an interchangeable test surface mounted to the bottom side of the test section.

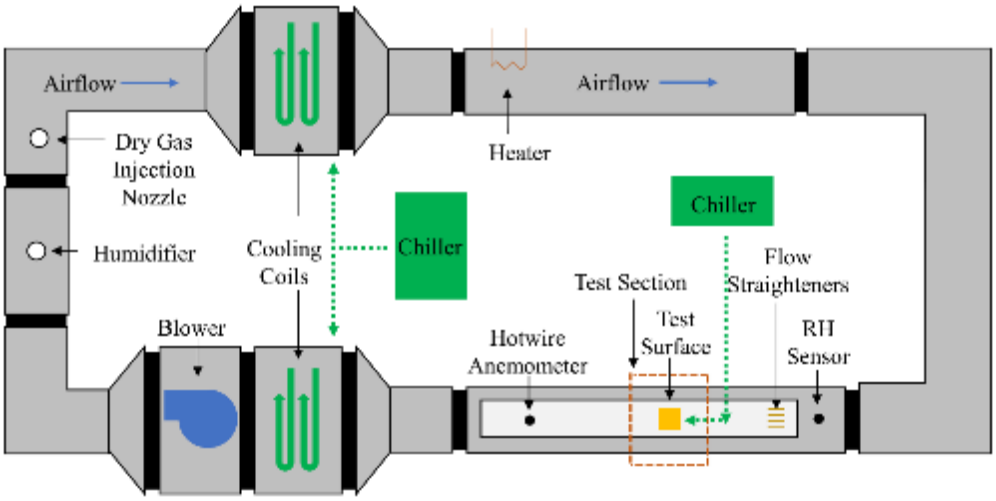

Figure 3.3. Schematic overview of the wind tunnel loop system.

The test stage (as shown in Figure 3.4) was made of machined optical transparency acrylic glass that had a low thermal conductivity (0.2 W/(m·K)). A 0.17 mm thick single pane of optical quality glass on the acrylic panel of the test stage allowed for in-situ, top-down viewing in the microscopy system without disruption to the experimental process. Upstream of the test section, a group of cylindrical, plastic flow straighteners were applied

at the inlet of the inner annulus to generate laminar flow. The inner annulus had a rectangular shape with 15 mm height and 60 mm width. A relative humidity sensor and a type-T thermocouple were mounted upstream from the test surface and used for the measurement of the entering air temperature and relative humidity, respectively. There was also a hot wire anemometer downstream from the test surface for the measurement of the air velocity. Figure 3.5 gives an example of the vertical distribution of the air velocity profile in the test section. An upright style Nikon stereoscopic microscope (model LV150) was mounted above the test section to observe the experimental process vertically. Two long-working-distance objective lenses, 5X magnification and 20X magnification, were used. A customized light-emitting diode (LED) illuminator was applied to minimize the effect of heat generated from the light source. To provide real-time visualization of the freezing processes on the test surface, an IDT-Redlake M3 high-speed digital camera was attached to the upper viewport of the Nikon microscope and stabilized with a C-clamp. The camera operated with a 15.4 by 12.3 mm proprietary complimentary metal-oxide-semiconductor photodiode array and was set at 1280 by 1024 pixels resolution.

A thermal stage mounted at the bottom of the test section was the central component of the experimental system used to control the test surface temperature. Figure 3.6 provided the detailed view of the thermal stage. The main components consisted of a Peltier module, a copper heat sink with a 3 cm by 3 cm aluminum surface plate, and a type-T thermocouple. An electromechanical switch was applied to alternate the Peltier module between cooling and heating modes. The copper heat sink with an internal circuit could conduct the heat energy from the Peltier module to the coolant (50/50 propylene glycol-water solution). The type-T thermocouple was used for the measurement of the surface temperature. All the

components in the phase-change module were bonded by a thermally conductive material with 0.254 mm thickness and the 52°C phase-change temperature. The observation location was fixed at 1cm away from the leading edge.

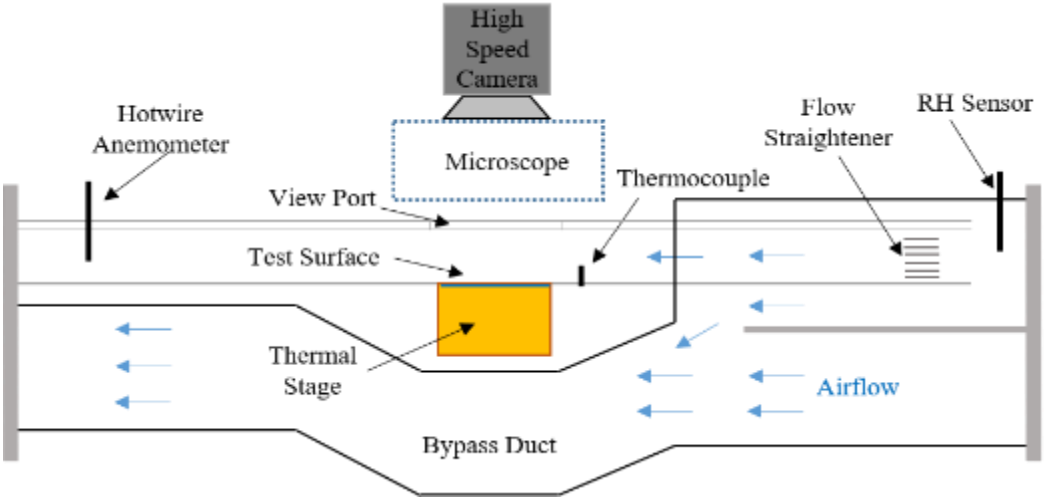

Figure 3.4. A detailed schematic of the test stage.

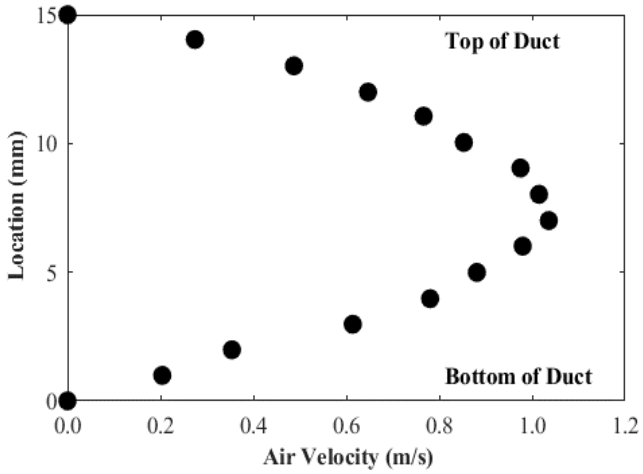

Figure 3.5. An example of the vertical air velocity distribution at V_{air} 1.0 m/s with T_{air} 22°C and RH 55%.

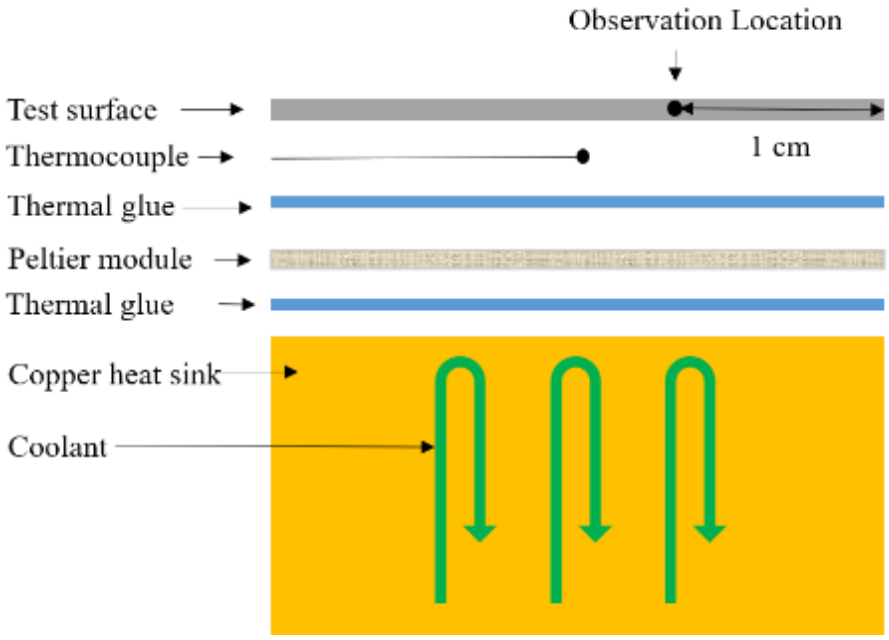

Figure 3.6. Exploded view of thermal stage.

Experimental Procedure

The experiments were carried out on a 3cm x 3cm polished aluminum surface with a 74.6° static contact angle. The experimental testing conditions were listed in Table 3.1. The free stream air temperature was maintained at 22°C, 12°C or 6°C. The relative humidity was varied in specific increments between 15 and 85%. The surface temperature was held constant during a given test. The surface temperatures ranged from -25 to -5°C. The air velocity passing through the test section could be varied from 0.5 to 5.0 m/s. Table 3.2 lists the accuracy of measurements.

Control of the system was done through a NI LabVIEW program. Before starting a frost test, the Peltier module was kept in heating mode to avoid any condensate droplets forming on the test surface. Once steady environmental conditions were reached in the wind tunnel, the Peltier module was switched to cooling mode and could reduce the surface temperature to the target wall temperature within 10 seconds. Frost formation went through

water droplet condensation, super-cooled droplet freezing, and then formation and growth of initial frost crystals on the frozen droplets. The camera system was operated manually to record the frost crystals formed in the initial period of frost growth.

Table 3.1. List of experimental testing conditions

T_{air} (˚C)	V_{air} (m/s)	T_s (˚C)	RH (%) (10% increment)	Total tests
22	1.5	-25	15 - 85	
		-20	15 - 85	
		-15	15 - 85	39
		-10	15 – 85	
		-5	25 - 85	
12	1.5	-25	15 - 85	
		-20	15 - 85	
		-15	15 - 85	37
		-10	25 - 85	
		-5	35 - 85	
	0.5	-25	65	
	1.5	-20	65	
	2.5	-15	65	20
	5.0	-10	65	
		-5	65	
6	1.5	-25	15 - 85	
		-20	15 – 85	
		-15	25 – 85	34
		-10	35 – 85	
		-5	45 - 85	

Table 3.2. Accuracy of measurements

Parameter	Control Accuracy
Air Velocity	± 0.05 m/s
Air and Wall Temperature	± 0.5°C
Relative Humidity	± 2%

Initial Frost Crystal Type

The frost crystals in the initial period of the frost growth presented different shapes under different environmental conditions. They were classified into six groups: feather crystals, sector crystals, sheath crystals, pole crystals, scroll crystals, and flake crystals, as shown in Figure 3.7. Compared with the classifications of frost crystals from previous investigations [18],[17], we had similar descriptions of the feather and flake crystals, but differentiated the grass-type crystals of Lee et al. [18] or needle and pole crystals of Wu et al. [17] into sector, sheath, pole and scroll crystals according to their unique structure. The corresponding symbols to the six classifications are also shown in Figure 3.7 in the top left corner of each photo. These symbols were also used in the following figures to represent the different frost crystal types.

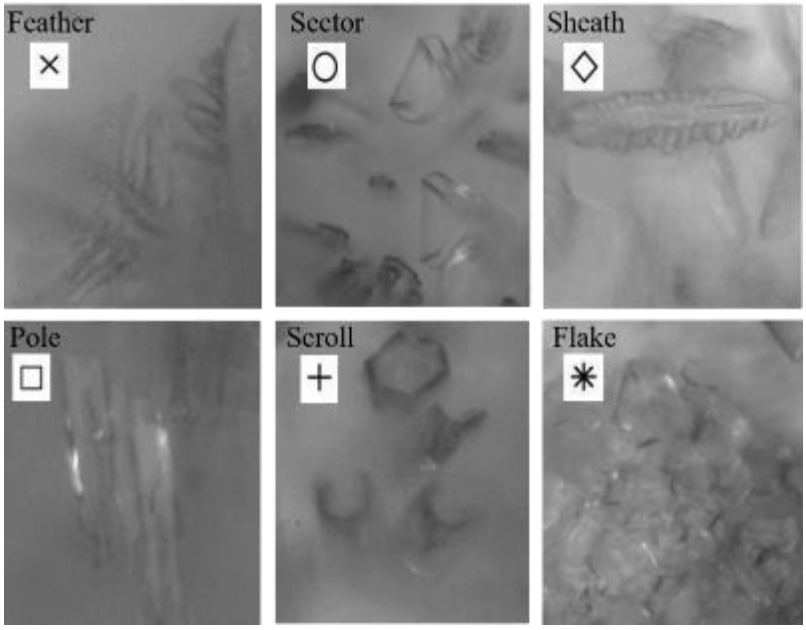

Figure 3.7. Shapes of frost crystal in the initial stage of frost growth and symbols used to represent each frost crystal.

Generally, the feather crystals appeared at wall temperature lower than -15°C and relative humidity over 25%. This boundary in the relative humidity increased from 25 to 45% as air temperature was decreased from 22 to 6°C. These crystals had fast growing branches which created crystals with large lateral dimensions. These branches were needle or plate shapes. Feather crystals mainly extended normal to the cold wall surface and left large voids between the crystals. Sector crystals were observed under wall temperatures lower than -15°C. The required maximum relative humidity for sector crystal formation increased from 25 to 45% as air temperature decreased from 22 to 6°C. Sector crystals grew almost without branches. As the wall temperature increased over -15°C, three types of crystals with column growth pattern formed: sheath crystals, pole crystals, and scroll crystals. They all grew mainly in the axial direction and rarely laterally. Sheath crystals had rough edges along their axial direction while pole crystals had straight and smooth borderlines. The structure of a scroll crystal, however, was hollow and had a hexagonal periphery. The last type of frost crystal, the flake crystal, appeared for wall temperatures over -5 °C in the case of T_{air} 22°C. Unlike column shape crystals, flake crystals presented a plate growth pattern and had quite small dimensions. These thin hexagonal plates were close or even overlapped with each other. Each type of frost crystal had its unique structure, which determined its characteristics. Such classification helped to reveal a better picture of frost microstructure.

Impacts of Environmental Conditions on Frost Crystal Type Formation

Figure 3.8, 3.9 and 3.10 show that the dependence of the initial frost crystal type for air temperatures of 22°C, 12°C, and 6°C, respectively. The crystal structure data were plotted as a function of both the wall surface temperature, T_s, and the absolute humidity

difference, ΔC, between the free stream and the saturated humidity corresponding to the surface temperature. Note that there is a change in the range of the y-axis in each of these figures. As the air temperature was decreased, the air could not hold as much moisture so the absolute humidity difference, ΔC, decreased. The maximum value for ΔC in Figure 3.8 was 15 g/kg for a 22ºC air temperature while for Figure 3.10 it was only 5 g/kg for a 6ºC air temperature. The types of frost crystals were marked in T_s-ΔC planes by using the same symbols shown in top left of each picture in Figure 3.7. For each air temperature, its corresponding relative humidity lines are displayed in each figure. The results illustrated that the frost crystal shape was primarily affected by the cold wall temperature but had some dependence on the free stream relative humidity. For example, in the case of T_{air} 22°C shown in Figure 3.8, the feather crystal region covered the upper-right corner of the figure corresponding to lower wall temperatures (-20 to -25°C). Humidity had some influence on the type of crystal only transitioning to sector crystals at relative humidity 15%. The lower-right area with lower wall temperatures and lower relative humidity belonged to the sector crystals. Flake crystals formed in the lower-left region where the wall temperatures were -5°C and relative humidity were below about 65%. At -10 and -15°C, the crystal structures were dominated by sheath and pole type crystals. The exceptions were at the highest air humidity (85%) at -15°C where feather crystals still formed and at the lowest air humidities (below 25%) at -10°C where scroll crystals formed. Generally, the supersaturation and the frost crystal dimensions increased from the lower-left region to the upper-right region in Figure 3.8, 3.9 and 3.10. Correspondingly, frost crystals changed from faceted shape to complex branch structures.

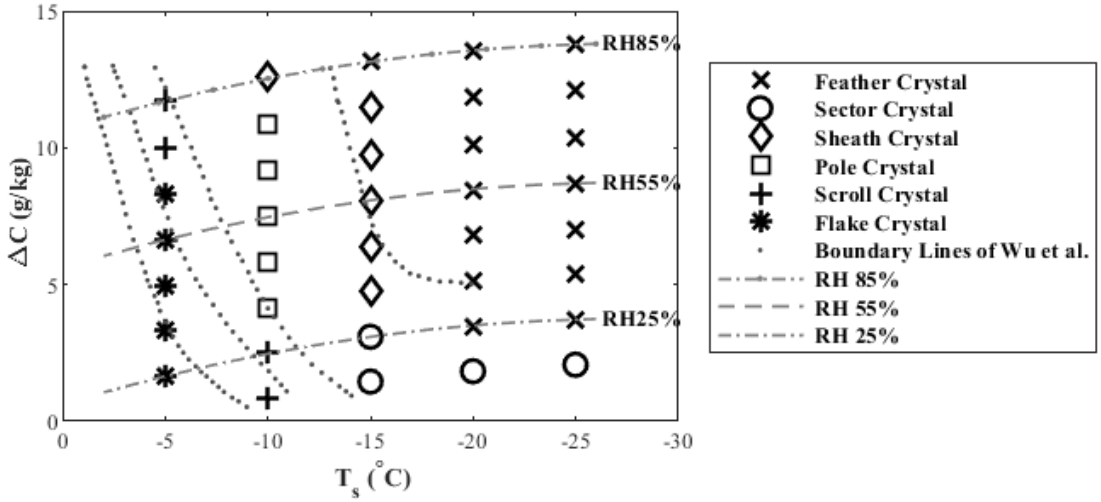

Figure 3.8. Frost crystal type at V_{air} 1.5 m/s with T_{air} 22°C.

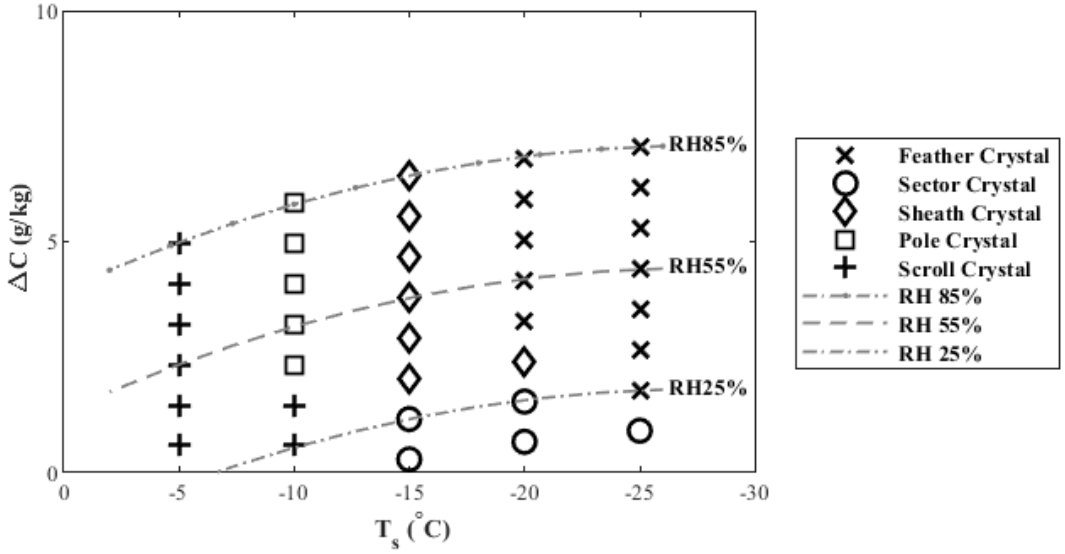

Figure 3.9. Frost crystal type at V_{air} 1.5 m/s with T_{air} 12°C.

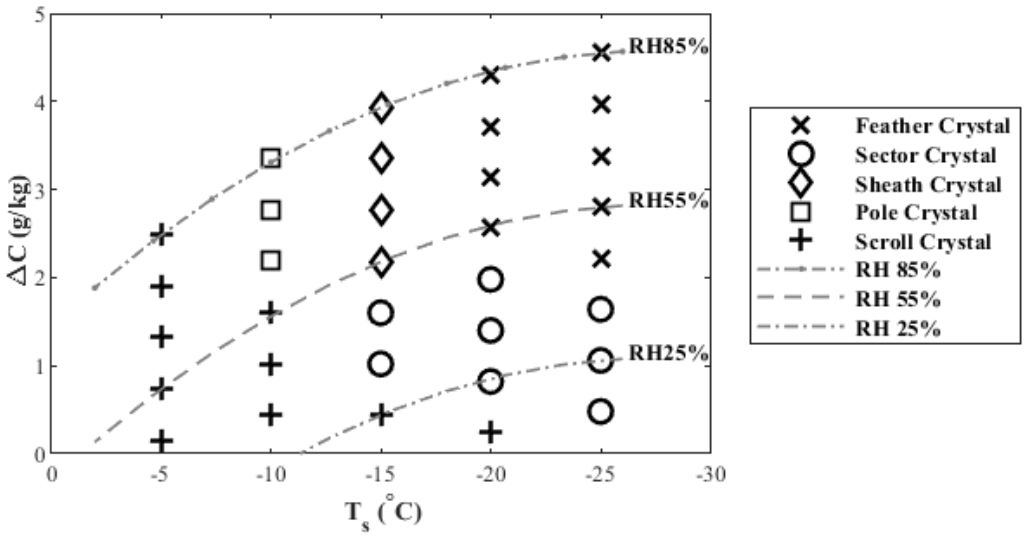

Figure 3.10. Frost crystal type at V_{air} 1.5 m/s with T_{air} 6°C.

The dotted vertical lines in Figure 3.8 showed the crystal formation map of Wu et al. [17]. Four boundary lines separated the frost crystal map into five types in Figure 3.8 according to the observation of Wu et al. [17]. The air temperature (22°C) for the tests in Figure 3.8 were the same as those used by Wu et al. [17]. From right to left, their crystal shapes included feather crystal, needle and pole crystal, flake crystal, irregular crystal, and water droplet. Our designations of the crystal shapes tended to agree well with the Wu et al.'s characterization even though we observed a wider range of crystal shapes. Our feather and flake crystal regions appeared to match well with the feather and flake crystal regions found in Wu et al.'s [17] frost crystal map. However, the middle section, named the needle and pole crystal regions in Wu et al.'s map, was divided into four groups: sector, sheath, pole and scroll crystals. This classification should present a more precise description of these column shape crystals.

One major difference in the plots in Figure 3.8, 3.9, and 3.10 was the reduction in absolute humidity difference (ΔC) as the air temperature decreased. Because ΔC is a measure of the moisture driving potential between the air and the cold surface, lower air

temperatures have lower amounts of moisture that can be deposited on the cold surface. At an air temperature of 22°C, ΔC was as high as 13.8 g/kg while at an air temperature of 6°C, ΔC peaked at 4.6 g/kg.

By comparing Figures 3.8, 3.9 and 3.10, the region covered by certain types of frost crystals shifted as the air temperature was reduced. Feather crystals continued to form at surface temperatures at -20 and -25°C regardless of the air temperature. The absolute humidity difference (ΔC) needed for the formation of feather crystals appeared to consistently be greater than about 2 g/kg. From the aspect of relative humidity, however, the air humidity region for feather crystal formation shifted upwards when the air temperature decreased from 22 to 6°C. The minimum value of air humidity for feather crystal formation increased from 25 to 55%. Sheath and pole crystals mostly formed at surface temperatures of -15 and -10°C, respectively, and at an absolute humidity difference ΔC consistently over about 2 g/kg. The corresponding relative humidity shifted upwards and varied from 35 to 55% as the air temperature decreased from 22 to 6°C. Sector crystals still formed at wall temperature ranging from -15 to -25°C and covered the area below the formation regions of feather and sheath crystals. Sector crystals maintained the same range of absolute humidity difference ΔC but varied in relative humidity range as the air temperature changed. The formations of flake and scroll crystals were significantly affected by the variation of air temperature. As the air temperature decreased, flake crystals that appeared for a surface temperature of T_s -5°C and air temperature of 22°C did not form at the two lower air temperatures: 12°C and 6°C. On the other hand, scroll crystals dominated at surface temperatures at -5°C regardless of the air temperature. Scroll crystals were also observed at some super-low humidity cases ($\Delta C < 0.5$ g/kg) for surface

temperatures of -15°C and -20°C, as shown in Figure 3.10. The formation region of scroll crystal expended towards the bottom right direction when air temperature decreased from 22 to 6°C.

The main reasons that led to the changes in the frost crystal regions appeared to be from two causes. First, related to the reduction of moisture in the air as the air temperature was decreased. There was no enough water vapor for frost crystals to grow with branches, such as feather crystals. Therefore, there was some variation in the frost crystal region as the air humidity changed. On the other hand, the air temperature itself was able to affect the growth rate in the direction normal to the cold wall surface. Increasing air temperature can create more resistance of frost crystal growth in axial direction. Figure 3.11 displays an example of the impacts of air temperature on initial frost crystal type. Three frosting tests were conducted at the same wall temperature of -5°C, relative humidity of 65%, and air velocity of 1.5 m/s. The air temperature varied from 22°C to 6°C. Correspondingly, frost crystal type changed from flake shape to scroll shape. High air temperature forced the growth of frost crystal in plate pattern instead of column pattern.

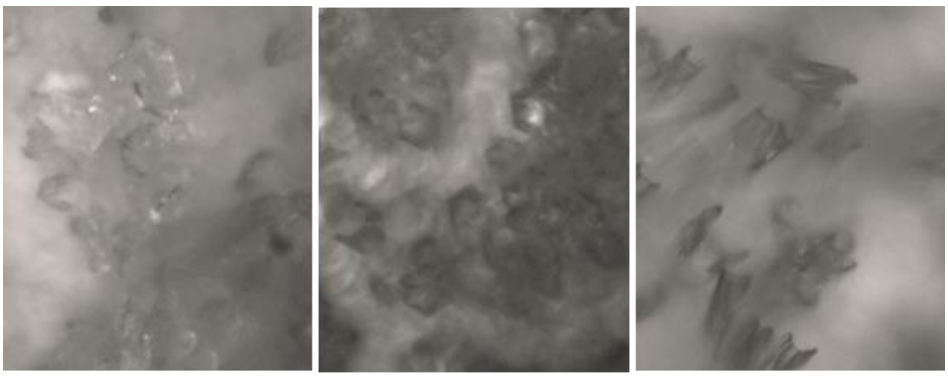

Figure 3.11. Frost crystal type at T_s -5°C and (a) T_{air} 22°C (b) T_{air} 12°C and (c) T_{air} 6°C.

Besides the impact of air temperature, the influence of air speed in initial frost crystal formation was also studied. Figure 3.12 shows the variation of initial frost crystal type with air velocity from 0.5 to 5.0 m/s, air temperature at 12°C, and relative humidity at 65%. In this range, increasing the air velocity had no impact on the initial frost crystal type. Feather crystals continued to grow under wall temperature lower than -20°C. Sheath, pole, and scroll crystals still appeared at Ts -15°C, -10°C, and -5°C, respectively. However, increasing the air velocity would affect distance between frost crystals. This effect is described in the next section.

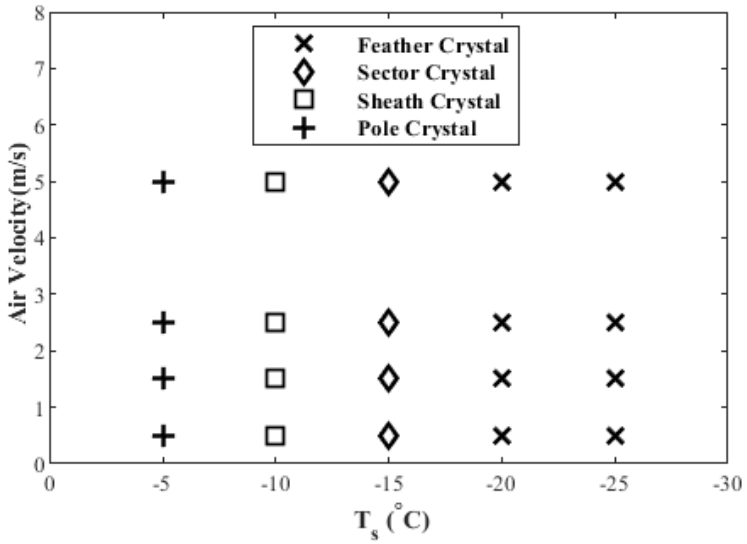

Figure 3.12. Variation of frost crystal type with air velocity from 0.5 to 5.0 m/s, air temperature of 12°C, and relative humidity of 65%.

Initial Average Frost Crystal Distance

Besides the impacts on initial frost crystal types, environmental conditions can affect the distance between the frost crystals, which can influence the frost microstructure. Therefore, the crystal distance was also evaluated. The results should be useful for the study of frost porosity and morphology during the initial period of frosting.

All images for the measurement of frost crystal distance were captured at 5 minutes after the initiation of frosting under 5X magnification, at a fixed location 1 cm from the leading edge. These captured images had an average resolution of 420 pixel per mm. By utilizing ImageJ software [75] to measure the pixel changes between frost crystals, the distance between certain frost crystal and its surrounding crystals could be obtained. The total uncertainty of frost crystal distance measurement using 5X magnification was ± 0.01 mm. Measurements were done five times for the distance between the crystal centers for a given set of frosting conditions. The average distance was then calculated along with its standard deviation. An example of crystal distance measurement is given in Figure 3.13. The variation of frost crystal size is presented qualitatively along with the analysis of changes of frost crystal distance.

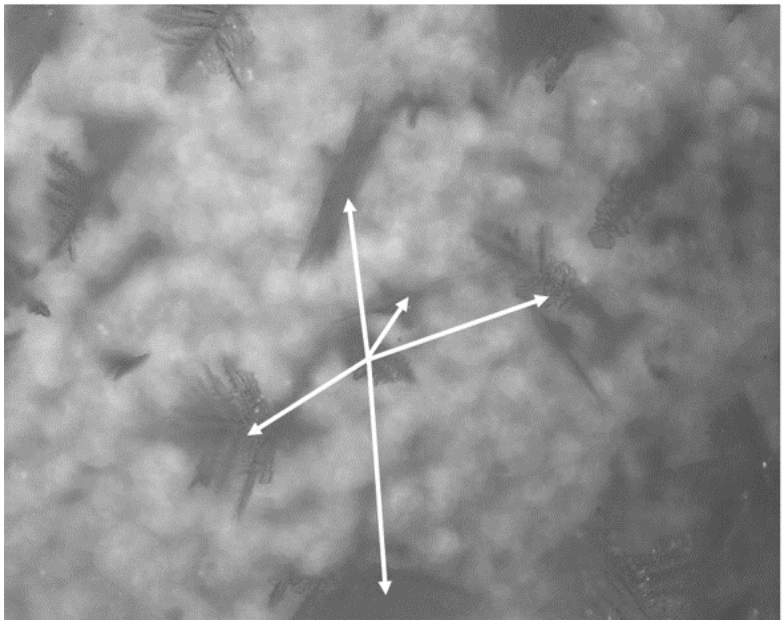

Figure 3.13. Measurement of crystal distance at 5X magnification.

The variation of crystal distance under different environmental conditions are shown in Figure 3.14. Generally, crystal distance decreased as the wall temperature

increased. Figure 3.14(a) shows the variation of average crystal distance with wall temperature and air temperature. For surfaces with wall temperatures lower than -20°C, the average crystal distances for the air temperature cases of 6°C cases were larger than those for the air temperatures of 12°C and 22°C. The potential reason was that the air at 6°C had the smallest amount of water vapor in it compared to the other two air temperature cases. When a crystal with a complex structure formed in the case of the air temperature at 6°C, the surrounding limited water vapor was absorbed by the crystal which inhibited the formation of other crystals. As a result, a greater crystal distance at an air temperature of T_{air} 6°C was generated when the wall temperature was lower than -20°C. The average crystal distance for an air temperature of 6°C reached 0.52 mm for a surface temperature of -25°C while that for an air temperature of 22°C with a surface temperature of -25°C, the distance was only 0.34 mm. Under wall temperatures higher than -15°C, however, the air temperature cases at 12°C or 22°C tended to generate larger average crystal distances than at an air temperature of 6°C. These crystals formed under wall temperature higher than -15°C had no complex branches. Their ability to absorb the surrounding water vapor was limited. In the case of the two lower air temperatures (6 or 12°C), frost crystals grew slower with smaller crystal sizes and smaller crystal distances. In the case of the 16°C air temperature case, frost crystals grew faster compared to the other two air temperature cases due to its higher absolute air humidity. Therefore, a larger frost crystal distance in the 16°C air temperature case was also associated with a larger frost crystal size when the wall temperature was higher than -15°C.

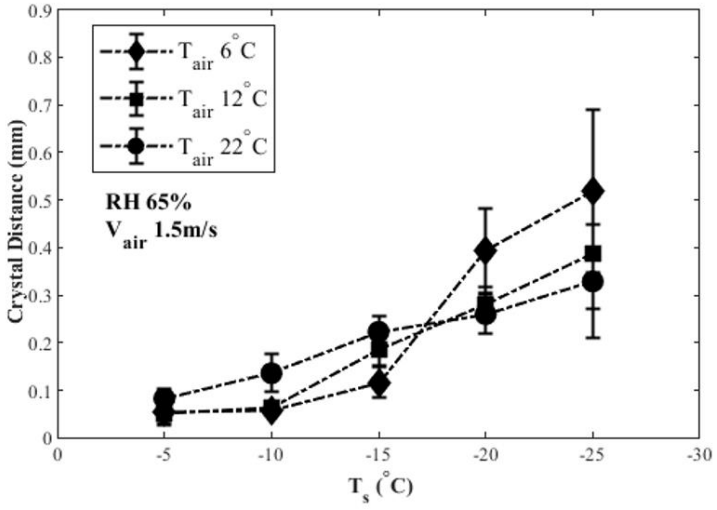

(a)

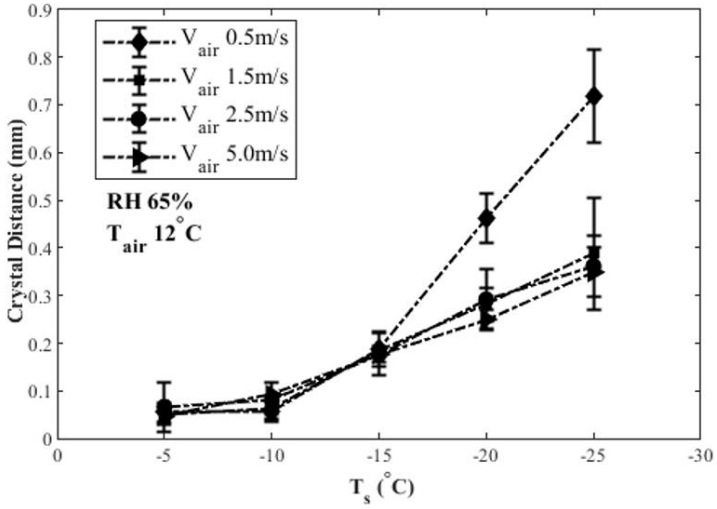

(b)

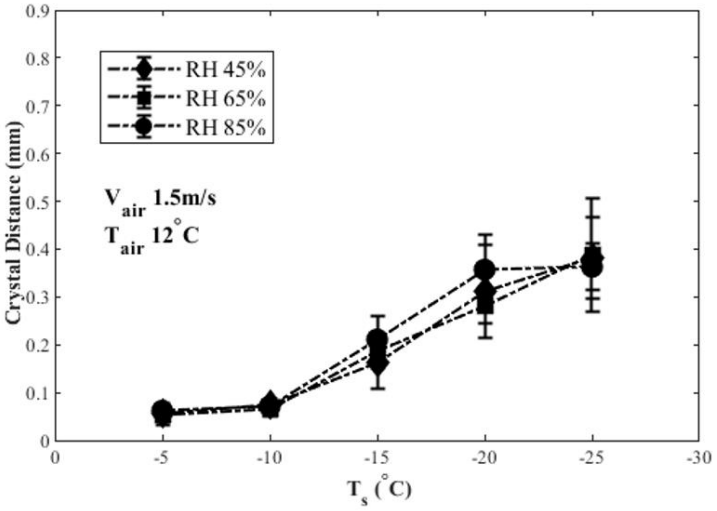

(c)

Figure 3.14. Crystal distance under different (a) T_{air}, (b) V_{air}, and (c) RH.

Figure 3.14(b) presents the variation of the average crystal distance with wall temperature and air velocity. Under a V_{air} of 0.5 m/s and T_s lower than -15°C, frost crystals grew with a large average crystal size and distance (up to 0.72 mm). Due to the low air speed, the mass transfer rate was small in this case. When a frost crystal with a complex structure formed, it would apparently absorb its surrounding water vapor and then limit the growth of other nearby frost crystals. Once the air speed and/or wall temperature reach a critical level (air speed over 1.5 m/s and wall temperature higher than -15°C), however, increasing air velocity had only small impacts on the increment of the average crystal distance. In these cases, frost crystals had enough water vapor to grow and interact with each other. Wall temperature, which determined the ice nucleation rate, became the only main parameter affecting the crystal distance.

Figure 3.14(c) shows the changes of the average crystal distance with wall temperature and relative humidity. The results indicated that increasing air humidity led to a small increase in the average crystal distance. According to the experimental observation in this task, nevertheless, frost crystal size increased as the air humidity increased. More water vapor was provided for the growth of frost crystals to grow to larger crystal sizes. Due to the interactions between crystals, however, their crystal distances did not increase much. Wall temperature was still the dominant factor influencing the crystal distance.

A multiple least square regression equation was fitted to the average frost crystal distance data. All the parameters were normalized. Equation 3.1 gives the correlation of the frost crystal distance (mm), d, as a function of dimensionless parameters, where w_a is air absolute humidity (kg/kg_a), w_s is air absolute humidity on the cold wall surface, Re_D is Reynolds number calculated by hydraulic diameter, and To is triple point temperature (K).

In Figure 3.15, the results of the frost crystal distance, calculated from Equation 3.1, are compared with the experimental data. The R-square value was 0.864.

$$d = 0.293 \left(\frac{w_a}{w_s}\right)^{0.597} (Re_D)^{-0.082} \left(\frac{T_o - T_s}{T_o}\right)^{0.619} \left(\frac{T_{air} - T_o}{T_o}\right)^{-0.270} \quad (3.1)$$

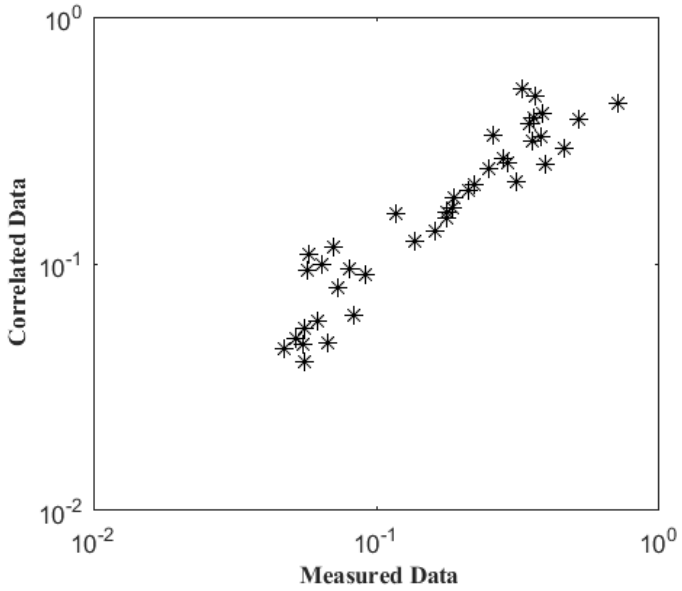

Figure 3.15. Comparison of the measured and correlated data of the frost crystal distance.

Conclusions

Frost crystal formation in the initial frosting period under various environmental conditions was investigated by using a closed-loop psychometric wind tunnel with a microscopy system. The purpose of this study was to better characterize the impact of environmental variables on frost crystal formation. It should provide a better understanding on inner and surface structure of frost formed under conditions where heat pump or refrigeration system runs. The main findings are summarized as follows:

- Frost crystal were classified into six types: feather crystals, sector crystals, sheath crystals, pole crystals, scroll crystals, and flake crystals. Such classification was helpful in revealing a better picture of frost microstructure.

- The initial type of frost crystal was mainly dependent on wall temperature and air relative humidity. Decreasing the air temperature can reduced the regions of feather crystals and flake crystals but increased the regions of scroll crystals and sector crystals. Moreover, changing air velocity had no impacts on the initial frost crystal type.
- The initial crystal size and distance decreased at higher wall temperature and higher air velocity. When air speed reached a critical level, however, it had a small influence in reducing initial crystal size and distance. Increasing relative humidity had little impact on initial crystal distance but affected initial crystal size.
- A correlation of frost crystal distance was developed as a function of dimensionless parameters.

Acknowledgements

The work in this paper were supported as part of FAA Grant 17-G-011. Any opinions presented in this paper are those of the authors and do not reflect the any official position of the U.S. Federal Aviation Administration or the United States government.

CHAPTER FOUR

Analysis of Frost Thickness and Roughness Growth from the Perspective of Frost Crystal Structure

This chapter published as: Tongxin Zhang, Dennis L. O'Neal, Stephen T. McClain, Analysis of Frost Thickness and Roughness Growth from the Perspective of Frost Crystal Structure, *International Journal of Refrigeration* 112 (2020): 314-323

Abstract

Laboratory experiments were conducted to characterize frost thickness and roughness on a horizontal cold flat surface with respect to the type of frost crystal. Air velocities, free stream temperatures, wall temperatures, and relative humidities were varied from 0.5 to 1.5 m s^{-1}, 16 to 6°C, and -25 to -15°C, and 50 to 75%, respectively. Three-dimensional photogrammetry was employed for evaluating frost roughness characteristics. The results showed that the frost growth corresponded with changes of frost crystal formation. Feather and needle crystals created a thick and porous layer with a rough surface, while flake and irregular crystals formed a thin and dense frost layer with a relatively smooth surface. Frost root-mean-square height began to decrease sooner under higher air velocities, higher air temperatures, and higher wall temperatures. The maximum value of frost root-mean-square height was largest under lower air velocities, lower air temperatures, lower wall temperatures, and higher relative humidities. Larger frost surface skewness occurred under lower air velocities, lower air temperatures, higher

wall temperatures, and higher relative humidities. The impacts of increasing relative humidity on the frost roughness parameters plateaued at higher relative humidities.

Key Words

Frost crystal, frost thickness, frost surface skewness, frost roughness height

Nomenclature

T_{air} = Air temperature

V_{air} = Air velocity

T_s = Wall surface temperature

RH = Relative humidity

T_{fst} = Frost surface temperature

RMS = Root-mean-square

N_p = The number of points in a surface point cloud

R_q = Root-mean-square roughness height

Skw = Skewness

Z(x,y) = Surface elevation at a point

$\bar{Z}$ = The mean surface elevation, $= \frac{1}{N_P}\sum_{i=1}^{N_P} Z_i$

Introduction

Frost formation on a cold surface in many refrigeration and heat pump applications usually starts with condensation of water droplets and the subsequent freezing of these super-cooled droplets [17]. Initial frost crystals then emerge on the frozen condensate droplets. As the frost crystals continue to grow and connect with each other, a porous frost layer with a rough surface eventually forms. Researchers [3-8, 14]

have indicated that air velocity (V_{air}), air temperature (T_{air}), wall temperature (T_s), and air humidity (RH) affected the microstructure and properties of frost deposited on a cold surface. Typically, higher air velocities, lower air temperatures, lower wall temperatures, and higher air humidities lead to higher frost thickness.

The initial crystals vary in shape and depend on the ambient cold wall temperature (T_s) and the water vapor concentration difference (ΔC) between the free stream (C_∞) and the cold wall surface (C_s) [17-19]. Later, Leoni et al. [4] provided suggestions on modifying this initial frost crystal formation map when analyzing the frost conductivity from the perspective of frost crystal formation. They set the frost surface temperature as the reference temperature (y axis value) for heat and mass transfer at the interface, instead of the cold wall temperature. In this way, a relationship between the frost surface temperature (T_{fst}) and frost crystal shapes was developed. Therefore, the frost crystal type on the frost layer surface could be predicted by using the frost surface temperature and the water vapor concentration difference between the free stream and the frost surface.

In engineering systems, such as evaporators, piping, and aircraft wing surfaces, frost with a roughness can have significant effects on fluid flow and heat transfer in these systems. Chen and Rohsenow [1] investigated the pressure drop on a frosted pipe and found that the measured pressure drop was greater than the expected pressure drop caused only by the flow area reduction caused by the frost. The authors indicated that these observed trends were attributed to the frost surface roughness which increased turbulence levels of the air on the surface. The interactions between the air stream and the

frost surface generated an additional frictional force due to the roughness. That force restricted air flow across the surface.

Dietenberger [2] conducted a study of frost roughness impacts on takeoff aerodynamic performance of aircrafts. Under different frost roughness heights (0.1 to 1.0mm), three aerodynamic parameters were measured: relative lift coefficient degradation ($\Delta C_L/C_L$), relative attack angle increment ($\Delta\alpha/\alpha$), and drag coefficient increment (ΔC_d). The results pointed out that when the frost roughness height was 1.0 mm, the reduction of maximum lift coefficient was as high as 33.3% and the reduction of maximum angle of attack was as high as 24.1%. These reductions generated by frost roughness were undesirable because they would significantly impact the performance of an aircraft during takeoff.

Although the importance of frost roughness has been well acknowledged in the literature, there are few studies that have evaluated frost roughness. Yun et al. [31] proposed an empirical correlation of frost roughness as a function of time when conducting experiments on a flat plate at subfreezing temperatures. They indicated that frost increased in roughness rapidly during the crystal growth period and was gradually reduced with time during the frost layer growth period. The authors also described the frost roughness change through analyzing the initial frost crystal types: needle type crystals grew almost normal to the frost surface so that a rough frost was formed; plate type crystals made the frost layer dense and flat. Nevertheless, Yun's correlation was only a function of time, but did not explore the impacts of environmental conditions on frost roughness formation.

Frost roughness is difficult to measure because the structure of frost is delicate, temperature sensitive, and partially transparent. Any physical contact with the surface or thermal effects from a measurement operation would disrupt the status of frost surface. Conventional noncontact methods, such as a laser scanner [68], electromagnetic wave interferometry [69], and chromatic confocal profilometry [70] lack adequate accuracy with semi-transparent objects such as frost crystals. Additionally, white paint needs to be applied to the measured surface to reduce the reflection of light from a laser scanner. The paint changes the frost surface, which reduces the accuracy of the laser measurements and changes the results of frost roughness characterizations.

With the development of observational and computational technologies, 3-D photogrammetry has been gradually applied to derive the spatial and geometrical information of objects. In 1985, Mikkelson et al. [71] used two cameras to capture peaks and valleys of ice formed on the wing of an aircraft. An analytical plotter was then used to obtain a measurement of ice surface roughness. Later, Collier et al. [72] utilized close-range photogrammetry to build a 3-D model for studying ice accretion over time. Recently, Miyauchi et al. [33] demonstrated and validated a measurement method using structure-from-motion photogrammetry [34] to fulfill the purpose of nonintrusive and in-situ measuring of the frost roughness on a closed-loop psychrometric wind tunnel. This was a noncontact method and required rapid data acquisition. This approach was non-intrusive and did not impose any direct impacts on the frost surface, structure, or temperature when frost was grown over a wide range of environmental conditions. Two primary parameters of frost roughness statistics, the root-mean-square (RMS) height and skewness were calculated to represent the spatial geometry of frost surface.

In this study, a series of laboratory experiments were conducted to characterize frost roughness formation under various atmospheric conditions. Frost roughness was measured by applying the 3-D photogrammetry method from Miyauchi et al. [33]. The experimental data was analyzed to develop a relationship between atmospheric conditions and frost morphology. Collectively, the significance of each atmospheric factor was presented, and the factors affecting frost roughness formation were identified.

Methodology

Experimental Apparatus

To investigate frost roughness, a closed-loop psychometric wind tunnel system was employed in this study. The system had several modular sections, including air humidity control module with an ultrasonic humidifier and a dry gas (pure nitrogen) injection system, air temperature control module with two cooling coils and a duct heater, air velocity control module with an adjustable electronically commutated motor blower, and a test section where experimental data were collected and the surface temperature is controlled. The whole wind tunnel system could provide continuous, conditioned airflow over an interchangeable test surface mounted to the top side of the thermal stage.

The test section had an optical transparent panel (acrylic glass with 0.2 W m^{-1} K^{-1} thermal conductivity) which allowed for in-situ, vertical and horizontal viewing in the microscopy system without disruption to the experimental process. Figure 4.1 shows the detailed schematic of the test section. Conditioned air was split into two flow paths when entering the test section: a portion of the air flowed into the upper acrylic duct through a rectangular annulus (with 15 mm by 60 mm) while the rest of the air was diverted into

the bypass duct. The annular construction insulated the entry region of the test section and ensured the temperature of the air inducted over the test surface was uniform. At the upstream of the test section, a relative humidity sensor and a type-T thermocouple were used for the measurement of the relative humidity and air temperature, respectively. A hot wire anemometer was mounted at the downstream of the test surface for the measurement of the air velocity. An example of the vertical air velocity distribution is given in Figure 4.2.

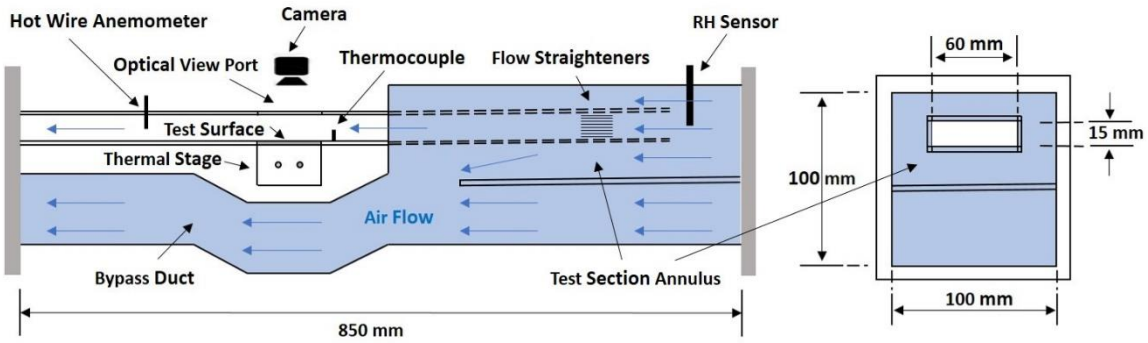

Figure 4.1. A detailed schematic of the test stage.

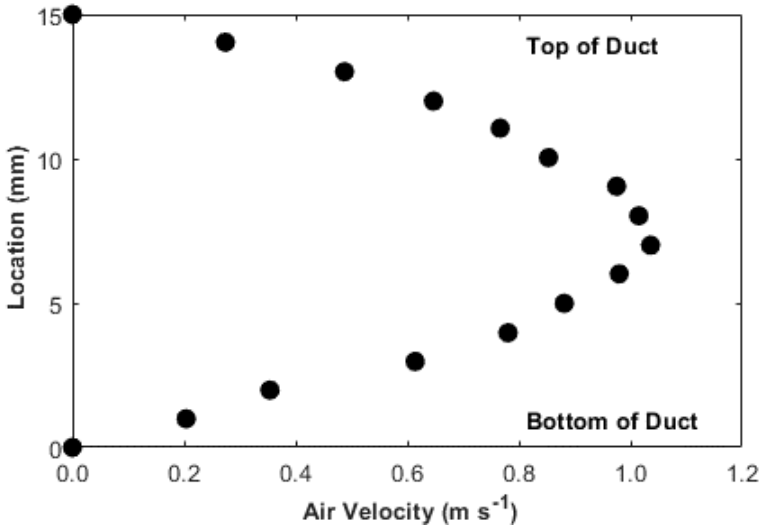

Figure 4.2. An example of the vertical air velocity distribution at V_{air} 1.0 m s^{-1}.

At the center of the test section, a thermal stage was bonded with an aluminum test surface (3 cm by 3 cm) through a thermally conductive material (with 0.254 mm thickness and 3.0 W m^{-1} K^{-1}) thermal conductivity). The stage consisted of a thermoelectric cooler, a type-T thermocouple, and a copper heat sink with an internal circuit. The polarity of the thermoelectric cooler was controlled by an electromechanical switch to fulfill the alternate between cooling and heating modes. The heat generated by the thermoelectric cooler was conducted through the copper heat sink. During the entire frosting experiments, the thermal stage was automatically controlled by a NI LabVIEW program to maintain the wall surface temperature constant as demanded. Moreover, a Digi-Sense traceable dual-laser infrared thermometer was employed for the frost surface temperature measurements from the top of the test surface.

Measurement of Frost Thickness

A Nikon D3400 DSLR camera with an AF Micro Nikkor 60mm f/2.8D lens was applied to accomplish non-contact and in-situ thickness and roughness measurements. The camera was set at 1.0x reproduction ratio. The subject in the plane of focus was identical in size to the image sensor size, which was 23.5 mm by 15.6 mm. This feature of the camera provided an approach for the measurement of captured items. A multi-axial traversing system, which consisted of a telescoping boom stand and two positioning slide plates, was used to traverse the Nikon camera in the x and y direction and focus the camera in the z-direction. A two-degree-of freedom telescoping boom stand supported the camera system and allowed observation of the experimental process from the lateral or top viewport of the test section.

To measure the frost thickness, a reference image was first captured before frost formation occurred. This image was used to identify the reference height before frost growth. Subsequently, a series of frost height images were taken as the frost formed and grew on the surface. These images had an average resolution of 255 pixel per mm. By applying ImageJ software, the pixel changes of frost growth from the reference image to the new frost-air boundary line in the frosted surface images would be measured to calculate the increase of frost thickness.

Measurement of Frost Roughness

The frost roughness measurement was accomplished through a 3-D photogrammetric method. The same camera system used in frost thickness measurement was applied here. Instead of a lateral side observation, the camera was mounted on the top of the test section. Conventional roughness measurements of frost formed on a flat plate was based on a 2-D surface profile generated during thickness measurements. However, the freezing process around the edge of the flat plate began earlier due to nonhomogeneous nucleation. The 2-D surface profile produced an overlapped view of the frost located in different distances from the camera. Hence, the conventional horizontal observation method of frost roughness measurement could generate unreliable measurements of frost roughness. A complete and detailed description of this 3-D method can be found in Miyauchi et al. [33].

At the start of data acquisition, a cyclic operation began of capturing a photo with a remote sensor and traversing the camera. Between the moments of capturing images, the camera was traversed approximately 2.15 mm along the positive y-direction for acquisition of 10 images, and then crossed approximately 4.45 mm along the positive x-

direction for one repetition. Next, the image capturing cycle was repeated in the negative y-direction. A total of 4 columns of 10 images were acquired during the entire image capturing procedure. The approximate time for capturing all 40 images was 45 seconds. In addition, a scale bar was applied to the images to provide a reference for scaling the entire model to the correct units.

The data images collected from the tests required post processing to achieve detailed height distributions and roughness parameters. First, photogrammetric software (Agisoft Photoscan Pro) was used to produce a preliminary point cloud file. Next, a matrix-based programming platform (MATLAB) made corrections to the point cloud. From the correctly scaled dense point cloud model, surface roughness analysis could be estimated. The RMS height and skewness were then computed. The RMS height (R_q), as described in Equation 4.1, represented the standard deviation of height from the mean surface value.

$$R_q = \left[\frac{1}{N_P}\sum_{i=1}^{N_P}(Z_i - \bar{Z})^2\right]^{\frac{1}{2}} \tag{4.1}$$

The skewness (Skw), as described in Equation 4.2, represented the symmetric distribution of the surface about the mean surface. This parameter indicated whether the frost surface had more peaks or valley. For example. a positive skewness presented a frost surface had more frost peaks than valleys.

$$Skw = \frac{1}{{R_q}^3}\left[\frac{1}{N_P}\sum_{i=1}^{N_P}(Z_i - \bar{Z})^3\right] \tag{4.2}$$

The advantage of using RMS height and skewness to represent surface roughness was that they were widely employed in calculating the equivalent sand-grain roughness height, which can be applied to study the effects of roughness on surface aerodynamic performance.

Experiment Procedure

The experiments were carried out on a 3 cm by 3 cm polished aluminum surface (74.6° static contact angle). Surface temperatures ranged from -25 to -15°C, free stream temperature from 6 to 16°C, relative humidity from 50 to 75%, and air speeds from 0.5 to 1.5 m s^{-1}. Table 4.1 listed the accuracy of measurements and uncertainties of process in this study.

Table 4.1. Accuracy of measurements and uncertainties of process

Parameter	Control Accuracy
Air Velocity	± 0.05 m s^{-1}
Air and Wall Temperature	± 0.5°C
Relative Humidity	± 2%
Frost Surface Temperature	± 0.83°C
Frost Roughness	± 7%
Frost Thickness	± 0.1 mm
Frost Density	± 0.02 kg m^{-3}

The thermoelectric cooler was maintained in heating mode before environmental conditions reached the target setting, then switched to the cooling mode to decrease the wall surface temperature down to the target wall temperature within 10 seconds. When the wall temperature reached steady state, it was marked as the initial time. Each frosting test was run for one hour. Frost roughness images were captured every 15 minutes as well as the frost surface temperature. A NI LabVIEW program was employed during the entire frosting tests to monitor and control all the environmental parameters.

Results and Discussion

Frost Crystal Type

For all test cases, the air dew point temperatures were above the freezing point, which meant that frost initially started with water droplet condensation, then ice nucleation, and eventually frost crystal growth. Frost crystals growing on top of a frost layer consisted of the morphology of a frost surface. The type and distribution of these frost crystals vary with time and environmental conditions. An example of the change of frost crystals on top of the frost layer is shown in Figure 4.3. The example was tested under an air velocity of 1.0 m s^{-1}, air temperature of 16°C, wall temperature of -25°C, and relative humidity of 75%. One can observe that frost crystals formed on frozen water droplets condensed during the initial period on the cold wall surface. As time increased, the type of frost crystal changed from feather crystal to a needle shaped crystal, and then to flake or even irregular shaped crystals. Generally, the feather crystals appeared at frost surface temperatures from about -25 to -15°C. These crystals had fast growing branches which produced large size crystals (about 0.7 mm). Feather crystals mainly extended normal to the cold wall surface and left many voids (valleys) between the crystals. As the frost surface temperature increased, needle crystals formed. They all grew mainly in the axial direction. Lastly, flake and irregular crystals then appeared under frost surface temperatures higher than about -7°C. Unlike column shape crystals, flake and irregular crystals presented plate-like growth patterns and had quite small dimensions (lower than 0.2 mm). These thin hexagonal plates were close to each other or even overlapped each other. The size of the frost crystals became smaller and smaller while the main growth

pattern of frost crystals varied from column shape to plate shape. Eventually, all these changes contributed to the frost thickness and roughness formation.

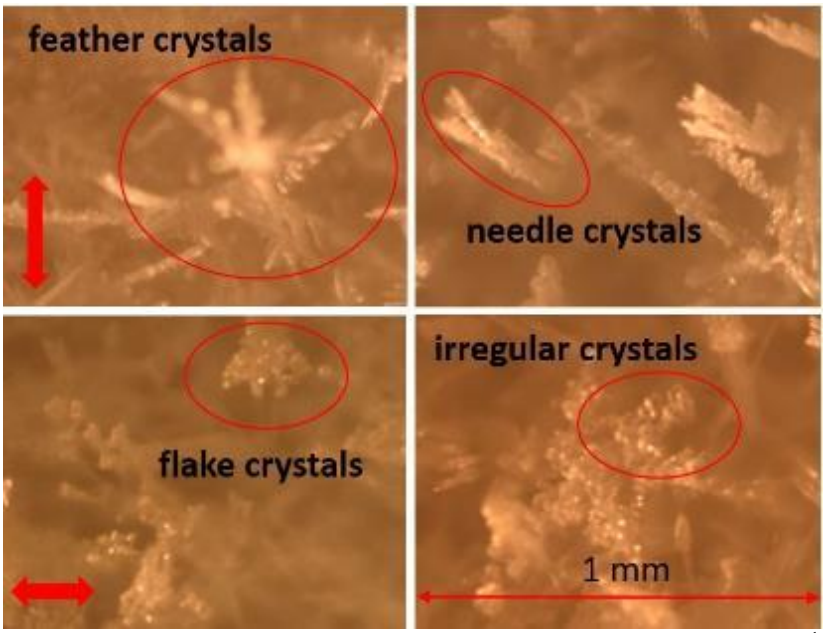

Figure 4.3. Frost crystals on the top of frost layer formed under V_{air} 1.0 m s^{-1}, T_{air} 16°C, T_s -25°C and RH 75%.

Figure 4.4 shows the variation of frost thickness and frost surface temperature for the case with an air speed of 1.0 m s^{-1}, air temperature of 16°C, wall temperature of -25°C, and relative humidity of 75%. As the frost grew, the frost surface temperature increased from -25 to -5°C, which led to the changes in frost crystals from feather shape to flake shape. Correspondingly, the rate of growth of the frost thickness with time decreased. This decrease can be seen by looking at the slope between the points of frost thickness over time. Larger size crystals, like feather crystals, formed at a frost surface temperature below -15°C and resulted in a faster frost growth rate (0.16 mm min^{-1}). Alternatively, smaller size crystals, like flake and irregular crystals, generated at frost surface temperatures above -7°C corresponded to a lower frost growth rate of 0.02 mm

min^{-1}. The impact on frost thickness under different wall temperatures is shown in Figure 4.5. This figure also illustrated the effects of frost crystal type on frost growth speed. Other environmental parameters were kept constant (air speed of 1.0 m s^{-1}, air temperature of 12°C, and relative humidity of 75%). Compared to the feather crystals formed at T_s -25°C, frost formed at T_s -15°C was primarily needle crystals which were not as tall during the initial period of frosting but had a larger density at the end of the one-hour test. As the wall temperature increased from -25 to -15°C, at 60 min, frost thickness decreased from 3.76 to 2.93 mm while frost density increased from 94.3 to 105.1 kg m^{-3}.

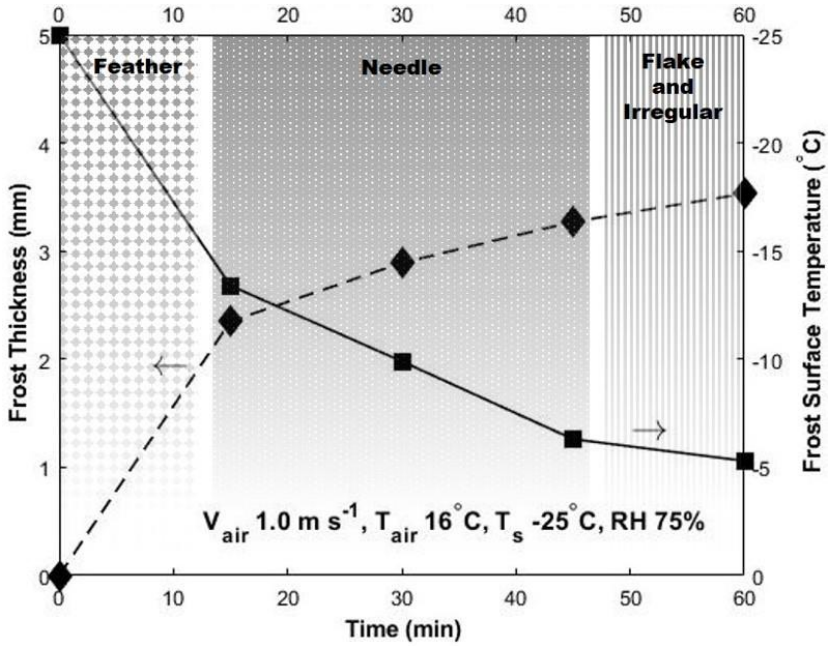

Figure 4.4. Frost thickness and frost surface temperature for the case under V_{air} 1.0 m s^{-1}, T_{air} 16°C, T_s -25°C and RH 75%.

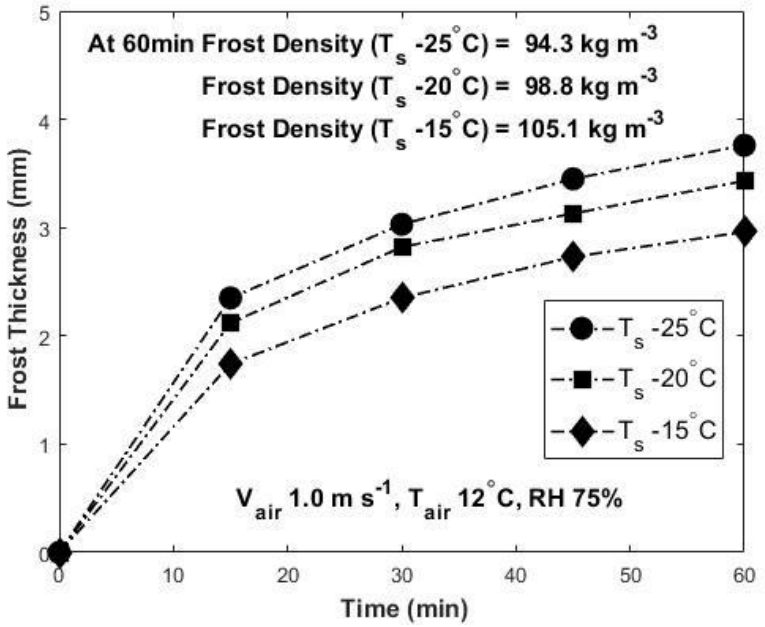

Figure 4.5. Frost thickness for the cases under T_s -15°C, -20°C, and -25°C.

Besides the effects of frost crystal type on frost thickness growth, the variation of frost crystal shapes can also influence the frost surface roughness. Take the frosting case in Figure 4.3 as an example. At the beginning of testing, frost grew initially as feather crystals. Due to the irregular shape of feather crystals, the frost layer formed a rough surface. When needle crystals appeared, these sharp tips created more peaks on the frost surface. As time increased, flake or irregular crystal gradually smoothed the frost surface because of their small sizes and plate growth pattern. During the whole frosting process, the environmental conditions greatly impacted the type of frost crystals, which directly determined the roughness of the frost surface. Moreover, distance between frost crystals, as well as frost crystal size, can also be influenced by environmental conditions and then affect surface roughness of frost. More details on the effect of the environmental conditions are discussed in the following sections.

Air Velocity

To determine the effect of air velocity on frost surface roughness, tests were performed at air velocities of 1.5 m s^{-1}, 1.0 m s^{-1}, and 0.5 m s^{-1}. Other environmental parameters were kept constant: air temperature of 12°C, wall temperature of -25°C, and relative humidity of 75%. Frost surface temperature and surface roughness were measured every 15 min for one hour.

Frost surface temperature increased with time. At 60 min, the higher air velocity of 1.5 m s^{-1} caused a greater frost surface temperature, T_{fst} of -7.8°C compared to the T_{fst} of -9.9°C for the air velocity case of 1.0 m s^{-1} and the T_{fst} of -11.8°C for the air velocity case of 0.5 m s^{-1}. Correspondingly, frost crystal type for the air velocity case of 1.5 m s^{-1} quickly changed from feather shape and needle shape to flake or even irregular shape, as shown in Figure 4.6. At 15 min, the frosting crystal type for air velocity of 1.5 m s^{-1} had already presented needle shapes while the crystal types of frosting for an air velocity of 0.5 m s^{-1} was still mainly feather crystals. At 60 min, for an air velocity of 1.5 m s^{-1}, a partial zone of frost had appeared with flake crystals while the frost in the air velocity case of 0.5 m s^{-1} still fully grew with needle shapes. Due to the large size and column growth pattern of feather and needle crystals, the frost RMS height for an air velocity of 0.5 m s^{-1} (see Figure 4.7(a)), continuously increased to 0.67 mm at the end of the one-hour test. The RMS height for an air velocity of 1.5 m s^{-1}, however, reached its maximum (0.45 mm) at 15 min and then gradually decreased as frost surface temperature left the needle crystal formation region. In summary, higher air velocities can drive the frost RMS height to reach its maximum value in less time while lower air velocities can create a larger maximum RMS height.

Figure 4.7(b) shows the results of frost skewness under different air velocities. It can be seen that the surface skewness in the air velocity case of 0.5 m s^{-1} was large and positive (0.97) at 15 min, which indicated the frost surface had much more frost peaks than valleys. After that, the surface skewness dropped and eventually became a negative value which indicated the frost surface had more frost valleys than peaks. On the other hand, surface skewness in the air velocity case of 1.5 m s^{-1}, was small and negative. Its ranges were between 0.05 and -0.28. The phenomenon could be explained by the images of frost morphology shown in Figure 4.6. Both cases started from the formation of feather crystals with close crystal sizes. Frost crystals formed at an air velocity of 0.5 m s^{-1} were sparser than those with an air speed of 1.5 m s^{-1}. This sparse crystal distribution associated with the column growth pattern of feather crystal created many frost peaks which led to a large positive surface skewness. As frost crystals grew and interacted with adjacent crystals, the gaps between crystals were gradually filled. The frost peaks got small. Therefore, frost skewness decreased. For the air velocity case of 1.5 m s^{-1}, the upper-most part of frost grew as flake crystals for most of the time after the initial 15 min. Their plate growth pattern could smooth the frost surface and then create small frost skewness. In summary, crystal growth pattern and distribution collaboratively control the formation of frost surface skewness. Additionally, higher air speed tended to lead to a smaller frost skewness.

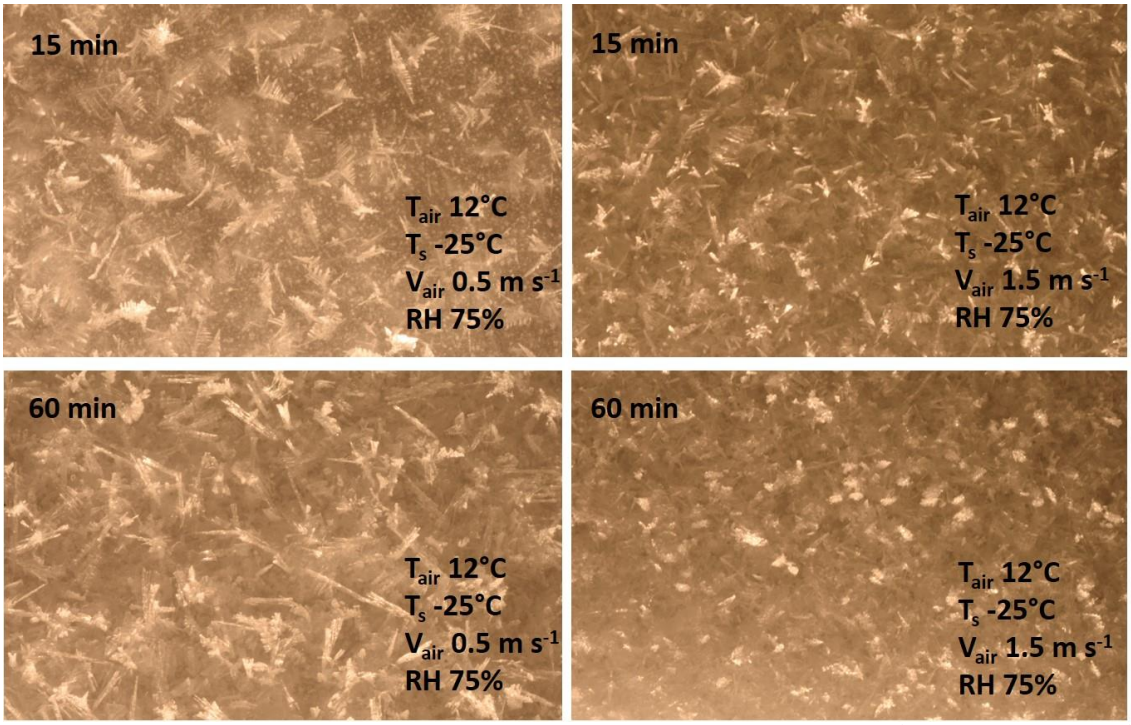

Figure 4.6. Frost morphology at 15 min and 60 min under V_{air} 0.5 m s^{-1} and V_{air} 1.5 m s^{-1}.

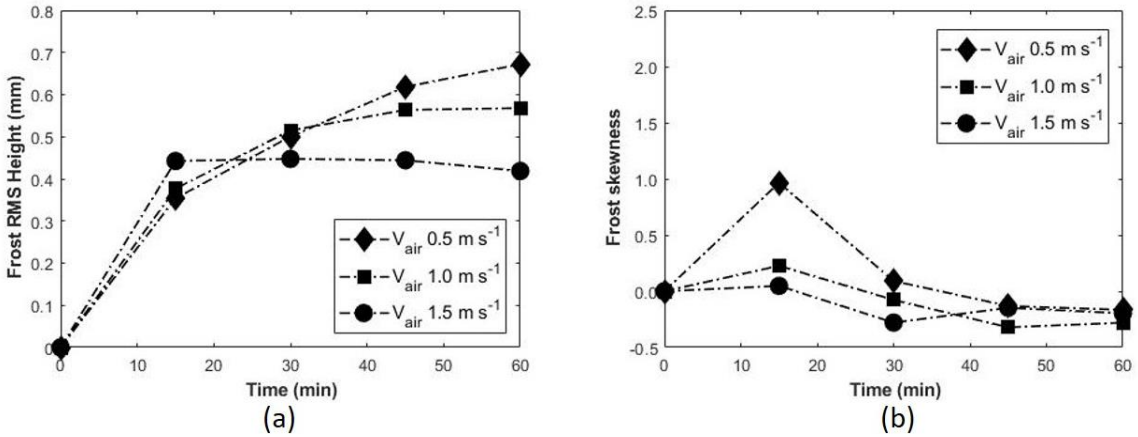

Figure 4.7. The effects of air velocity on (a) frost surface root-mean-square roughness height and (b) frost surface skewness.

Air Temperature

To determine the effect of air temperature on frost surface roughness, tests were performed at air temperatures of 16°C, 12°C, and 6°C. Other environmental parameters were kept constant: air speed of 1.0 m s^{-1}, wall temperature of -25°C, and relative

humidity of 75%. Frost surface roughness was measured every 15 min as well as frost surface temperature. Generally, increasing air temperature had similar impacts on frost surface temperature and frost roughness as increasing air velocity did.

Frost surface temperature increased with time. At 60 min, the highest air temperature of 16°C caused a greatest frost surface temperature of -5.3°C compared to a frost surface temperature of -9.9°C for the air temperature case of 12°C and frost surface temperature of -15.9°C for the air temperature case of 6°C. Therefore, for the high air temperature cases, the frost crystal type on the top of the frost surface quickly changed from feather to needle shape, and then to flake or even irregular shape, which had smaller sizes and a plate growth pattern. Figure 4.8 showed variations of frost crystal types under different air temperature. At 15 min, the frost crystal type of T_{air} 6°C stayed feather-shaped while the frost crystal of T_{air} 16°C changed from feather type to needle type. At 60 min, the frost under T_{air} 6°C grew with needle shape while the frost under T_{air} 16°C formed as flake crystals. As a result (shown in Figure 9(a)), the frost RMS height in the air temperature case of 16°C had a large value (0.42 mm) at 15 min and gradually decreased after the frost surface temperature was over the corresponding temperature of the needle crystal formation region. In contrast, the frost crystals in the air temperature case of 6°C were feather-shaped, and grew continually up to a RMS height of 0.69 mm at 60 min. In summary, higher air temperatures produce frost RMS heights that reach their maximum values earlier in the tests, while lower air temperatures created larger maximum RMS heights.

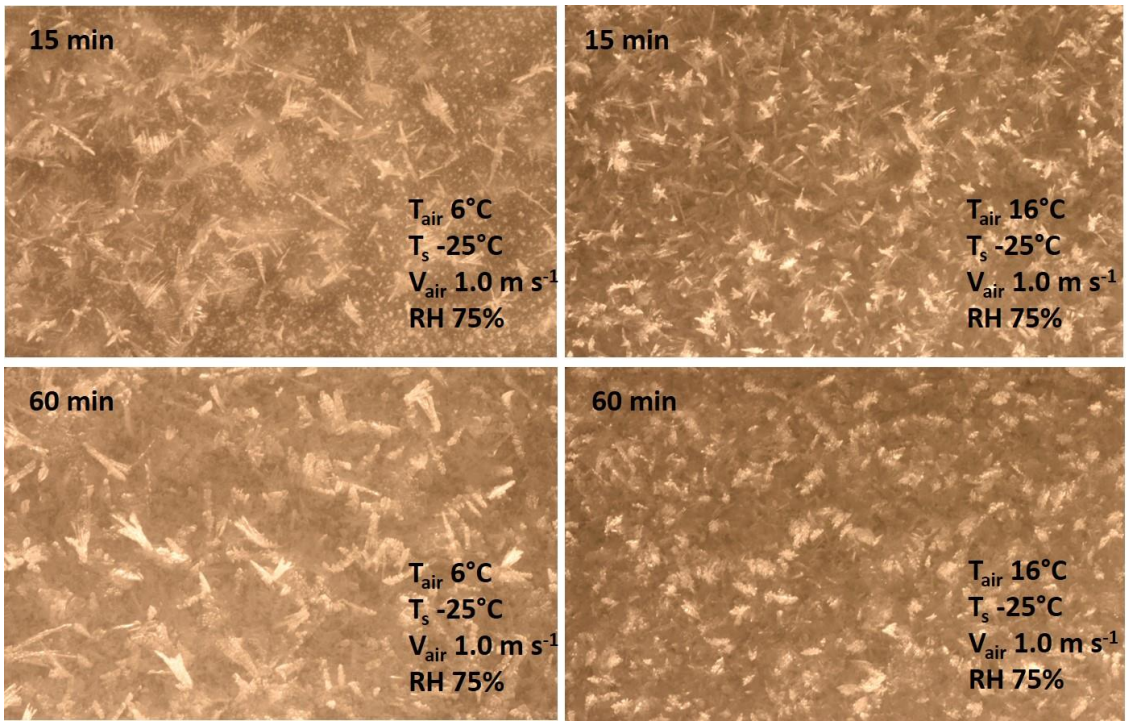

Figure 4.8. Frost morphology at 15 min and 60 min under T_{air} 6°C and T_{air} 16°C.

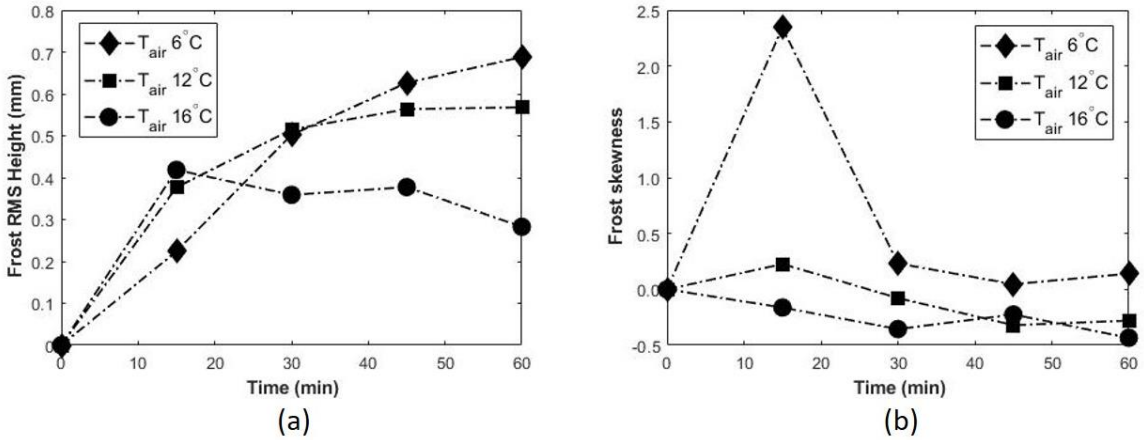

Figure 4.9. The effects of air temperature on (a) frost surface root-mean-square roughness height and (b) frost surface skewness.

The results of frost skewness under different air temperature are shown in Figure 4.9(b). The surface skewness in the air temperature case of 6°C had a large positive value (2.34) at the beginning and then significantly decreased. The frost surface skewness in the air temperature case of 16°C mostly remained negative, and reached -0.43 at 60

min. The reasons for this can be found in Figure 4.8. Both cases started from the formation of feather crystals with close crystal sizes. Frost crystals formed under an air temperature of 6°C were sparser compared to that for the case of air temperature of 16°C. This sparse crystal distribution as well as feather crystal type with column growth pattern created many frost peaks and then led to a large positive skewness in the case of an air temperature of 6°C. As frost crystals grew and interacted with each other, the gaps between crystals were gradually filled. The previous frost peaks got small. Therefore, frost skewness decreased. For an air temperature of 16°C, however, frost grew as flake crystals or even irregular crystals for most of time after the initial 15 min. Their plate growth pattern could erase the peaks formed by previous feather or needle crystals, and then created a negative frost skewness. Ultimately, crystal type and distribution collaboratively governed the formation of frost surface skewness. Higher air temperatures tended to lead to a negative frost skewness while lower air temperature tended to form a positive skewness.

Wall Temperature

To determine the effect of wall temperature on frost surface roughness, tests were performed at wall temperature of -25°C, -20°C, and -15°C. Other environmental parameters were kept constant, air speed of 1.0 m s^{-1}, air temperature of 12°C, and relative humidity of 75%. Frost surface roughness were measured every 15 min for a one-hour test duration.

Due to the difference of the initial frost surface temperature, the initial formed frost presented different crystal types and sizes. As shown in Figure 4.10, the frost crystal type for the wall temperature case of -25°C case was feather-shaped with large crystal

size. For the case of a wall temperature of -15°C, it was needle-shaped with small crystal dimensions. Consequently, as shown in Figure 4.11(a), at 15 min, a larger frost RMS height 0.38 mm was displayed for the case of wall temperature of -25°C, compared to 0.14 mm for the case of a wall temperature of -15°C. As the frost surface temperature increased, certain areas of the frost surface in both cases appeared as flake crystals, as shown in the cases of 60 min in Figure 4.10. Correspondingly, the frost RMS height either grew slowly or decreased. Overall, higher wall temperatures can let the frost RMS height reach its maximum value earlier while lower wall temperatures can create a larger maximum RMS height.

The frost skewness results obtained under different wall temperatures are given in Figure 4.11(b). The frost skewness in the wall temperature case of -15°C was greater than that of frost grown under wall temperature of -25°C. This scenario can be explained through the images of frost morphology shown in Figure 4.10 as well. Frost formed for a wall temperature of -15°C started growing in a relatively large number of needle crystals with sharper tips to obtain more peaks than valleys. On the other hand, frost in the wall temperature case of -25°C showed feather crystals with larger sizes and relatively small number of crystals. As a result, at 15 min, frost surface under wall temperature of -15°C had a larger frost skewness than that formed in the wall temperature case of -25°C due to the difference of the amount of frost peaks. As frost surface temperature increased, more and more plate type crystals formed on the top of the frost layer to gradually smooth the frost surface, and then reduced the frost surface skewness in both cases. In summary, within our testing range, a higher wall temperature tended to lead to a greater frost skewness.

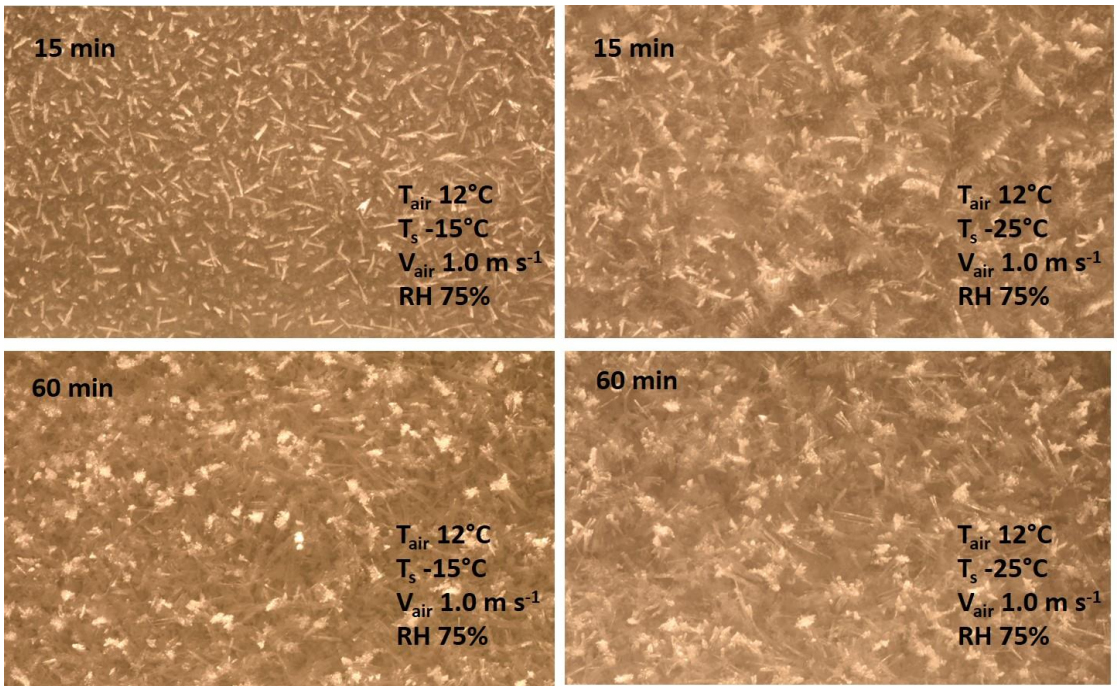

Figure 4.10. Frost morphology at 15 min and 60 min under T_s -15°C and T_s -25°C.

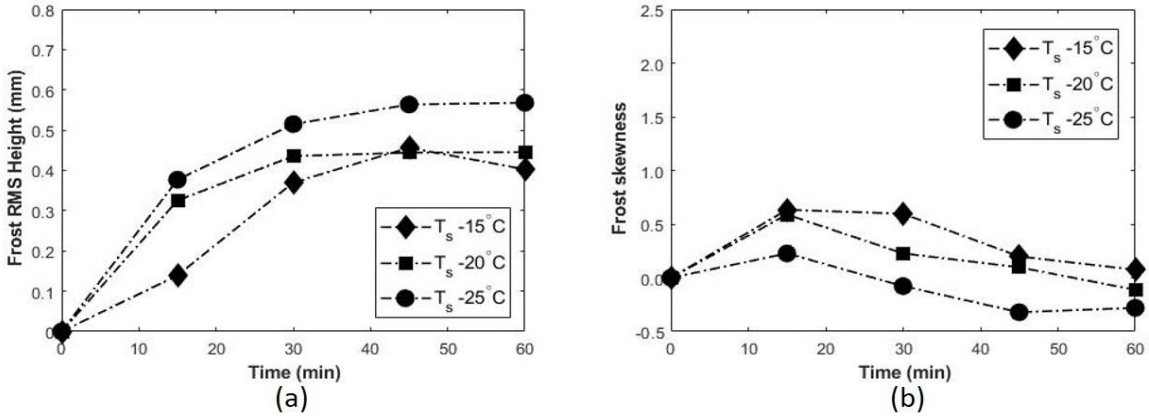

Figure 4.11. The effects of wall temperature on (a) frost surface root-mean-square roughness height and (b) frost surface skewness.

Air Humidity

To determine the effect of humidity on frost surface roughness, tests were performed at relative humidities of 50%, 65%, and 75%. Other environmental parameters were kept constant: air velocity of 1.0 m s^{-1}, air temperature of 12°C, and wall temperature of -25°C. Frost surface temperature and surface roughness were measured

every 15 min in a one-hour test duration. Generally, within our test range, relative humidity showed the weakest impact on frost roughness compared to the other three environmental parameters.

Frost surface temperature increased with time. Correspondingly, as shown in Figure 4.12, frost crystals on the top of frost surface changed from feather shape to needle shape as time increased from 15 min to 60 min. Frost crystal size tended to increase as relative humidity increased. This is clearly shown in the images captured at 60 min in Figure 4.12. Most of the frost crystals under RH 50% and 75% presented the same needle shapes. But crystals formed at RH 50% were shorter and narrower than those grown under RH 75%. A similar trend was also observed in images captured at 15 min. Overall, in the initial formation period, the frost RMS height of these three cases were similar, as shown in Figure 4.13(a). At the end of the hour-long test, the change in frost crystal sizes caused by increasing relative humidity created a RMS height 0.57 mm in the relative humidity case of 75%, but only 0.38 mm for the relative humidity case of 50%.

Figure 4.13(b) shows the results of frost skewness under different relative humidity. Frost skewness started increasing as frost formed on the cold surface. Frost skewness reached a maximum value of around 0.25, then began decreasing and eventually became negative. At the lower relative humidity of 50%, there was a smaller frost surface skewness during the whole test. The phenomenon could be explained by the difference in crystal size among the same shape frost crystals. When frost surfaces had similar frost crystal type and amount, the larger the frost crystal size, the higher the frost peaks, and the greater the surface skewness.

Additionally, from Figures 4.13(a) and 4.13(b), the frost RMS height increment created by the increasing relative humidity became limited when the humidity approached 75%. The change in frost surface skewness produced by increasing the relative humidity became small. More research is needed to reveal the exact mechanism causing insensitivity to the relative humidity at high values.

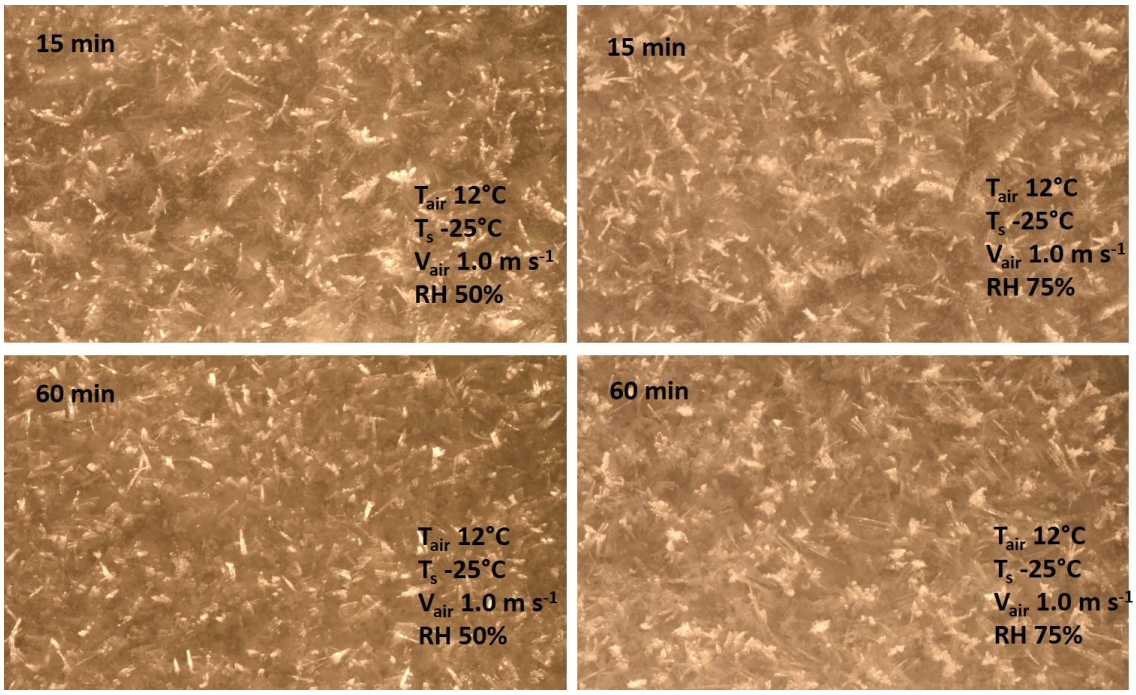

Figure 4.12. Frost morphology at 15 min and 60 min under RH 50% and RH 75%.

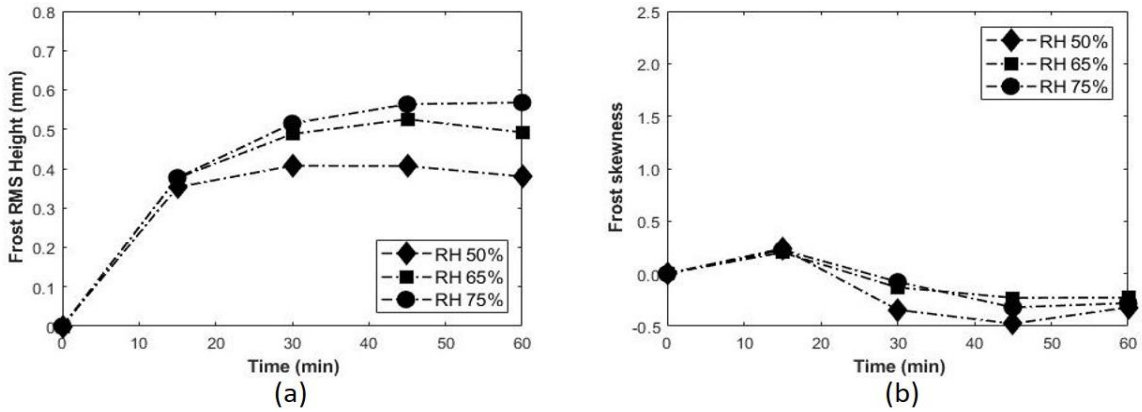

Figure 4.13. The effects of relative humidity on (a) frost surface root-mean-square roughness height and (b) frost surface skewness.

Conclusions

A series of frosting experiments were done on a cold flat plate under various environmental conditions covering wall temperature from -25 to -15°C, free stream temperature from 16 to 6°C, relative humidity from 50 to 75%, and air speed from 0.5 to 1.5 m s^{-1}. Frost roughness was measured and analyzed through 3-D photogrammetric method, which revealed more details of frost morphology.

As time increased, the frost crystal type on the top of the frost layer changed from feather-shaped to needle-shaped, then flake-shaped or even irregular-shaped. Feather and needle crystals with column growth pattern created a thick and porous frost layer with a rough frost surface. Flake and irregular crystals with plate growth pattern, however, formed a thin and dense frost layer, which smoothed the frost surface.

Frost crystal type, growth pattern, and distribution varied with changes in environmental conditions. High air velocity and high air temperature accelerated the change of frost crystal type from feather crystals to irregular crystals and made frost crystals appear closer to each other. Increasing relative humidity strongly enlarged frost crystal size, but slightly changed frost crystal type at the same time scale. Wall temperature dominated the initial frost crystal type which continuously affected the ongoing process of frost formation. Low wall temperature tended to create feather crystals of larger size, instead of a sharp needle crystal of smaller size.

Due to the variation of frost crystal formation on the top of frost layer, frost surface roughness presented diverse trends. Both frost RMS height and surface skewness continuously increased initially, and then gradually reached their maximum values. After passing through peak values, frost roughness parameters started decreasing.

Qualitatively, the frost RMS height decreased earlier when air velocity was higher, air temperature was greater, wall temperature was higher within our testing ranges. The maximum frost RMS height increased when air velocity, air temperature, and wall temperature decreased, and relative humidity increased. Larger frost skewness was related to environmental conditions with lower air velocity, lower air temperature, higher wall temperature, and higher relative humidity. Moreover, when relative humidity approached 75%, the frost roughness increments caused by increasing RH became limited.

Acknowledgements

The work in this paper were supported as part of FAA Grant 17-G-011. Any opinions presented in this paper are those of the authors and do not reflect the any official position of the U.S. Federal Aviation Administration or the United States government.

CHAPTER FIVE

Variation of Frost Roughness on a Flat Plate under Forced Convection
(In review, Journal of Thermal Science and Engineering Applications)

Abstract

Experiments were conducted on a cold flat plate to characterize the variation of frost roughness over both time and location on the surface. The testing conditions included air temperatures from 8 to 16°C, wall temperatures from -20 to -10°C, relative humidities from 60 to 80%, and air velocities from 0.5 to 2.5 m s^{-1}. A 3-D photogrammetric method was employed to measure the variation in frost root-mean-square height and skewness by location and time. These data were used to develop the equivalent sand-grain roughness for the frost at different locations and time. The experimental results showed that frost roughness varied by location and changed with time. For the environmental conditions in this study, relative humidity and air temperature were the most important factors determining changes in the peak frost roughness. For example, at an air temperature of 12ºC and surface temperature of -15ºC, the frost roughness peaked at about 40 minutes for a relative humidity of 80% and 90 minutes for a relative humidity of 60%. Empirical correlations were provided to describe the relationships between the environmental conditions and the appearance of the peak frost roughness.

Key Words

Frost roughness uniformity, empirical correlation, 3-D photogrammetry, flat plate

Nomenclature

ANOVA = Analysis of variance

D = hydraulic diameter

Fo = Fourier number

k_{ave} = Average of frost equivalent sand-grain roughness

k_s = Equivalent sand-grain roughness

k_{max} = Maximum value of equivalent sand-grain roughness

N_p = The number of points in a surface point cloud

Re_D = Reynolds number calculated by hydraulic diameter

RH = Relative humidity

RMS = Root-mean-square

R_q = Root-mean-square roughness height

Skw = Skewness

Std_ k_s = Standard deviation of frost equivalent sand-grain roughness

t = Time

T_{air} = Air temperature

T_s = Wall surface temperature

T_o = Triple point temperature

V_{air} = Air velocity

w_a = Absolute air humidity

Z_i = Surface elevation at a point

$\bar{Z}$ = The mean surface elevation, $= \frac{1}{N_P}\sum_{i=1}^{N_P} Z_i$

Introduction

Frost is a common phenomenon in nature as well as in engineering applications. When a cold surface with a temperature below 0˚C is surrounded with moist air, frost may deposit on the cold surface. In the past 70 years, researchers [3-14] have extensively investigated the dependence of frost growth under different atmospheric conditions. They indicated that air humidity, air velocity, wall temperature, and air temperature had primary impacts on the properties of frost.

Frost formation on a cold surface usually starts with the condensation of water droplets and the subsequent freezing of these super-cooled droplets [17]. Frost crystals then emerge from the top surface of the frozen condensate droplets. These crystals vary in shapes that are dependent on the ambient cold wall temperature and air humidity [17-19]. As the frost crystals continue to expand and interact with each other, a porous frost layer with a rough surface eventually forms. During this process of frost growth, moist air either deposits on the frost surface to increase the frost thickness or crosses the frost surface into the inner frost layer to increase the frost density [20-25].

Frost crystal structure can play an important role on frost formation. The initial porosity of the frost layer directly influences the frost layer characteristics [26]. The variation of frost crystal growth direction contributes greatly to the changes in frost growth rate [27]. Moreover, frost crystal shape was considered as a key factor affecting frost thermal conductivity [4]. Specifically, column shape crystals had higher heat conduction and led to a higher frost thermal conductivity compared to plate type crystals. In addition, the frost morphology changes were also associated with variation of frost crystal structure. As the frost grows, the frost crystal type on the top of the frost layer

might change from feather-shaped to needle-shaped and then to flake-shaped or even irregular-shaped during frosting. The different shapes of frost crystals propagating from the frost surface can produce a wide range in roughness [76]. Generally, frost crystals growing normal to the frost surface tended to form a rough layer; while frost with plate type crystals was likely to create a smoother frost layer [31].

The roughness of the frost surface can cause many undesirable impacts. It could increase the turbulence levels of air on the surface which can generate additional frictional forces and restrict air flow across the surface [1]. If frost is formed on a wing surface of aircraft, the additional roughness of frost could cause a reduction in the lift and a rise in drag[2]. For heat pump applications, frost with different frost morphologies has been shown to cause different air pressure drops even though the amounts of frost were equal [28].

Frost properties can present an uneven distribution along a plate when frost is formed on a cold flat plate under forced convection [8, 14, 35-38]. Cheng and Shiu [14] studied the spatial variation of the frost thickness on a cold plate. They found that at the leading edge of the cold plate, the frost crystals grew in the radial direction to form a 'round head' of the frost layer which had a smooth profile. In the downstream region, the frost crystals grew at approximately the same rate to form a homogeneous frost layer of uniform thickness. Some modeling studies [35-38] have also shown that frost density was non-uniform along the cold surface. In the frontal region, the water vapor mass fraction was higher, and the cold surface cooled the humid air to create a higher mass transfer of the moisture into the frost layer which led to denser frost. In the rear region of the frost layer, the gradient of the air humidity at the frost surface was smaller than the values in

the frontal region, and the frost density was smaller. Frost thermal conductivity can also be uneven along the cold surface due to the spatial variation of frost density [38].

Although the uniformities of frost properties, such as thickness, density, and thermal conductivity, have been investigated extensively, none of them have been related to frost surface roughness. The variation of frost surface roughness along with the cold plate has been not characterized. The uniformity of frost surface roughness, especially equivalent sand-grain roughness of frost, is another variable that is important in understanding the potential impact of frost on an engineered system such as a heat pump or refrigeration evaporator or aviation airfoil. Therefore, new data on frost roughness can potentially help engineers in designing these systems.

Conventional methods of frost roughness measurements [31, 32] have used lateral side 2-D frost surface profiles. Frosting usually presents nonhomogeneous nucleation along the edges of test surfaces. Moreover, the lateral side profiles included an overlapped view of frost formed at different distances from the camera. These profiles might not represent the actual distribution of frost crystals over the whole frost surface. Another approach of frost roughness measurement was to apply 3-D photogrammetry. In 1985, Mikkelson et al. [71] used two cameras to capture peaks and valleys of ice formed on the wing of an aircraft. Image data were further processed by using an analytical plotter to derive the spatial and geometrical information of ice surface. A similar concept of 3-D close-range photogrammetry was later applied by Collier et al. [72] to build a 3-D model of accreted ice. Recently, Miyauchi et al. [33] developed a 3-D photogrammetric method for nonintrusive and in-situ measuring of the frost roughness on a closed-loop

psychrometric wind tunnel. Because the process was nonintrusive, it did not interfere with the growth of the frost on the cold surface.

In this study, the 3-D photogrammetry was applied for the measurement of frost roughness. The overall objective of this study was to characterize the surface roughness of frost formed on a flat plate under forced convection as a function of location and time. Several environmental conditions were varied, including air temperature, air humidity, air velocity, and wall temperature.

Methodology

Closed-loop Psychrometric Wind Tunnel

A closed-loop psychometric wind tunnel system was used to provide conditioned airflow over a cold test surface. Figure 5.1 shows the schematic drawing of the wind tunnel system. An ultrasonic humidifier with the use of a dry gas (pure nitrogen) injection system were applied to precisely control the air humidity in the wind tunnel. An adjustable electronically commutated motor blower was employed to vary the air velocity in the closed loop. Two cooling coils and a duct heater were used to carry out the control of air temperature. In addition, a thermal stage mounted in test section was utilized to precisely control wall temperature as needed.

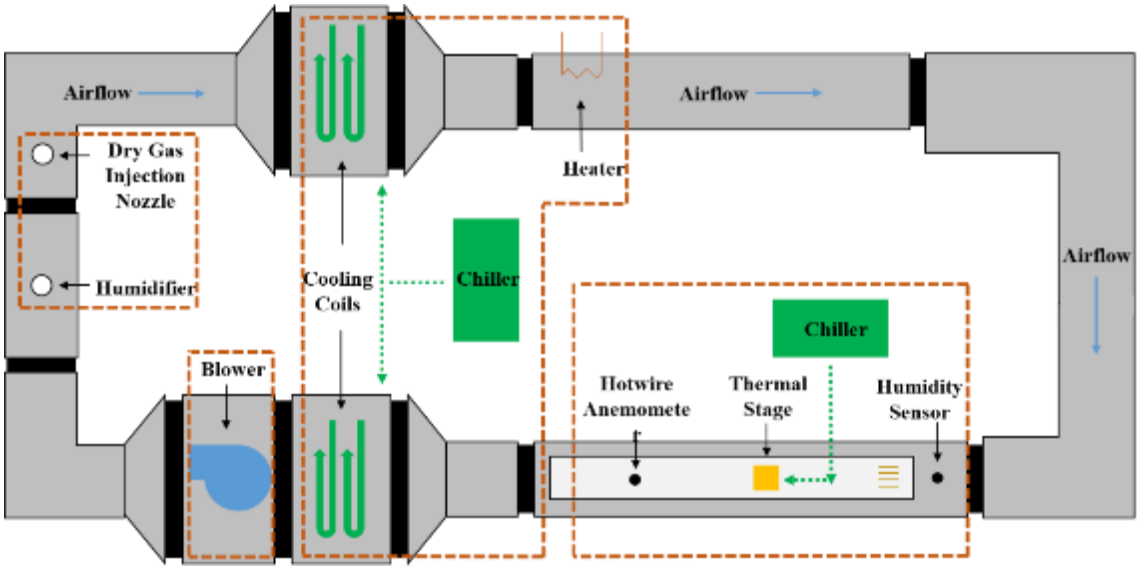

Figure 5.1. Schematic overview of the wind tunnel loop system.

A detailed schematic of the test section is presented in Figure 5.2. The test section was made of an optical transparent acrylic glass with 0.2 W m^{-1} K^{-1} thermal conductivity. This panel allowed for in-situ, vertical and horizontal observations of experimental processes without any disruption. Conditioned air coming into the test section was split into two flow paths by a rectangular annulus (15 mm by 60 mm) and a bypass duct: the upper portion flowed into the acrylic panel and crossed over a chilled aluminum test surface (3 cm by 3 cm) while the rest of the air crossed through the lower duct and by-passed the test section. The air temperature was measured by a type-T thermocouple located upstream from the test surface. A Vaisala HMT-333 series relative humidity sensor was used for the measurement of relative humidity. A TSI 1750 constant temperature hot-wire anemometer (model 1201 sensor probe) was applied to measure the air velocity. At the center of the test section, a thermal stage was bonded with the aluminum test surface through a thermally conductive material (with 0.254 mm thickness and 3.0 W m^{-1} K^{-1}) thermal conductivity). The thermal stage consisted of a type-T

thermocouple, a thermoelectric cooler, and a copper heat sink. During testing, the wall surface temperature was precisely adjusted as needed by the thermal stage using a NI LabVIEW program.

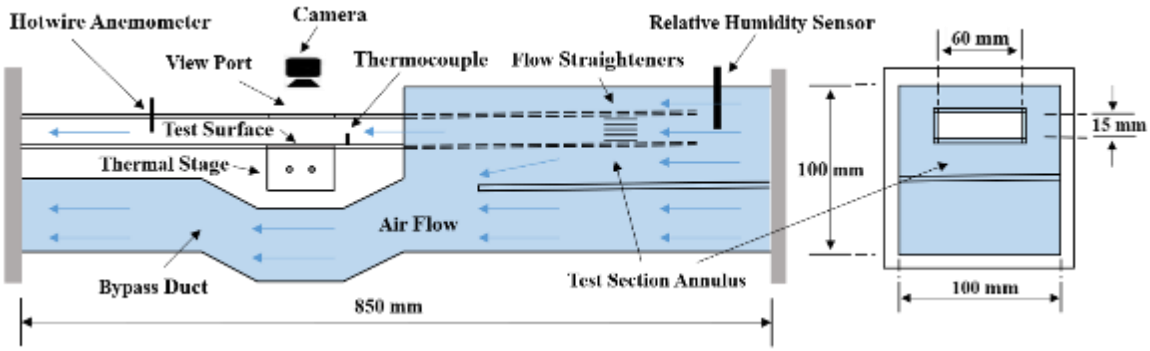

Figure 5.2. A detailed schematic of the test section.

Frost Equivalent Sand-grain Roughness Measurement

Equivalent sand-grain roughness was the parameter used to represent the surface morphology of frost formed on the tested plate. Equivalent sand-grain roughness has been widely employed in studies of the effects of roughness on surface aerodynamic performance [73]. To measure frost surface roughness, a 3-D photogrammetric method developed by Miyauchi et al. [33] was applied. This approach was non-intrusive and did not impose effects on the frost surface, structure, or temperature when frost was grown over a wide range of environmental conditions.

Generally, the 3-D photogrammetric method was used to generate a 3-D digital model of frost surface based on multiple images of the frost surface. An example of an image layout is given in Figure 5.3. To capture these images of frost morphology, a Nikon D3400 DSLR camera with an AF Micro Nikkor 60mm f/2.8D lens was applied in this study. The whole camera system, supported by a two-degree-of freedom telescoping boom stand, was fixed above the top of the frost surface to observe the changes in the

characteristics of the frost surface. The camera was set at 1.0x reproduction ratio, ISO 200, and an aperture of f/22. At the beginning of data acquisition, the camera was manually traversed approximately 4.45 mm along the positive x-direction for acquisition of 7 images, and then crossed approximately 2.15 mm along the positive y-direction for one repetition. Next, the image capturing cycle was repeated in the negative x-direction. At the end of the image data acquisition, a total of 5 rows of 7 images were captured and saved on a computer. The whole image capturing procedure took about 45 seconds. During the procedure, an illuminator with two fiber optic guides was employed to provide lighting source from the lateral side of the test surface.

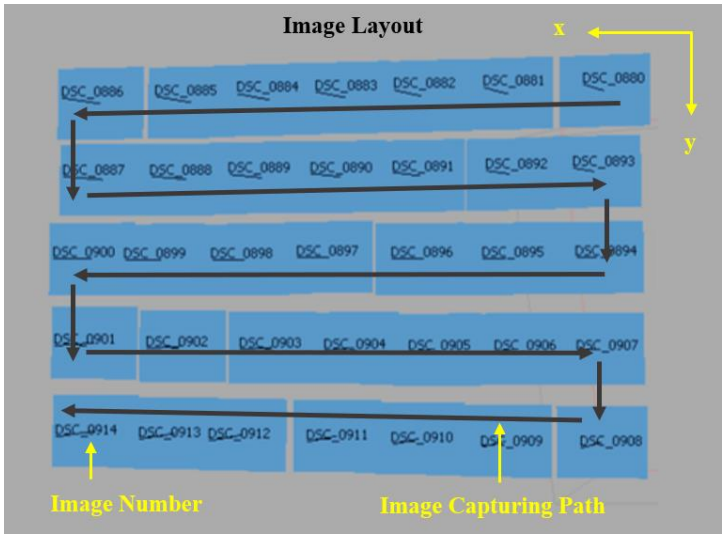

Figure 5.3. An Example of Image Layout.

The digital images of the frost surface needed had to be processed to generate a digital model of the frost surface by applying a commercial photogrammetric software, Agisoft Photoscan Pro [77]. Figure 5.4 shows an example of a frost surface model produced by using the image data of frost morphology. A 60-degree sloped scale bar with specks of black spray paint was placed near the x-direction edge. The specks of black

spray paint on the scale bar were used to create a reference for the horizontal x-y plane of the digital frost surface model in the software of Agisoft Photoscan Pro. On the other hand, the 60-degree slope of the scale bar was applied to correct units of the digital model in the vertical z-direction. The scaling process of the z-direction is described later.

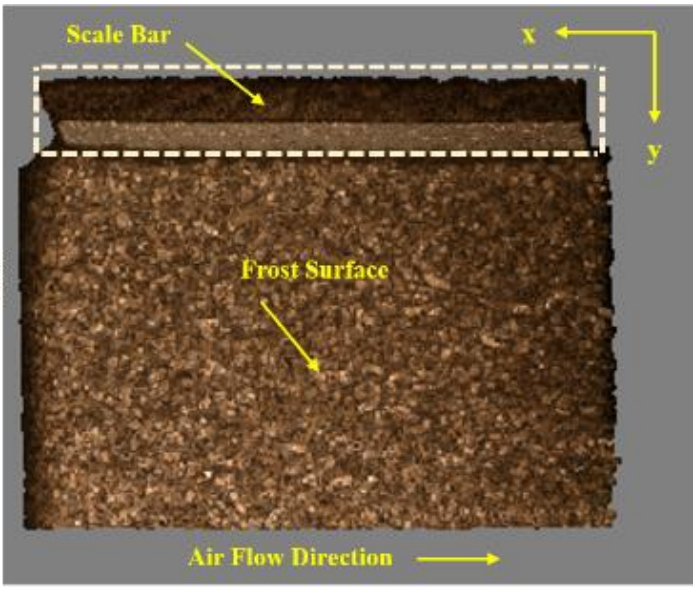

Figure 5.4. An Example of a Frost Surface Model Generated by Agisoft Photoscan Pro.

A text file with a point cloud of the frost surface was exported from the frost surface model generated by Agisoft Photoscan Pro. The point cloud was a set of data points of the external frost surface in space. This file was then processed by a MATLAB program to scale the model units in the z-direction through the reference information of the 60-degree slope of the scale bar. The scaling magnitude was determined by comparing the physical slope of the scale bar to the computed slope of the scale bar in the digital model. Thus, a detailed height distribution of frost surface was achieved from the correctly scaled txt data file, which would be used to calculate the root-mean-square

(RMS) height and skewness of frost surface. The RMS height (R_q), as described in Equation 5.1, represented the standard deviation of height from the mean surface value.

$$R_q = \left[\frac{1}{N_P}\sum_{i=1}^{N_P}(Z_i - \bar{Z})^2\right]^{\frac{1}{2}} \tag{5.1}$$

The skewness (Skw), as described in Equation 5.2, represented the symmetric distribution of the surface where a positive SSK indicated a frost surface had more frost peaks than valleys.

$$Skw = \frac{1}{{R_q}^3}\left[\frac{1}{N_P}\sum_{i=1}^{N_P}(Z_i - \bar{Z})^3\right] \tag{5.2}$$

In the last part, the calculation of equivalent sand-grain roughness height (k_s) was done by using the empirical formula (Equation 5.3) proposed by Flack and Schultz [73].

$$k_s = 4.43R_q(1 + Skw)^{1.37} \tag{5.3}$$

A detailed description of this 3-D photogrammetric method can be found in Miyauchi et al. [33].

The 3-D photogrammetry can overcome the difficulties generated by conventional 2-D roughness measurements [31, 32] using a surface profile from lateral edge of the flat plate. Figure 5.5 gives an example to show the difference of frost roughness observed from a lateral side 2-D frost surface profile (Figure 5.5(a)) and a 3-D frost surface elevation map generated by the photogrammetric method (Figure 5.5(b)). The lateral side profiles were an overlapped view of frost formed in different distances, which made the frost surface looked smoother. The 3-D frost surface elevation map could rebuild the

spatial morphology of frost to present these actual frost peaks and valleys. Hence, the data obtained from 3-D photogrammetry should be closer to the true roughness of the frost surface.

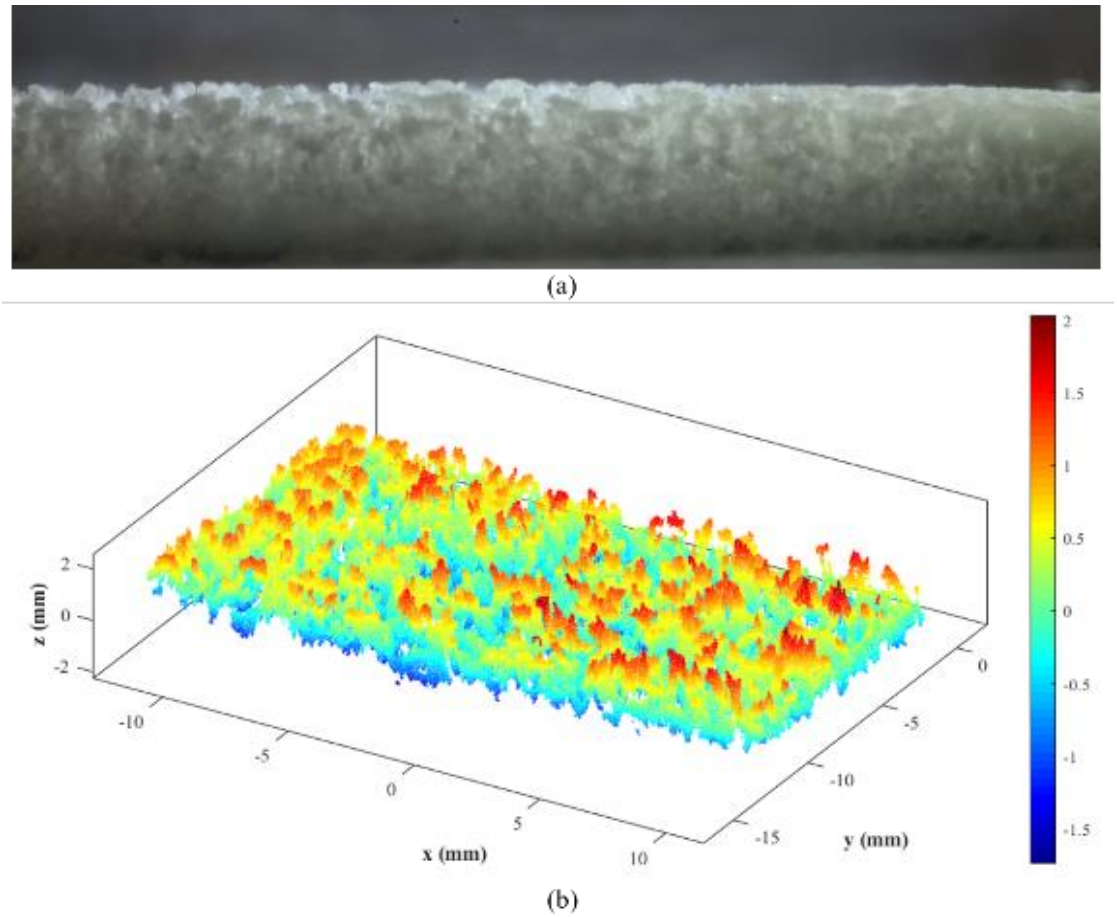

Figure 5.5. Frost surface observed from (a) a lateral side 2-D frost surface profile and (b) a 3-D frost surface elevation map generated by photogrammetric method (data were collected at 60 min under the testing conditions of T_{air} 12°C, T_s -15°C, RH 80%, and V_{air} 1.0 m s^{-1}).

Testing Procedures

The experiments were carried out over the following ranges: surface temperatures (T_s) from -20 to -10°C, free stream air temperatures (T_{air}) from 8 to 16°C, relative humidities (RH) from 60 to 80%, and air velocities (V_{air}) from 0.5 to 2.5 m/s. Table 5.1 gives the testing conditions as a function of surface temperature used in this study.

Table 5.1. List of experimental test conditions for the study of frost roughness variation

T_s (˚C)	T_{air} (˚C)	RH (%)	V_{air} (m/s)
-20			
-15	12	70	1.0
-10			
	16		
-15	8	70	1.0
		60	
-15	12	80	1.0
			0.5
-15	12	70	1.5
			2.5

To avoid any condensation before an individual frosting test started, the thermoelectric cooler was maintained in heating mode before the environmental conditions (air temperature, humidity, and velocity) in the wind tunnel reached their desired values. Once the steady state was achieved in the environmental conditions, the thermoelectric cooler was then switched to the cooling mode to quickly decrease the wall surface temperature down to the required value. This process usually took less than 10 seconds. A NI LabVIEW program was used to monitor and control all the environmental parameters. Each frosting test lasted for two hours. Frost surface images were captured every 15 minutes and then used for the calculation of frost equivalent sand-grain roughness height. Table 5.2 listed the estimated accuracy of the measurements.

Table 5.2. Accuracy of measurements for the study of frost roughness variation

Parameter	Control Accuracy
Air Velocity	$\pm$ 0.05 m s^{-1}
Air and Wall Temperature	$\pm$ 0.5°C
Relative Humidity	$\pm$ 2%
Frost Roughness	$\pm$ 7%

Results and Discussion

Frost Roughness Uniformity

For all frosting tests in this study, the dew point temperatures of air were above the freezing point. Hence, frost formation initially started with water droplet condensation, then freezing of super-cooled water droplets, and eventually frost crystals growing from the frozen water droplets. Frost crystals of different shapes grew on top of a frost layer, and thus produced a range in frost roughness.

Similar to the non-uniformed distribution of other frost properties found by previous investigations [8, 14, 35-38], the different types of frost crystals along the cold surface were observed in this study. Figure 6 gives an example of the frost crystal structure (or morphology) obtained at 45 minutes at an air temperature of 16°C, surface temperature of -15°C, relative humidity of 70%, and an air velocity of 1.0 m s^{-1}. In this figure, conditioned air entered from the left side. The entire frosted surface was divided into three parts: front region, center region, and rear region. The frost morphology shown in the frontal region was visibly different compared to that on the rest of the frost surface. Frost crystals near the leading edge had a cluster shape. These crystals were shorter and smoother compared with these needle-shaped crystals that appeared in the center and rear regions. This phenomenon was potentially caused by the variation of the air temperature and humidity gradients close to the frost surface. The gradient of air temperature and humidity in the frontal region should be greater than the those in the middle and back parts. The high gradient either melted the peaks of previous formed frost crystals or forced frost crystals to form a more clustered structure. As a result, a smoother frost layer was shown in the front region of Figure 5.6. Moreover, the type of frost crystal in the

center region in Figure 5.6, as well as the amount of frost crystals, were similar to these in the rear region.

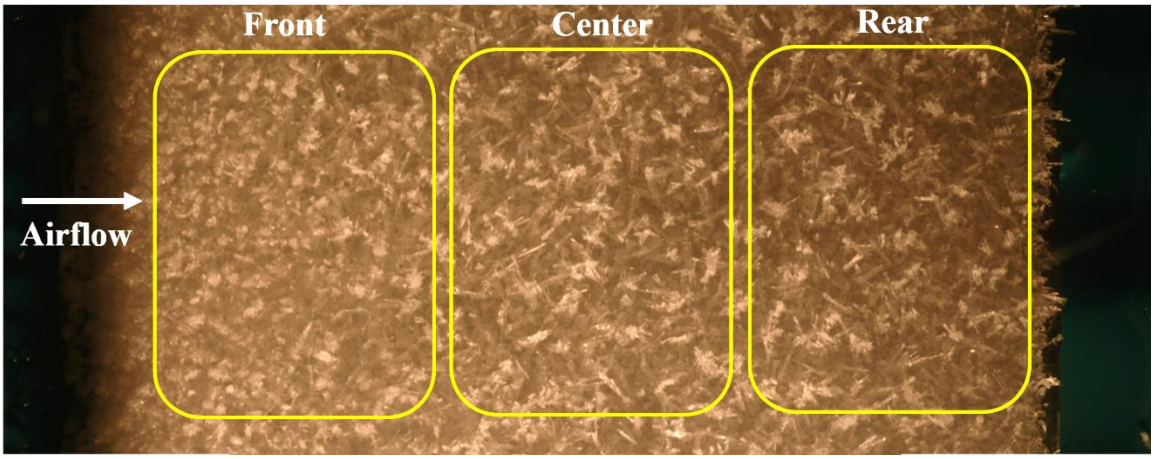

Figure 5.6. An example of frost morphology obtained at 45 min under T_{air} 16°C, T_s -15°C, RH 70%, and V_{air} 1.0 m s^{-1}.

The smoother frost surface nearer the front was observed in all the frosting tests. To quantitatively represent frost surface roughness, frost equivalent sand-grain roughness height (k_s) was used. Figure 5.7 provides an example of frost k_s variations with time under different air temperatures. At the front, center, and rear regions of the frost surface, frost k_s values might present similar growth trends. For example, in the air temperature case of 8°C, the frost roughness increased over time for the front, center, and rear regions with the frost roughness being largest at the end of 120 minutes for the center and read regions. In contrast at air temperatures of 12°C and 16°C (the bottom two plots in Figure 5.7), the frost in the front section was significantly smoother than either the center or rear and, with the exception at the beginning of the 12°C test, tended to decrease over time during the most of the tests. For both the 12°C and 16°C tests, both the center and read regions increased in roughness as measured in the k_s values reaching peaks of over 3 mm

at 12°C and nearly 4 mm at 16°C. Although frost roughness varied across the test surface, the frost k_s values in the center and rear regions tended to follow similar trends. This observed trend was consistent for all cases, which meant that the frost in the downstream region was nearly homogenous and formed a nearly uniform roughness. However, near the leading edge, the frost tended to generate a smooth frost layer with a small k_s value, which led to the uneven distribution of roughness along the length of the frost surface.

The unevenness of the frost surface was also affected by variations in environmental conditions, such as air temperature, air velocity, air humidity, and wall temperature. To estimate the non-uniformity in the frost roughness, the standard deviation of the frost equivalent sand-grain roughness heights at the front, center, and rear regions, Std_ k_s, was calculated. The Std_ k_s value represented the amount of variation of frost k_s at three different regions. A high standard deviation indicated the frost roughness heights were spread out over a wider range while a small value of standard deviation corresponded to a more even or smoother frost surface. The results are presented in the next section.

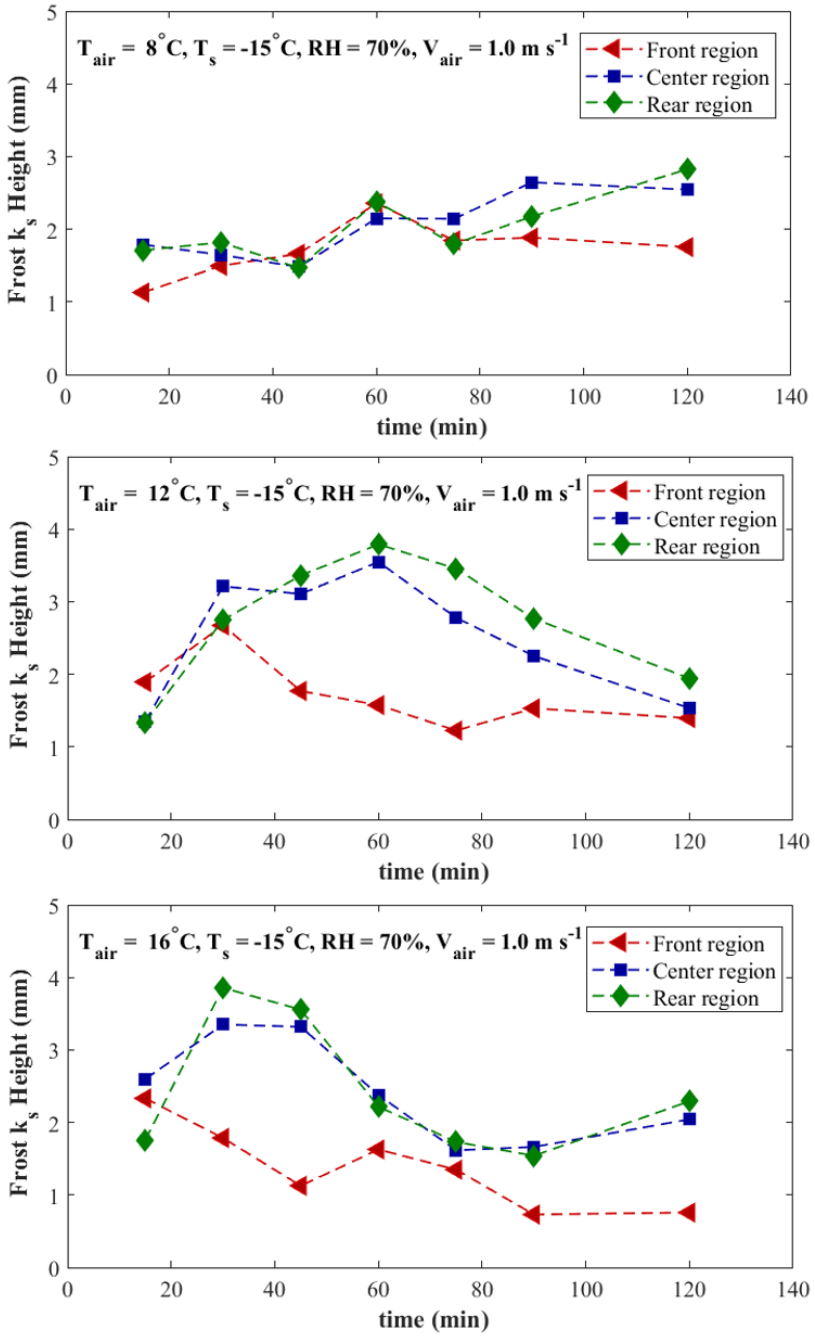

Figure 5.7. Frost k_s variations with time under different air temperatures.

Growth Behavior of Environmental Parameters on Frost Roughness Unevenness

The standard deviation of the frost equivalent sand-grain roughness (Std_ k_s) were computed in this section to evaluate the unevenness of the frost roughness. Figure 5.8 shows the results of the Std_ k_s values with time under different environmental

conditions. The Std_ k_s increased with time until reaching its maximum value, and then started decreasing. The timing for the appearance of the maximum frost Std_ k_s showed a strong relationship with environmental conditions. Within our testing ranges, the frost Std_ k_s reached its maximum value sooner when air temperature, relative humidity, or air velocity was increased, or wall temperature was decreased. To predict when the maximum frost Std_ k_s appeared, an empirical correlation with dimensionless parameters, were generated, as shown in Equation 5.4:

$$Fo_{std} = \frac{\alpha\, t}{D^2} = 0.019\ (w_a)^{-2.926}\ (Re_D)^{-0.607}\ (\frac{T_{air} - T_o}{T_o})^{1.127}\ (\frac{T_o - T_s}{T_o})^{-0.705} \quad (5.4)$$

where Fo_{std} is Fourier number to represent the dimensionless time when the frost Std_ k_s reached its maximum height, α is the thermal diffusivity of air, D is the hydraulic diameter, t is the real time when the frost Std_ k_s reaches its maximum height, w_a is the absolute air humidity, Re_D is the Reynolds number calculated by the hydraulic diameter of the test duct, and T_o is the triple point temperature. The R-square of this empirical correlation was 0.732. Figure 5.9 shows the comparison of the measured and correlated data of the dimensionless appearance time. The potential reasons limiting the accuracy of the correlation may be from two aspects: one was the small amount of data points (ten frosting cases), and the other was the large time step (15 min) for data collections. Although this correlation had some room for improvement, it appeared to be capture the growth behavior of the frost Std_ k_s.

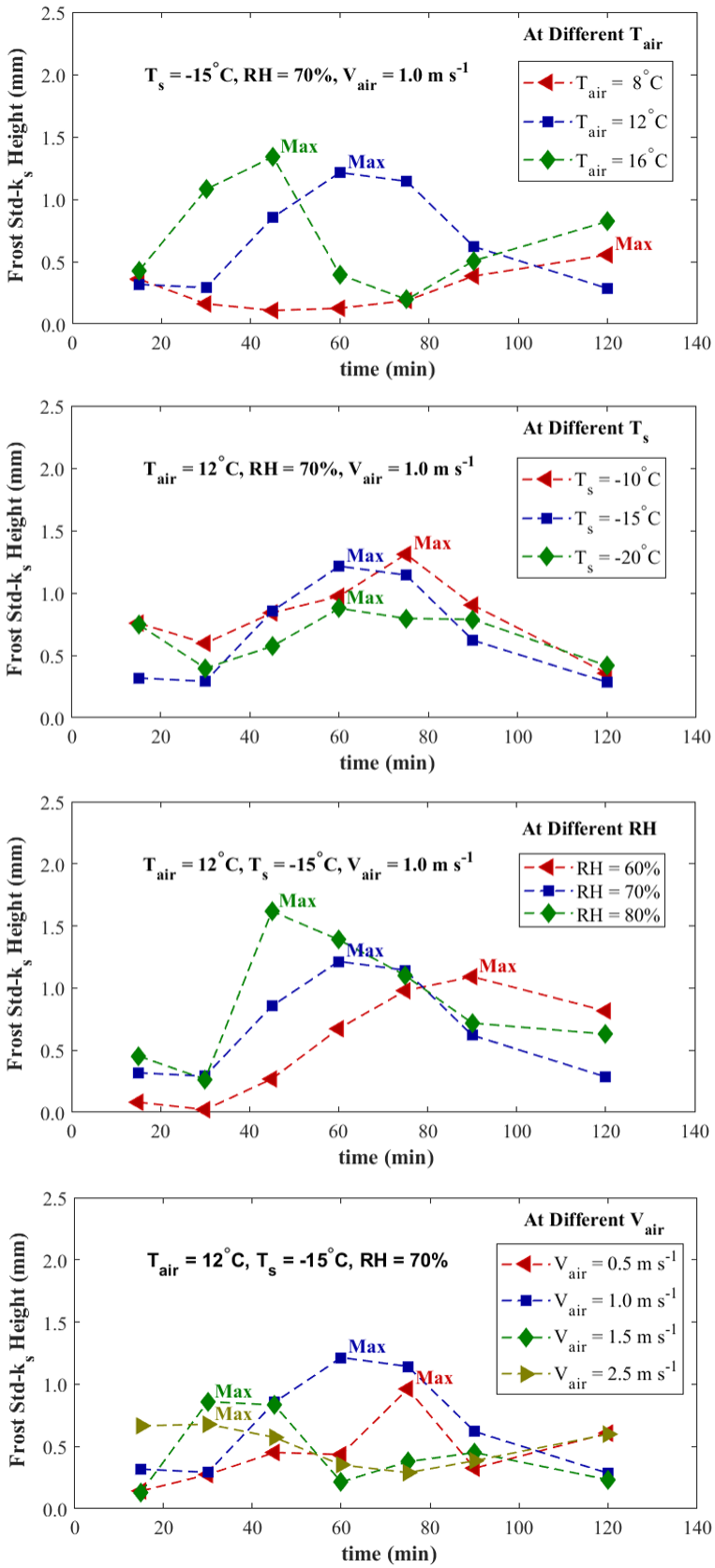

Figure 5.8. Frost Std_k_s values with time under different environmental conditions.

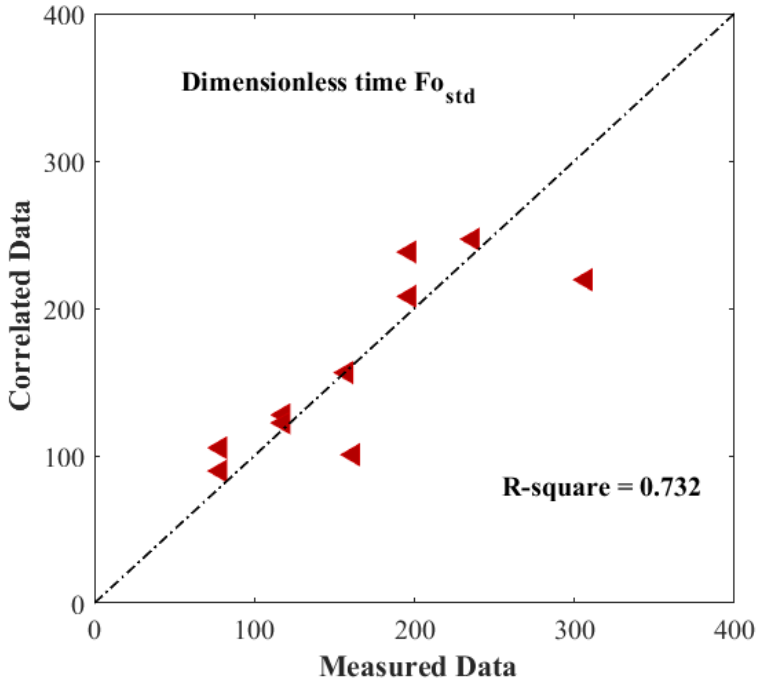

Figure 5.9. The measured and correlated data of the dimensionless appearance time of the maximum frost Std_ k_s height.

Figure 5.8 shows the importance of each environmental parameter on the growth of Std_ k_s heights. Changing air temperature or relative humidity led to considerable variations on the Std_ k_s while the effects of adjusting wall temperature or air velocity were limited. To quantitatively evaluate the importance of each parameter, an analysis of variance (ANOVA) test was performed on the resulting Std_ k_s values.

By varying the environmental conditions, ten cases were used to perform a one-way ANOVA test to identify the most important parameters determining the unevenness of the frost roughness. To remove the time parameter from the ANOVA analysis, the growth rates of Std_ k_s were analyzed for two times: 1) the 0 to 45 minute test span and 2) the 45 to 90 minute test span. The slopes of the regression lines through the resulting points in two time spans were evaluated as shown in Equation 5.5.

$$\dot{Std\_k_s} = \frac{dStd\_k_s}{dt} = \frac{N\sum t_j Std\_k_{s,j} - \sum t_j \sum Std\_k_{s,j}}{N\sum t_j^2 - \left(\sum t_j\right)^2} \tag{5.5}$$

The statistical variance of all the growth rates, for the Std_ k_s, was compared to the statistical variance of the growth rates from each subgroup with each of the four environmental parameters. Based on the comparison of the statistical variance of the group growth rates to the statistical variance of the entire set of growth rates, a probability, or P-value, can be evaluated to assess the importance of each parameter on the resulting Std_ k_s growth rates. This part of work was done by applying JMP software. The lower the P-value, the more important the variable was in determining the growth rate of roughness unevenness.

Table 5.3 lists the results of the ANOVA analysis for the Std_ k_s growth rates. The P-value for relative humidity and air temperature at both test spans were smaller than 0.1 or even 0.01, which indicated that relative humidity and air temperature were the most important factors governing the unevenness of frost roughness. Increasing air humidity or air temperature provided more water vapor for the growth of frost in the center and rear regions. As a result, frost with rougher surface were formed downstream the cold surface, which led to a large Std_ k_s values.

Table 5.3. P-value of the Std_ k_s growth rates

Parameter	P-value (0-45 min)	P-value (45-90 min)
V_{air}	0.37760	0.79541
T_s	0.97991	0.44209
RH	0.01233	0.00398
T_{air}	0.00683	0.02584

To further investigate the importance of each environmental variable on the frost k_s height at different locations (the front, center, and rear regions), ANOVA tests, similar with the one for Std_ k_s growth rates, were conducted. Table 5.4 listed all the P-values of frost k_s growth rates at different locations under two different time spans. For the formation of frost k_s in the front region, the P-value of air velocity had the smallest value for both time spans, which indicated air velocity had the most significant impact on frost k_s growth near the leading edge. Increasing air velocity should produce higher heat and mass transfer in the front region which can help melt the sharp peaks of frost crystals to form a smoother frost layer.

For the formation of frost k_s in the center and rear regions, air velocity was no longer the most critical factor. Instead, relative humidity and air temperature were dominated. In the downstream region, the growth of frost k_s was more dependent on the amount of water vapor as measured by the relative humidity. Higher relative humidity created frost crystals with larger sizes, which led to a rougher frost surface.

Table 5.4. P-value of frost k_s growth rates at different locations

	P-value (0-45 min) Front	P-value (45-90 min) Front	P-value (0-45 min) Center	P-value (45-90 min) Center	P-value (0-45 min) Rear	P-value (45-90 min) Rear
T_s	0.99554	0.89410	0.55738	0.76195	0.63832	0.91507
V_{air}	0.05192	0.22138	0.45137	0.66718	0.46636	0.59195
RH	0.80246	0.57291	0.25325	0.13035	0.08962	0.01993
T_{air}	0.35959	0.38186	0.24514	0.13256	0.10539	0.08385

Average Frost k_s Height

Because the frost far away from the leading edge grew in a way to form a nearly uniform roughness, an average value of the frost k_s heights in the center and rear regions were used to represent the general k_s value for the frost surface. Figure 5.10 lists the

results of average frost k_s (k_{ave}) values with time under various environmental conditions. The frost k_{ave} increased with time. Once it reached its maximum height, the frost k_{ave} value then started decreasing. Note that the maximum value of frost k_{ave} (k_{max}), as well as the timing it appeared, showed a strong dependence on environmental conditions. Within our testing ranges, the frost k_{ave} had a larger maximum value when air temperature, relative humidity, or wall temperature was higher, or air velocity was lower. On the other hand, the maximum height appeared earlier when air temperature, relative humidity, or air velocity was higher, or wall temperature was lower.

Equations 5.6 and 5.7 give the empirical correlations of the dimensionless appearance time of frost k_{max} and the value of the frost k_{max}, respectively. These two empirical correlations should be useful for describing the growth behavior of frost equivalent sand-grain roughness and further investigating the effects of frost roughness on aerodynamic performance of frosted surface. The correlation in Equation 5.6 had a 0.911 R-squared while that for Equation 5.7 was 0.634. The measured and correlated data of the dimensionless appearance time of frost k_{max} and the value of the frost k_{max} were compared and shown in Figure 5.11 and 5.12, respectively. The outlier in Figure 5.11 was the one and only one test with air velocity of 0.5 m/s. The predictive accuracy of Equation 5.6 was reduced in this case due to the lack of data obtained at the minimum tested air velocity (0.5 m/s) when generating the empirical correlation.

$$Fo_{ave} = 1.003\,(w_a)^{-1.084}\,(Re_D)^{-1.616}\,\left(\frac{T_{air}-T_o}{T_o}\right)^{-0.731}\left(\frac{T_o-T_s}{T_o}\right)^{-0.774} \quad (5.6)$$

$$k_{max} = 208.9\,(w_a)^{-0.253}\,(Re_D)^{-0.880}\,\left(\frac{T_{air}-T_o}{T_o}\right)^{-0.268}\left(\frac{T_o-T_s}{T_o}\right)^{-0.436} \quad (5.7)$$

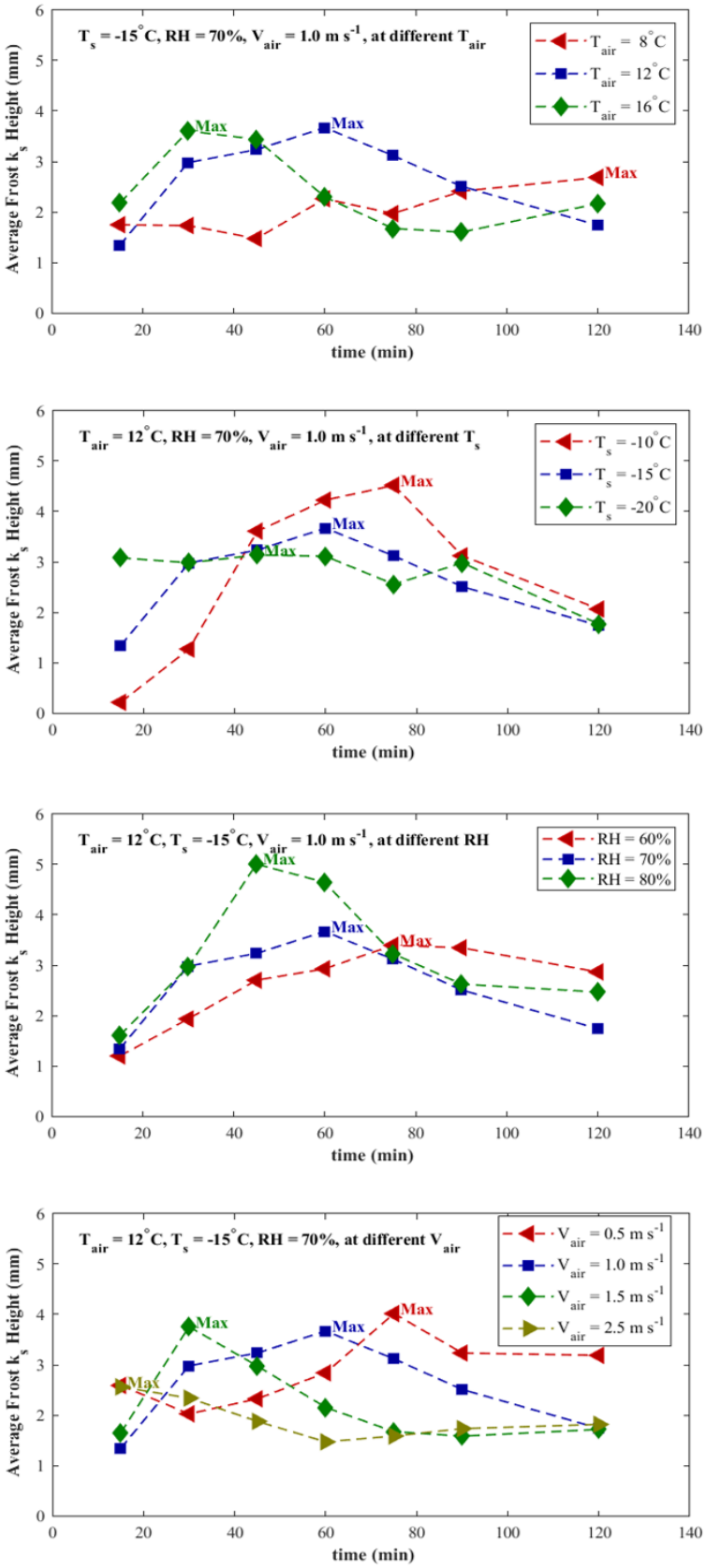

Figure 5.10. Average frost k_s values under various environmental conditions.

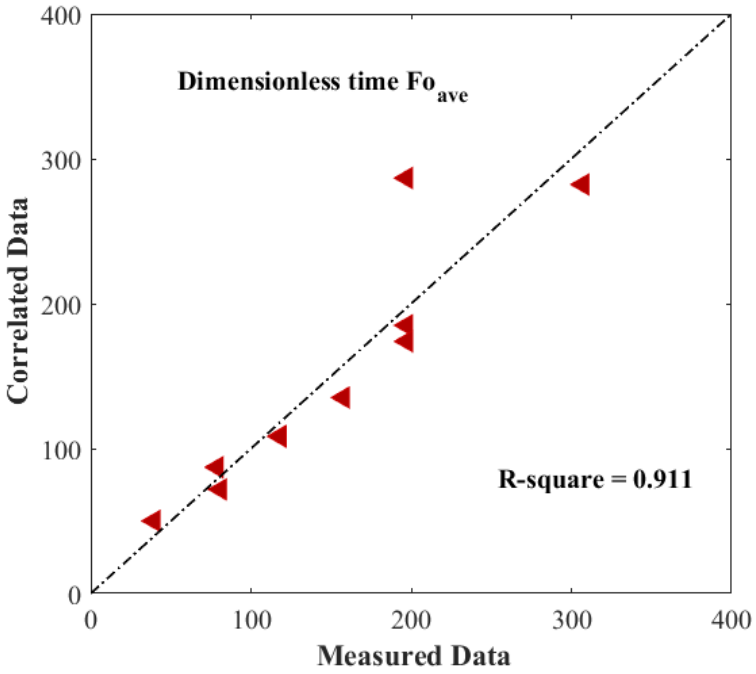

Figure 5.11. The measured and correlated data of the appearance dimensionless time of frost k_{max} height.

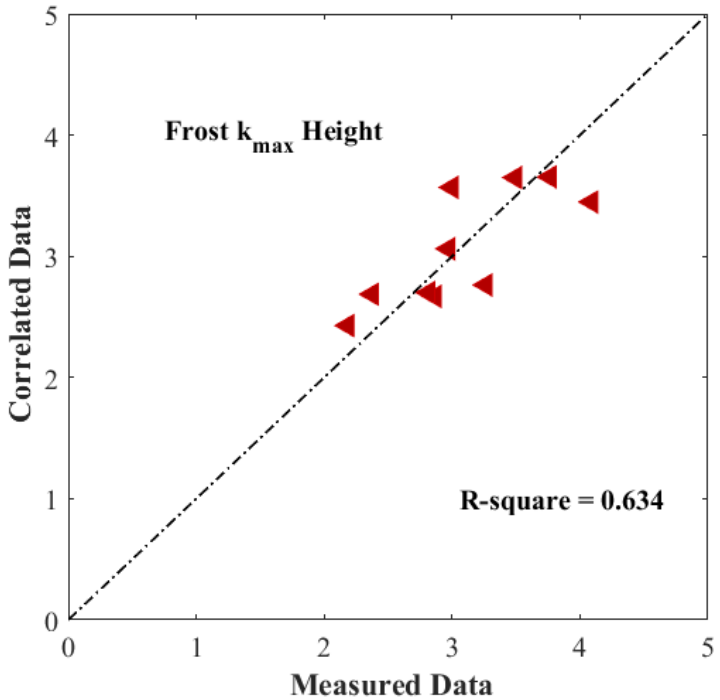

Figure 5.12. The measured and correlated data of the frost k_{max} height.

Conclusions

The variation of frost roughness across a flat plate was investigated by conducting frosting experiments under a range of environmental conditions covering air temperatures from 8 to 16°C, wall temperatures from -20 to -10°C, relative humidities from 60 to 80%, and air velocities from 0.5 to 2.5 m s^{-1}. The frost equivalent sand-grain roughness was measured by applying a 3-D photogrammetric method. The experimental results revealed that frost roughness was different from the front to the rear regions of the plate. The frost layer in the front region was smoother and had a smaller equivalent sand-grain roughness than the frost formed in the center and rear regions. The frost roughnesses in the center and rear regions of the cold plate were similar.

The standard deviation of the frost equivalent sand-grain roughness was used to represent the unevenness of frost roughness over the frost surface. The timing for the appearance of the largest frost roughness appeared sooner when the air temperature, relative humidity, or air velocity were higher, or the wall temperature was lower. An empirical correlation was developed to estimate the timing of the maximum frost roughness.

An ANOVA test was conducted on the data of the standard deviation of the frost equivalent sand-grain roughness over the frost surface. Results indicated that within our ranges of environmental conditions, relative humidity and air temperature were the most important factors determining the non-uniformity of frost roughness. Similar ANOVA tests were also conducted on the data of frost equivalent sand-grain roughness at different locations of frost surface. The results showed that within the ranges of environmental conditions in this task, air velocity was the dominating factor for the growth of frost

equivalent sand-grain roughness in the front region of the cold plate. However, relative humidity and air temperature took over the domination when frost formed in the center and rear regions.

During the two-hour duration of the experiments, the average frost equivalent sand-grain roughness over the frost surface generally increased with time until it reached its maximum height, and then started decreasing. The timing for the appearance of the largest average frost equivalent sand-grain roughness was shorter when air temperature, relative humidity, or air velocity was higher, or wall temperature was lower. The maximum frost equivalent sand-grain roughness became greater when air temperature, relative humidity, or wall temperature was higher, or air velocity was lower. Two empirical correlations were provided for the prediction of the maximum frost equivalent sand-grain roughness and its appearance time.

Acknowledgements

The work in this paper were supported as part of FAA Grant 17-G-011. Any opinions presented in this paper are those of the authors and do not reflect the any official position of the U.S. Federal Aviation Administration or the United States government.

CHAPTER SIX

Dimensionless Modeling of Frost Surface Roughness on a Cold Flat Plate under Forced Convection

Abstract

Laboratory experiments were conducted to generate empirical correlations for estimating surface roughness of frost formed on a cold flat plate under forced convection. Environmental parameters, including wall temperature (T_s), air velocity (V_{air}), relative humidity (RH), and air temperature (T_{air}), were considered when generating the correlations. The test conditions were chosen to simulate the environmental conditions experienced by cold-soaked fuel frost formation on upper airfoil surfaces. The root-mean-square height, skewness, and equivalent sand-grain roughness height of frost were correlated as functions of the Reynolds number, absolute humidity, and dimensionless temperature. The correlations can be used in the following ranges: wall temperatures from -20 to -5°C, free stream temperatures from 8 to 16°C, relative humidities from 60 to 91%, and air velocities from 0.5 to 2.5 m s^{-1}. The comparison between the correlation of frost equivalent sand-grain roughness height in this study and a previous model revealed the importance of geometry on frost roughness formation.

Key Words

Frost roughness, empirical correlation, flat plate, environmental conditions

Nomenclature

D	=	Hydraulic diameter
Fo	=	Fourier number
h_f	=	Frost thickness
k_s	=	Equivalent sand-grain roughness
N_p	=	The number of points in a surface point cloud
ROI	=	Region of interest
Re_D	=	Reynolds number calculated by hydraulic diameter
RH	=	Relative humidity
RMS	=	Root-mean-square
R_q	=	Root-mean-square roughness height
Skw	=	Skewness
T	=	Temperature
V	=	Air velocity
w	=	Absolute humidity
Z_i	=	Surface elevation at a point
$\bar{Z}$	=	The mean surface elevation, $= \frac{1}{N_P}\sum_{i=1}^{N_P} Z_i$

Superscript

*	=	Dimensionless

Subscripts

a	=	Air
s	=	Wall surface
fst	=	frost
o	=	Triple point

Introduction

Cold-soaked fuel frost contamination on aircraft wings is an undesirable phenomenon that may affect aircraft takeoff safety. The formation of cold-soaked fuel frost commonly occurs when an aircraft needs enough fuel for a round trip or multi-city trip. In these cases, the fuel in the aircraft wing tanks could easily reach temperatures below 0°C due to the plane cruising at altitudes at 10,000 meters or greater. Frost can rapidly grow on the upper airfoil surfaces near the cold-soaked fuel tanks after the aircraft lands downs at airports with relatively cool and moist air. The additional roughness due to frost on an aircraft's wing surface could cause an increase in the drag and affect the aerodynamic performance of the wing [2].

The dependence of frost growth under different atmospheric and surface conditions has been investigated extensively, specifically on flat plates. Researchers [3-14] indicated that air humidity, air velocity, wall temperature, and air temperature had primary impacts on the microstructure and properties of frost deposited on a cold surface. Generally, frost formation on a cold surface usually starts with condensation of water droplets and the subsequent freezing of these super-cooled droplets[17]. Initial frost crystals then emerge on the frozen condensate droplets. These crystals vary in shapes that correspond to the ambient cold wall temperature and air humidity [17-19]. As the frost crystals continue to grow and connect with each other, a porous frost layer eventually forms. The type of frost crystals on the top of the frost layer might change from feather-shaped to needle-shaped, then flake-shaped or even irregular-shaped during frost formation [76]. Additionally, the different shapes of frost crystals propagating from the frost surface can produce a range of frost roughness [76]. During the frost growth

process, moist air either deposits on the frost surface to increase the frost thickness or crosses the frost surface into the inner frost layer to thicken the frost density [20-25].

A number of frost growth predictive methods [25, 45-49] have been presented and reviewed in the literature, including empirical correlations obtained from experimental data, and mathematical models based on the analysis of the conservation of mass and energy in the frost layer. Most studies focused on frost properties, such as frost thickness and density. During modeling, many assumptions were needed to simplify the predictive models. Breque and Nemer [25] investigated the effects of different assumptions, and concluded that improving correlations for the convective heat and mass transfer coefficients was one approach to increasing the accuracy of frost growth models. The heat and mass transfer coefficients were not only dependent on frost thickness and frost density, but also frost surface morphology. Therefore, it was not acceptable to assume that the frost layer was a smooth wall. The information of frost surface roughness was essential. Furthermore, a predictive model of frost roughness is helpful not only for the study of heat and mass transfer on frost layers, but also for the investigation of aerodynamic performance of frosted surfaces.

Although researchers have investigated the modeling of frost formation for many years, few studies are related to the prediction of frost roughness. Chen and Rohsenow [1] provided a relationship between frost thickness and frost equivalent sand roughness (see in Figure 6.1). The authors obtained the frost roughness data via comparisons between frost images and sand grain sizes. According to their results, frost roughness was proportional to frost thickness in the initial growth stage, and gradually climbed to a plateau as the frost continued to grow.

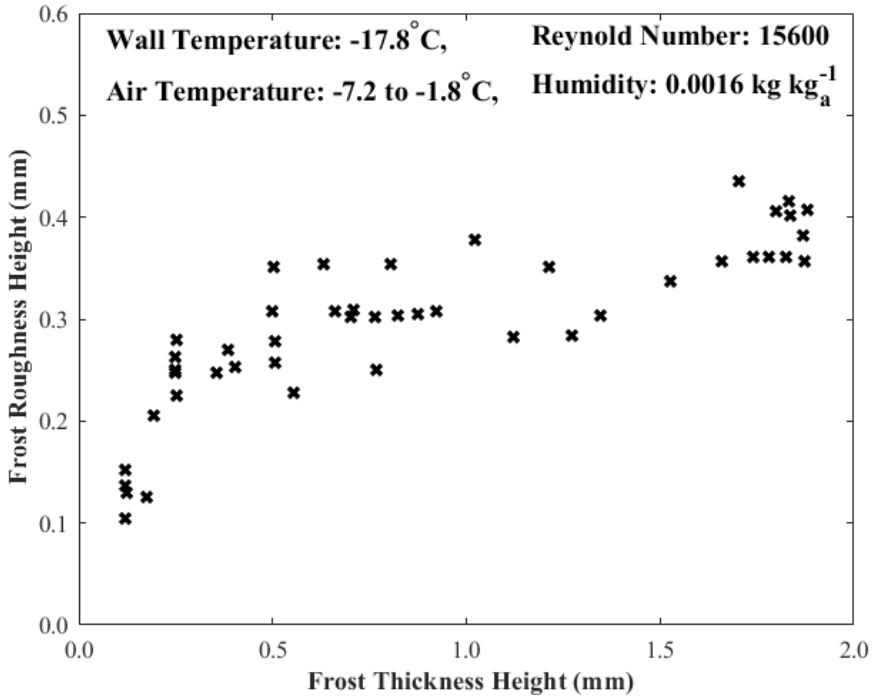

Figure 6.1. Relationship between frost roughness height and frost thickness height [1]

Yun et al. [31] developed a model that estimated frost roughness based on experiments on a flat plate (128 mm wide and 500 mm long) at subfreezing temperatures. In their study, frost roughness was defined as the height difference between frost peaks and valleys. It was measured under magnification using a micrometer with a thin needle to ensure the needle tip/frost contact. Figure 6.2 shows the results of frost roughness from their study. The authors indicated that column crystals grew almost normal to the frost surface so that a rougher frost was formed with these crystals. In contrast, plate type crystals made the frost layer denser and smoother than with column crystals. By calculating the average frost roughness under different test conditions, the authors developed an empirical correlation of frost roughness as a function of time:

$$y(t) = 3.92 * 10^{-3} + 0.069 \cdot t - 0.0023 \cdot t^2 + 2.84 * 10^{-5} \cdot t^3 - 1.28 * 10^{-7} \cdot t^4 \quad (6.1)$$

The correlation is shown in Figure 6.2. Frost roughness peaked at about 25 minutes, then decreased over time.

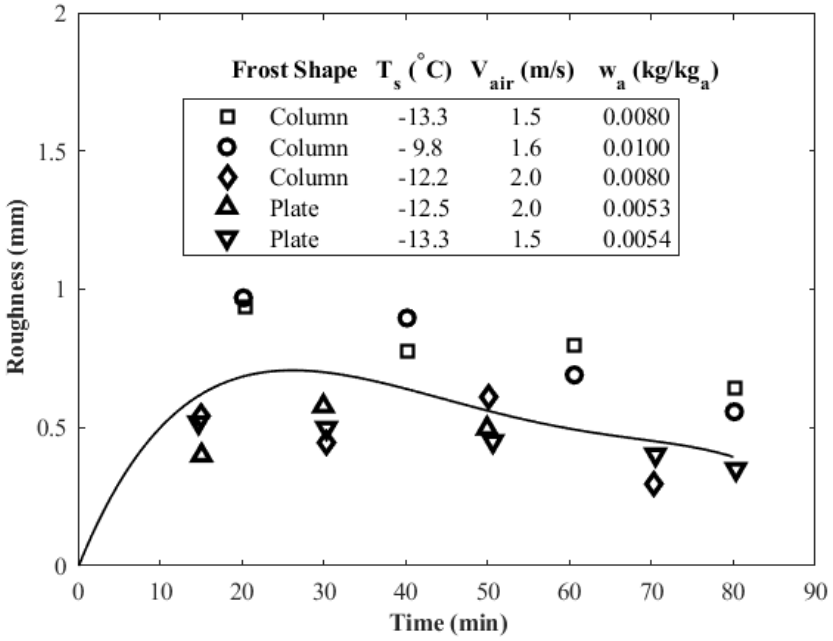

Figure 6.2. Time Variation of Frost Roughness at Constant Tair 26.85°C (300 K) [31].

Yun et al.'s frost roughness correlation had several limitations due to the small range of experimental conditions and its high standard deviation (±29%). The roughness data were based on one local measurement (250 mm away from the leading edge of the 500 mm-long flat plate), which limited the ability to obtain other information of frost surface roughness, such as root-mean-square (RMS) height and surface skewness. Furthermore, the correlation was given only as a function of time, but the frost roughness was known to be strongly influenced by locations on a surface and environmental conditions, such as air temperature, wall temperature, air velocity, and air humidity.

The overall objective of this paper was to develop empirical correlations of frost surface roughness by considering the following relevant environmental parameters: air temperature, air velocity, air humidity, and wall temperature. The correlations were

expressed as functions of the Fourier number, absolute humidity, Reynolds number, dimensionless temperatures.

Methodology

Experimental Setup

A closed-loop psychrometric wind tunnel was employed in this study. Figure 6.3 shows the schematic drawing of the wind tunnel. It was composed of four sections: the humidity control module with a humidifier and a dry gas injection system, the circulation module with an adjustable electronically commutated motor blower, an air temperature control module with two cooling coils and a duct heater, and a test section where the wall temperature was controlled and experimental data were collected.

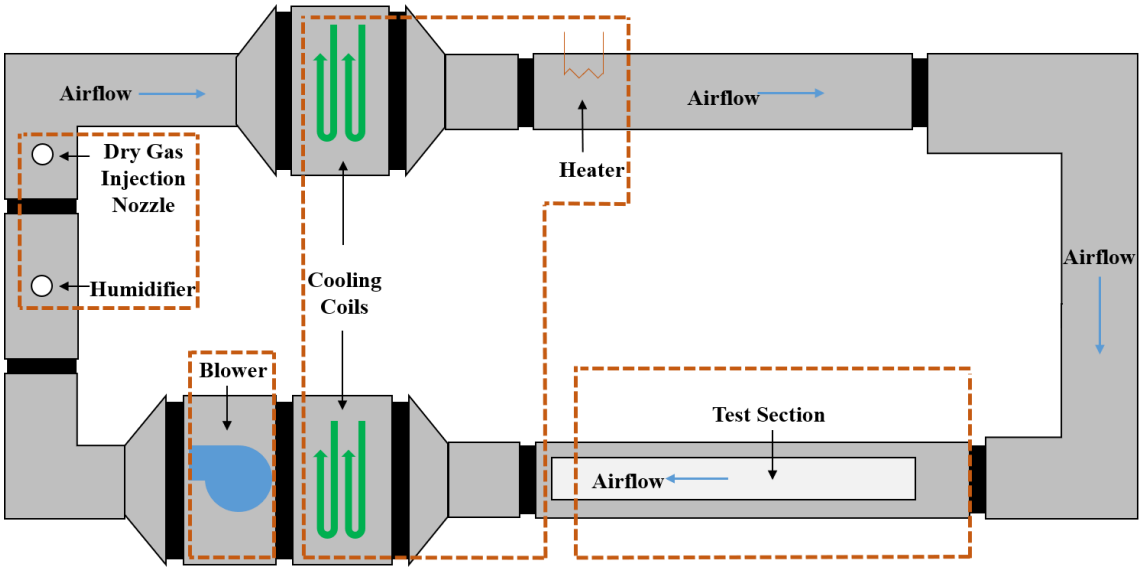

Figure 6.3. Schematic overview of the wind tunnel loop system.

Figure 6.4 provides a detailed schematic of the test section. It consisted of an optical transparent panel made of acrylic glass that allowed for in-situ, vertical and horizontal viewing in the microscopy system without disruption to frosting processes. A

Vaisala HMT-333 series relative humidity sensor and a type-T thermocouple, mounted upstream from the test surface, were used for the measurement of the air temperature and the relative humidity, respectively. A TSI 1750 constant temperature hot-wire anemometer (model 1201 sensor probe) was located downstream from the test surface for the measurement of the air velocity. A thermal stage mounted at the bottom of the test section was used to control the test surface temperature. The stage was composed of a type-T thermocouple, a thermoelectric cooler, and a copper heat sink. A 3 cm by 3 cm polished aluminum test surface was bonded with the thermal stage by a 0.254 mm-thick thermally conductive material. All the controls of the test conditions were done through a NI LabVIEW program.

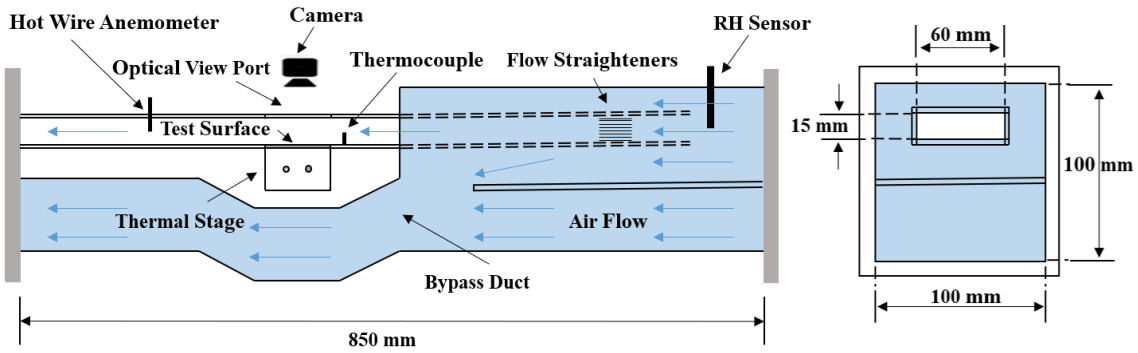

Figure 6.4. A detailed schematic of the test section.

Frost Thickness and Surface Temperature Measurement

To accomplish non-contact and in-situ frost thickness measurements, a Nikon D3400 DSLR camera with an AF Micro Nikkor 60mm f/2.8D lens was applied in this study. It was mounted at the lateral side of test surface to capture a 2D profile of frost surface. When the camera was set at a 1.0x reproduction ratio, the subject in the plane of focus was identical in size to the image sensor size, which was 23.5 mm by 15.6 mm.

This feature of the camera provided an approach for the measurement of frost thickness. Figure 6.5 gives an example of the frost thickness measurement. First, a reference image was captured before frost formed on the surface. This image was used to identify the initial point of frost growth. Subsequently, a series of frost images were taken as frost grew on the surface. These images had an average resolution of 255 pixels per mm. By applying ImageJ software to measure the pixel changes of the air-frost boundary line between the reference image and the new frosted surface images, quantitative increments of the frost heights were identified.

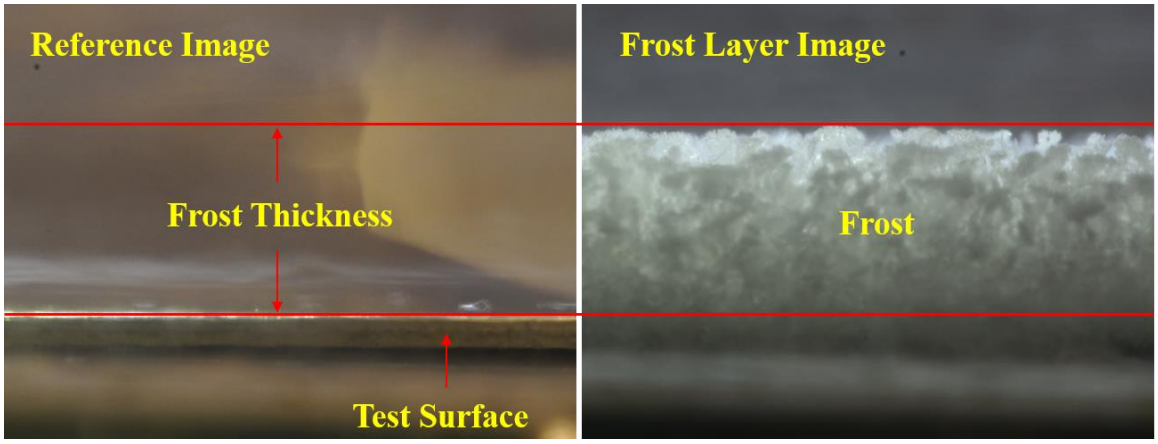

Figure 6.5. An example of frost thickness measurement.

During the measurement of frost thickness, a Digi-Sense traceable dual-laser infrared thermometer was employed to measure the frost surface temperature from the top of the test surface. The infrared thermometer was fixed on a customized acrylic glass cover with a small view window. During the measurement of frost surface temperature, the view window was moved to the top of frost surface, and then quickly slid back to completely seal the test section. The thermometer was set in the mode to record the minimum value during the measurement. The frost surface temperature measurement was finished in less than 2 seconds, which provided minimal impact on the frost growth.

Frost Roughness Measurement

The measurement of frost roughness was accomplished through a 3-D photogrammetric method developed by Miyauchi et al. [33]. The method was developed to fulfill the purpose of in-situ measuring of the frost roughness on a closed-loop psychrometric wind tunnel. This approach was non-intrusive and did not affect the frost surface, frost structure, or air/frost temperatures during testing.

The same Nikon camera used in the frost thickness measurement was applied here but mounted at the top side of the test surface. At the beginning of image data acquisition, the camera was traversed approximately 4.45 mm along the positive x-direction for 7 images, and then moved approximately 2.15 mm in the positive y-direction. After that, the previous step was repeated for another four sets of images. A total of 5 rows of 7 images were captured within 45 seconds for a set of image data.

Next, the data images went through a post processing using a photogrammetric software (Agisoft Photoscan Pro [77]) to estimate the frost surface topography. Figure 6.6 gives an example of (a) an image layout and (b) its frost surface model generated by Agisoft Photoscan Pro. A 60-degree sloped scale bar with specks of black spray paint was placed near the x-direction edge. The specks of black spray paint on the scale bar were used to create a reference for the x-y plane of the digital frost surface model in the software of Agisoft Photoscan Pro. On the other hand, the 60-degree slope of the scale bar was applied to scale units of the digital model in the vertical z-direction through a MATLAB program. The scaling magnitude was determined by comparing the physical slope of the scale bar to the computed slope of the scale bar in the digital model.

Eventually, a scaled frost surface topography file, containing a set of data points of the external frost surface with correct units in space, was obtained.

Based on previous observations, frost roughness downstream of the leading edge of the cold flat surface was homogenous. Thus, we selected a downstream area as the region of interest (ROI) for frost roughness measurement in this study, as shown in Figure 6.6(b).

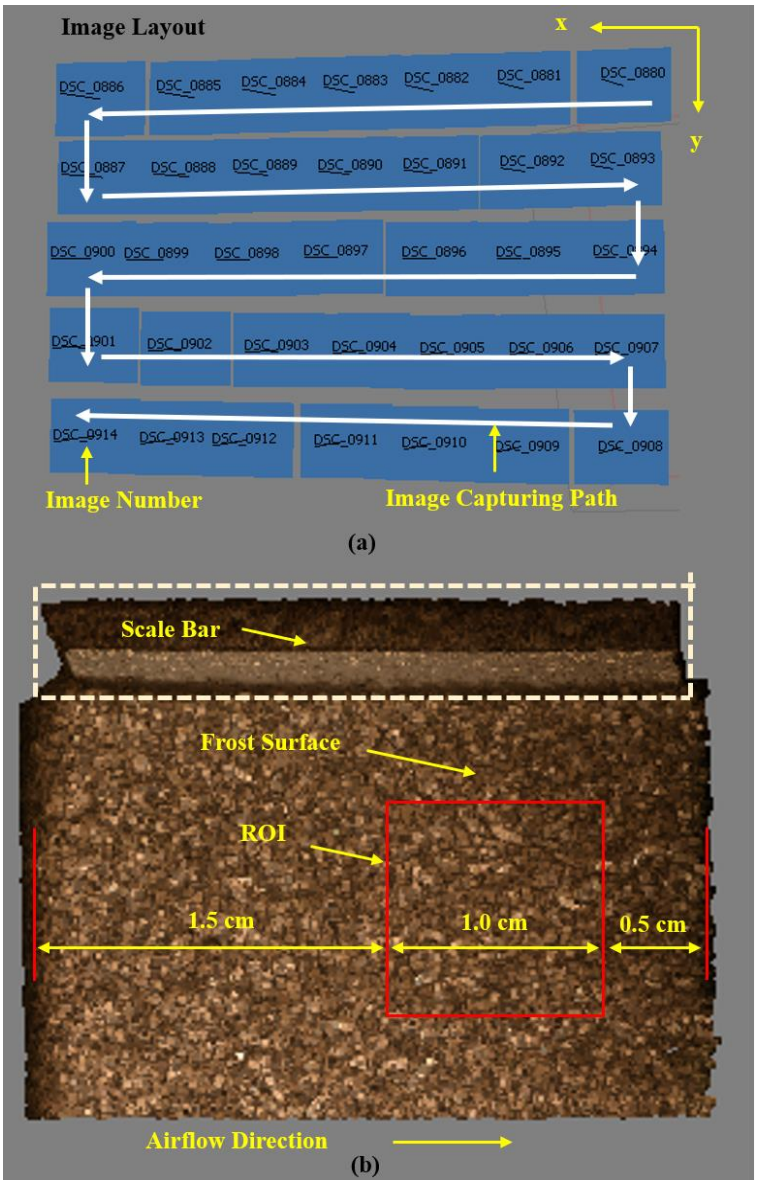

Figure 6.6. An Example of (a) an Image Layout and (b) its Frost Surface Model Generated by Agisoft Photoscan Pro.

From the scaled frost surface topography file, frost root-mean-square (RMS) height (R_q), frost surface skewness (Skw), and frost equivalent sand-grain roughness height (k_s) can be calculated. The RMS height (R_q) represented the standard deviation of frost height from the mean surface value and was calculated using Equation 6.2,

$$R_q = \left[\frac{1}{N_P}\sum_{i=1}^{N_P}(Z_i - \bar{Z})^2\right]^{\frac{1}{2}} \tag{6.2}$$

where N_p was the number of points in a dense point cloud file, Z_i was the surface elevation at a point, and $\bar{Z}$ was the mean surface elevation obtained by averaging the Z_i of all points. Next, the dimensionless parameter, surface skewness (Skw), as described in Equation 6.3, represented the symmetric distribution of the surface where a positive skewness indicated a frost surface had more frost peaks than valleys.

$$Skw = \frac{1}{{R_q}^3}\left[\frac{1}{N_P}\sum_{i=1}^{N_P}(Z_i - \bar{Z})^3\right] \tag{6.3}$$

Lastly, the calculation of equivalent sand-grain roughness height (k_s) was done by using an empirical formula (Equation 6.4) proposed by Flack and Schultz [73]. This correlation was built based solely on the surface statistics obtained from Equation 6.2 and 6.3.

$$k_s = 4.43R_q(1 + Skw)^{1.37} \tag{6.4}$$

A complete and detailed description of this 3-D photogrammetry can be found in Miyauchi et al. [33].

Test Procedures

The experiments were carried out with wall temperatures from -20 to -5°C, free stream temperatures from 8 to 16°C, relative humidity from 60 to 91%, and air velocities from 0.5 to 2.5 m s^{-1}. Table 6.1 gives the testing conditions of this study.

Table 6.1. List of experimental test conditions for the study of frost roughness modeling

T_s (˚C)	T_{air} (˚C)	RH (%)	V_{air} (m s^{-1})
-20	12	70	1.0
-15	12	70	1.0
-10	12	70	1.0
-15	16	70	1.0
-15	8	70	1.0
-15	12	60	1.0
-15	12	80	1.0
-15	12	70	0.5
-15	12	70	1.5
-15	12	70	2.5
-15	16	76	0.5
-10	16	76	0.5
-5	16	76	0.5
-10	12	76	0.5
-10	8	76	0.5
-10	16	61	0.5
-10	16	91	0.5
-10	16	76	1.0
-10	16	76	1.5

To prevent any water condensing on the aluminum surface, the thermoelectric cooler was kept in heating mode until the environmental conditions (air temperature, humidity, and velocity) reached the required setting. Once the target steady state condition was achieved, the thermoelectric cooler was then switched to the cooling mode. The desired wall surface temperature for a given test were typically reached in about 10 seconds. Each frosting test was run for two hours. Frost thickness and roughness images were captured every 15 minutes as well as the frost surface temperature. The images were

then post-processed to generate the final frost thickness and roughness. Table 6.2 lists the estimated measurements uncertainties.

Table 6.2. Accuracy of measurements for the study of frost roughness modeling

Variable	Uncertainty
Air Velocity	± 0.05 m s^{-1}
Air and Wall Temperature	± 0.5°C
Relative Humidity	± 2%
Frost Surface Temperature	± 0.83°C
Frost Roughness	± 7%
Frost Thickness	± 0.1 mm

Results and Discussion

Frost Roughness Growth Behavior

Frost roughness variables, including frost RMS height, frost surface skewness, and frost equivalent sand-grain roughness (k_s) height, were evaluated from the images. Through analyzing the 19 sets of frost roughness data, two typical growth patterns of frost roughness were observed. Figure 6.7 shows examples of both frost growth patterns. The left side y-axis is the frost height while the right side y-axis is the dimensionless value of frost skewness. The frost RMS height, frost k_s height, and frost skewness were shown as solid lines with triangle symbols, solid lines with square symbols, and dash lines with diamond symbols, respectively. Because the frost RMS height represented the standard deviation of frost surface height, it had a value less than 0.5 mm. For a two-hour test, the frost RMS height could continue to increase and reach its largest value (0.47 mm) as shown in Figure 6.7(a). It could also grow at the beginning, reach a peak value, then begin decreasing after it reached its maximum value at 60 min for the case in Figure 6.7(b). Similarly, the frost k_s height of the case in Figure 6.7(a) kept increasing

and reached its maximum value 3.07 mm at the end of the two-hour test. For the case in Figure 6.7(b), the frost k_s height achieved its peak of 2.68 mm at 60 min which was the same time when the frost RMS height reached its maximum value. For these cases, the frost k_s height had similar growth trends but different amplitudes than the frost RMS height.

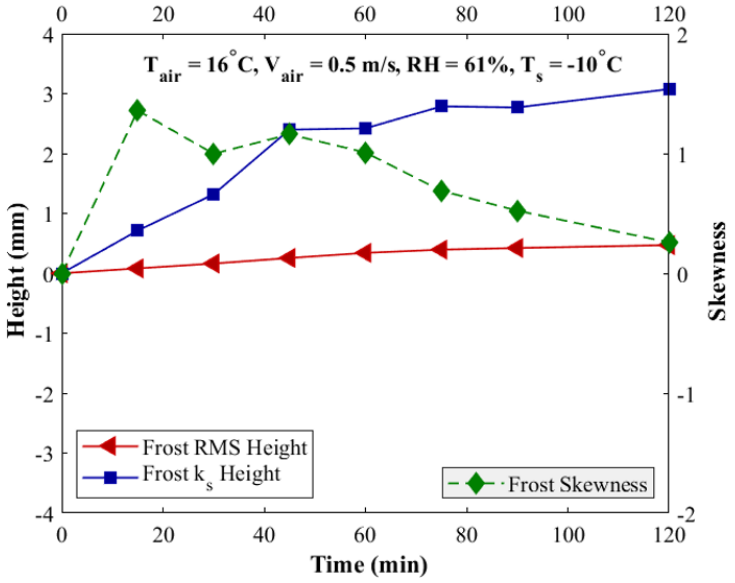

(a)

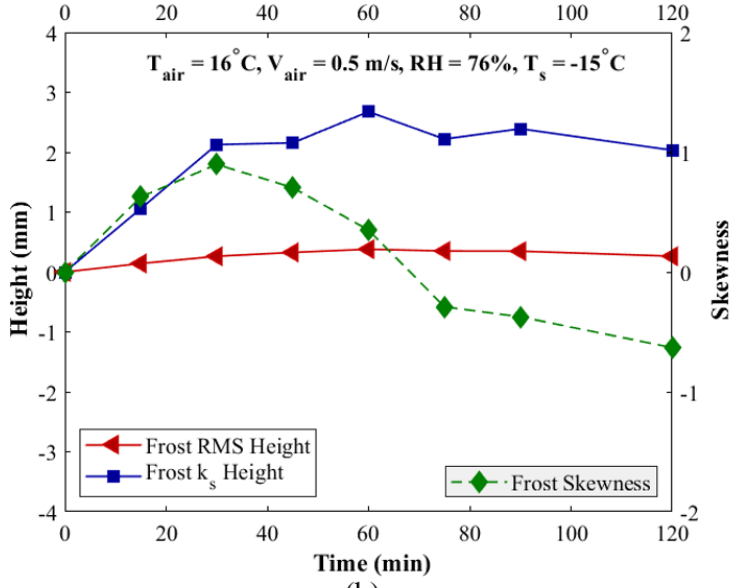

(b)

Figure 6.7. Three typical patterns of frost roughness formation.

Frost skewness, however, showed a different trend in contrast to the other two roughness parameters. For both cases in Figure 6.7(a) and 6.7(b), the growth of frost skewness values took a shorter time to pass over their peak points compared to the frost RMS heights. For the case in Figure 6.7(a), the frost skewness passed its maximum value of 1.36 at 15 min while in Figure 6.7(b), the peak frost skewness value was 0.90 at 30 min. In addition, the frost skewness was nearing zero when the frost RMS height turned to a low growth rate or even started to decrease. Thus, as the frost continued to grow, the previously formed peaks of frost crystals grew smaller or disappeared, which led to a symmetrically distributed frost surface as well as a small variation in frost heights.

Predictive Model of Frost Thickness and Frost Surface Temperature

Over 130 data points were used for generating these empirical correlations. Before developing the predictive models of frost roughness, the correlations of frost surface temperature and thickness were generated first. These two parameters were employed as independent variables in the modeling of frost roughness. The environmental properties were expressed as functions of dimensionless parameters, including Fourier number (Fo), Reynolds number (Re_D), absolute humidity (w_a), and dimensionless temperatures (T^*). Equation 6.5 and 6.6 gives the dimensionless wall temperature and the dimensionless air temperature, respectively.

$$T_s^* = \frac{T_o - T_s}{T_o} \tag{6.5}$$

$$T_{air}^* = \frac{T_{air} - T_o}{T_o} \tag{6.6}$$

The correlation of frost thickness is shown in Equation 6.7 with a R-square value of 0.94.

$$h_f = 1.759\ (Fo)^{0.445}\ (w_a)^{0.221}\ (Re_D)^{0.092}\ (T_s^*)^{0.653}\ (T_{air}^*)^{-0.174} \qquad (6.7)$$

The dimensionless temperature of frost surface is defined by the ratio of the difference between the triple point temperature of water and the frost surface temperature to the difference between the air temperature and the triple point temperature of water, and its correlation is presented in Equation 6.8 with a R-square value of 0.950.

$$T_{fst}^* = \frac{T_{air} - T_o}{T_{air} - T_{fst}} = 0.770\ (Fo)^{0.087}\ (w_a)^{0.226}\ (Re_D)^{0.104}\ (T_s^*)^{-0.273}\ (T_{air}^*)^{0.390} \qquad (6.8)$$

In Figure 6.8 and 6.9, the results of the dimensionless thickness and surface temperature of frost, calculated from Equation 6.7 and 6.8, respectively, are compared with experimental data.

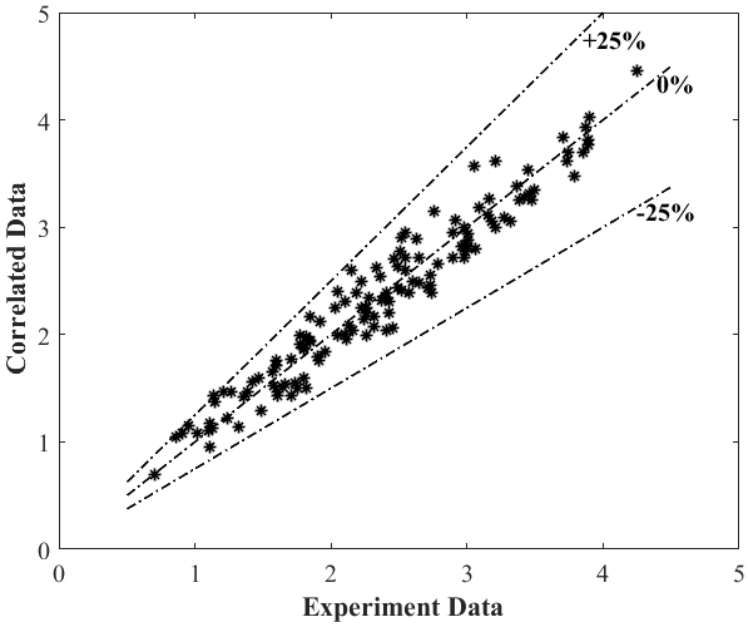

Figure 6.8. Comparison of the measured and correlated data of the frost thickness.

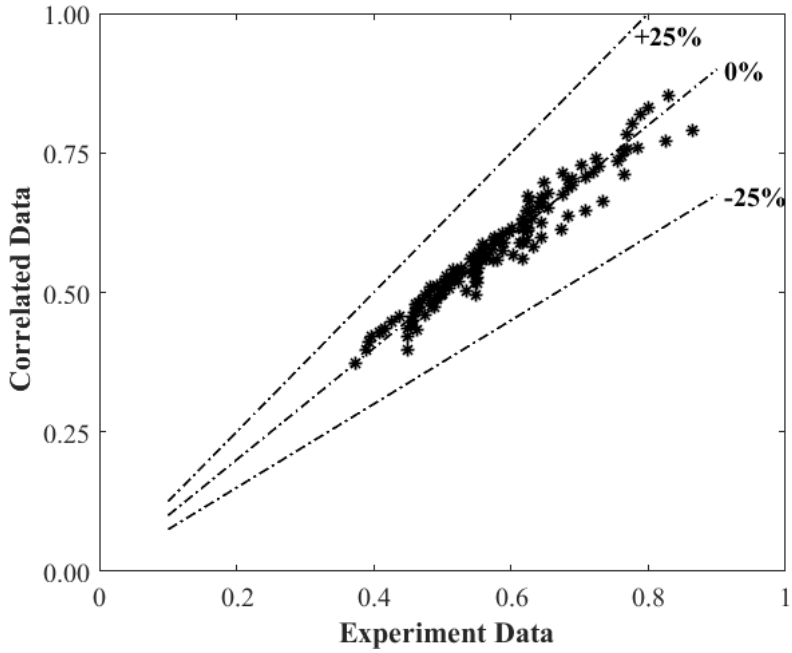

Figure 6.9. Comparison of the measured and correlated data of the dimensionless frost surface temperature.

Model of Frost Roughness Height

Models of frost roughness have rarely been documented in the literature. Chen and Rohsenow [1] developed a relationship between frost equivalent sand-roughness height and frost thickness height. But their research focused on frost surface roughness inside frosted tubes, which had a different geometry than the cold flat plate in this study. Yun et al. [31] provided an empirical roughness correlation of frost formed on a flat plate. But their roughness parameter was defined as the height difference between the frost peak and valley. Furthermore, their correlation was only a function of time. No environmental parameters involved. Their frost roughness was the average value over various environmental conditions.

In this study, frost roughness strongly depended on the variation of frost surface temperature (T_{fst}). Under the domain of frost surface temperature, the growth trends of frost roughness were clearer and more apparent. An example is given in Figure 6.10. The

data in this figure included all the frost k_s heights for the wall temperature cases of -15°C under frost surface temperature domain and time domain. During frosting tests, the frost k_s heights kept growing until the frost surface temperature reached a critical temperature zone, then started decreasing. In the time domain, however, identifying the trends of frost roughness formation is difficult, as illustrated in Figure 6.9. Therefore, the frost surface temperature was involved in the expressions of the dimensionless roughness correlation of frost instead of time in this study.

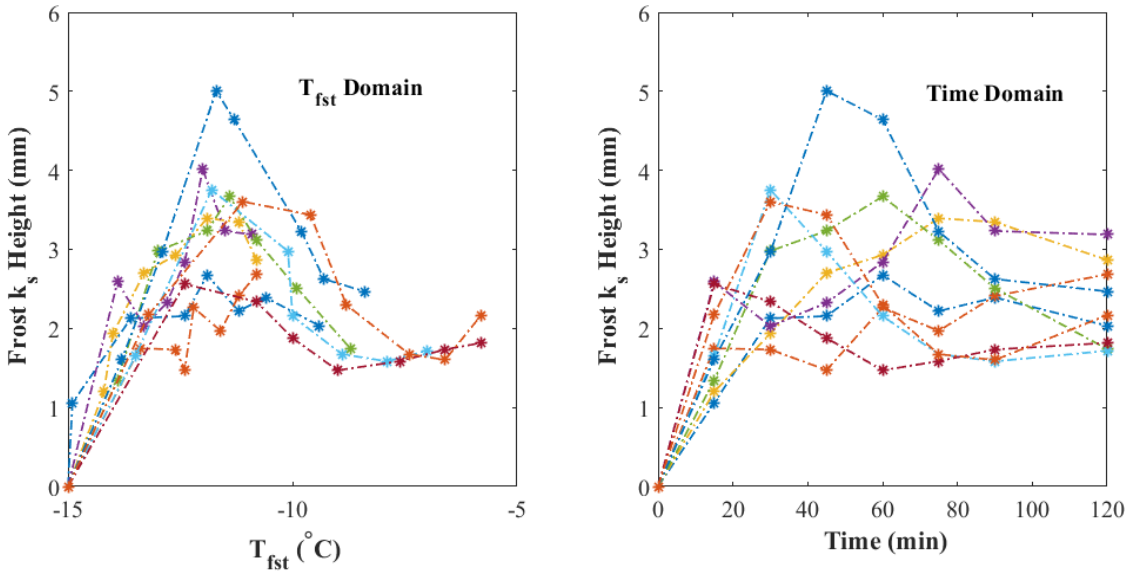

Figure 6.10. Frost k_s heights in the wall temperature cases of -15°C under T_{fst} domain and time domain.

The dimensionless RMS height of frost was expressed by using the frost RMS height divided by frost thickness, and its correlation is given in Equation 6.9. It had a R-square value of 0.570. Although this correlation may have some limitations, it does describe the growth of the frost RMS height under a range of environmental conditions. An example is given in Figure 6.11.

$$R_q^* = \frac{R_q}{h_f} = 2.123\,(w_a)^{-0.023}\,(Re_D)^{0.065}\,(\frac{T_{air}-T_o}{T_o})^{0.790}\left(\frac{T_o-T_s}{T_o-T_{fst}}\right)^{-1.227}\left(\frac{T_{fst}-T_s}{T_o-T_s}\right)^{0.342} \quad (6.9)$$

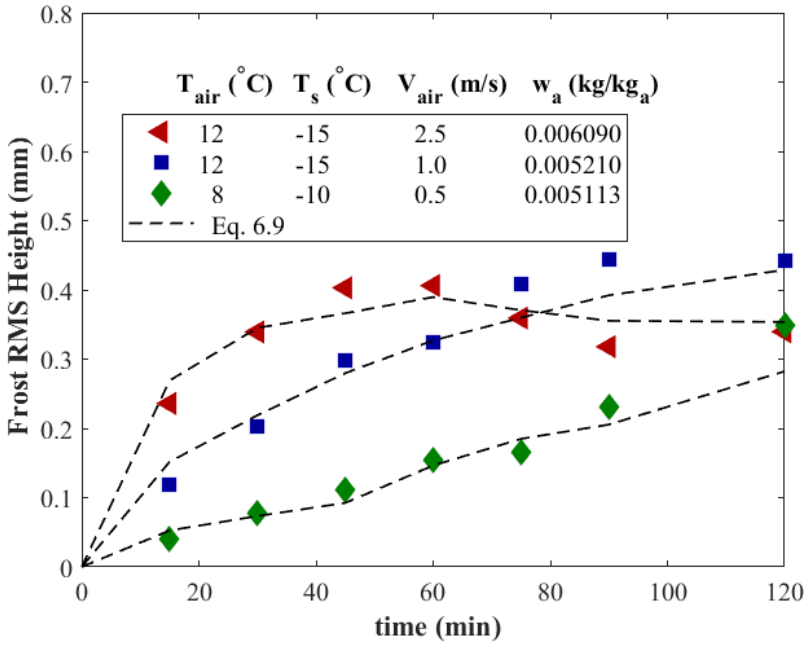

Figure 6.11. An example of frost RMS height variation under different testing conditions.

The dimensionless skewness of frost is defined in terms of the exponential of frost skewness, and its correlation is given in Equation 6.10. If the right-hand-side term of Equation 6.10 comes out to be greater than one, frost skewness has a positive value. On the contrary, frost skewness is negative if the right-hand-side term of Equation 6.10 is between zero and one. The R-square value for Equation 6.10 is 0.65.

$$\exp(Skw) = 13.182\,(w_a)^{0.524}\,(Re_D)^{0.064}\left(\frac{T_{air}-T_o}{T_o}\right)^{-0.524}\left(\ln\left(\frac{T_o-T_s}{T_o-T_{fst}}\right)\right)^{-0.324}\left(\frac{T_o-T_{fst}}{T_o}\right)^{0.612} \quad (6.10)$$

The dimensionless equivalent sand-grain roughness of frost is expressed by the ratio of frost equivalent sand-grain roughness height to frost thickness height, and its correlation is presented in Equation 6.11. The frost surface temperature is taken as an

exponential term, because the dimensionless equivalent sand-grain roughness strongly depends on it. The R-square value of Equation 6.11 is 0.53.

$$k_s^* = \frac{k_s}{h_f} = 0.029\,(w_a)^{0.367}(Re_D)^{0.150}\left(\frac{T_{fst}-T_s}{T_o}\right)^{0.342}\left(\exp\left(\frac{T_{air}-T_{fst}}{T_{air}-T_s}\right)\right)^{6.716} \quad (6.11)$$

In Figure 6.12, 6.13 and 6.14, the results of the dimensionless RMS height, skewness, and equivalent sand-grain roughness height of frost, calculated from Equation 6.9, 6.10 and 6.11, respectively, are compared with experimental data. Most of the data compare within ±25%. In Figure 6.13, it can be noticed that the predictive accuracy of the empirical correlation 6.10 reduced for the cases with relatively large skewness data due to lack of sufficient data points with high skewness when generating the correlation. The outlier that appeared in the most right-side of Figure 6.13 is the only point with frost skewness greater than 2, reaching 2.43.

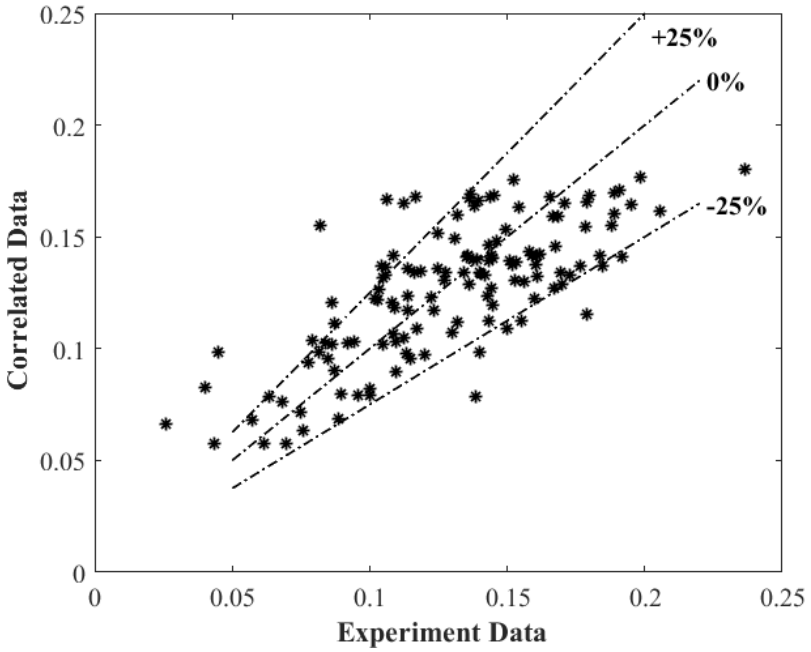

Figure 6.12. Comparison of the measured and correlated data of the dimensionless frost RMS height.

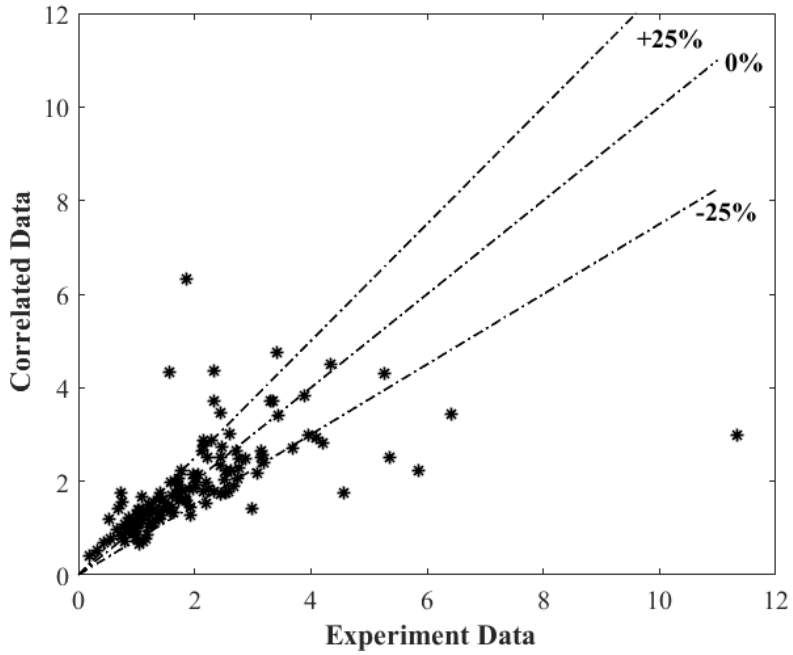

Figure 6.13. Comparison of the measured and correlated data of the frost skewness.

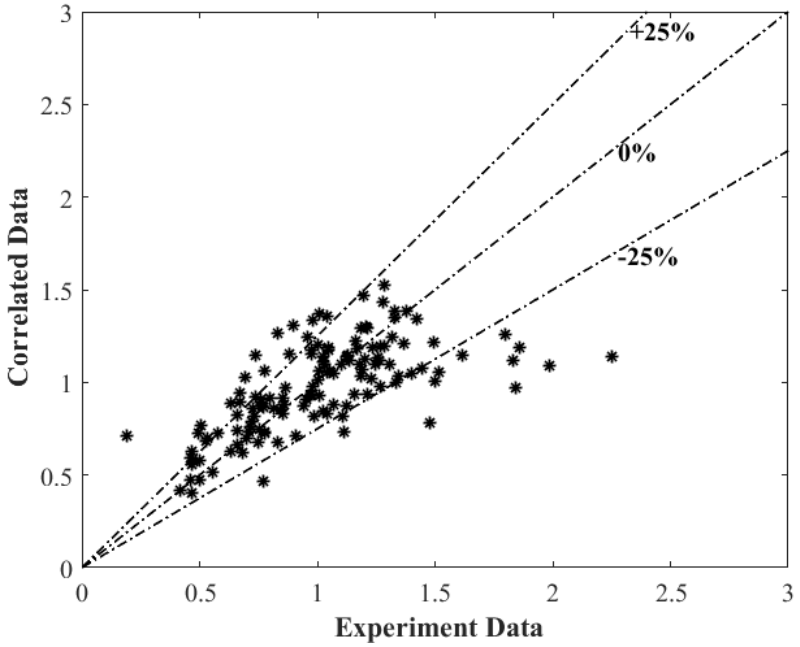

Figure 6.14. Comparison of the measured and correlated data of the dimensionless frost equivalent sand-grain roughness.

The results of Chen and Rohsenow's correlation [1] (Equation 6.12) and our predictive model (Equation 6.11) for the equivalent sand-grain roughness height are

compared with experimental data in Figure 6.15. The correlation of Chen and Rohsenow [1] was generated based on roughness data of frost formed inside frosted pipes as opposed to on a flat plate in this study. The k_{max} in Equation 6.12 was the steady-state value of frost roughness, defined as the final plateau of frost roughness growth. Here we used the maximum equivalent sand-grain roughness height to represent the steady-state value in Equation 6.12.

$$\frac{k_s}{k_{max}} = 1 - \exp\left(-\frac{h_f}{k_{max}}\right) \tag{6.12}$$

It should be noted that the correlation of Chen and Rohsenow [1] generally underpredicted the experiment frost k_s heights compared to that of Equation 6.11. One potential reason may be the difference between the geometries of the testing surfaces. Using a roughness correlation of frost formed inside frosted pipes may not be adequate to predict surface roughness of frost propagated on a flat plate. Geometry must be considered when predicting the formation of frost roughness.

Additionally, the tests for developing Equation 6.12 were controlled with constant volumetric flow rate inside that tube system. As frost grew, the actual diameter of the tube decreased, resulting in an increase in air velocity due to the constant airflow rate. The effect of the changing air velocity in developing Equation 6.12 may limit the application of Equation 6.12 on predicting frost roughness on flat surfaces when the air velocity is constant.

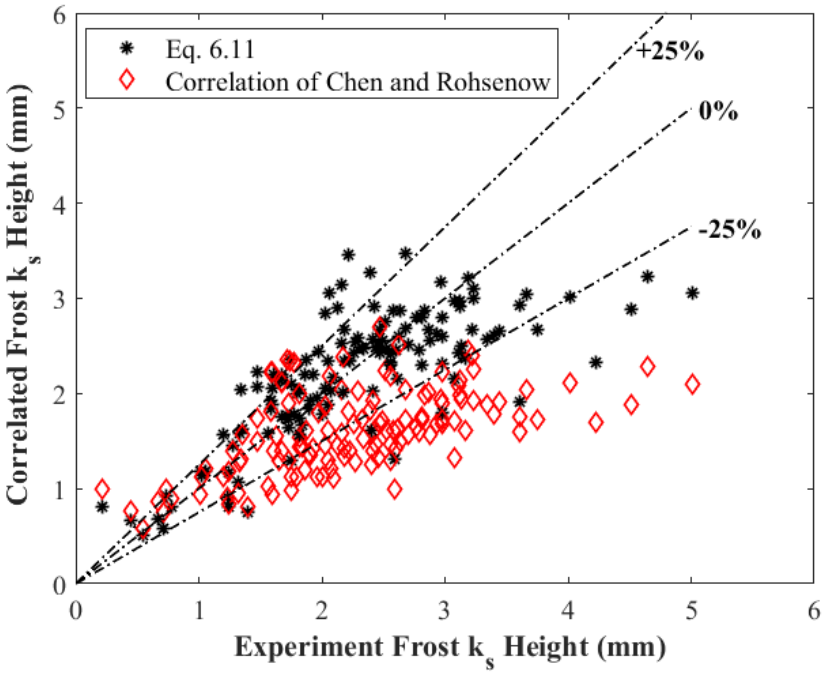

Figure 6.15. Comparison of the predicted frost equivalent sand-grain roughness from Equation 6.11 and Equation 6.12.

Conclusions

Frosting experiments were conducted to establish the empirical correlations of frost roughness properties, including frost RMS height, frost surface skewness, and frost equivalent sand-grain roughness height, as well as frost thickness and frost surface temperature. Environmental conditions were involved when generating these dimensionless correlations. The test conditions were chosen to simulate the environmental conditions experienced by cold-soaked fuel frost formation on upper airfoil surfaces. The empirical correlation of frost equivalent sand-grain roughness was compared to the previous predictive model, whose results revealed the importance of geometry on frost roughness formation. The suggested empirical correlations are valid under the wall temperature from -20 to -5°C, air temperature from 16 to 8°C, relative humidity from 61 to 91%, and air speed from 0.5 to 2.5 m s^{-1}.

Acknowledgements

The work in this paper was supported as part of FAA Grant 17-G-011. Any opinions presented in this paper are those of the authors and do not reflect any official position of the U.S. Federal Aviation Administration or the United States government.

CHAPTER SEVEN

Conclusions and Recommendations

The primary objective of this investigation was to characterize the roughness of frost as it formed on a cold flat plate under forced convection. To better understand the underlying phenomena responsible for the complex evolution of frost roughness, a series of visualization experiments were conducted over a wide range of carefully controlled environmental conditions in a closed-loop psychrometric wind tunnel. The study was divided into four subtasks: 1) Characterize the microstructure of the initial frost growth, 2) Identify the growth mechanics affecting frost roughness, 3) Quantify the uniformity of frost roughness over a cold flat plate, and 4) Develop a predictive model that estimates the roughness of frost as it grows on a cold surface.

In Subtask 1, the formation of different frost crystal types during the initial period of frosting was evaluated using a microscopy system to provide a better understanding of the structure of the growing frost. Frost crystals varied in crystal type, crystal size, and distance between crystals for range of environmental conditions in this study. Based on experimental observations, the initial frost crystals were classified into six types: feather crystals, sector crystals, sheath crystals, pole crystals, scroll crystals, and flake crystals. Wall temperature and air humidity were determined to be the main environmental factors affecting the formation of the initial crystal types. Frost crystal formation maps were developed in this study that varied by air temperature. The region covered by flake crystals formed under a wall temperature of -5°C in the case of an air temperature of

22°C was replaced by scroll crystals in the cases of air temperatures of 12 and 6°C. The relative humidity boundary line between the formation of feather crystals and sector crystals varied from 25 to 55% as the air temperature decreased from 22 to 6°C. Air velocity appeared to have no impact on the type of initial frost crystal in the velocity range studied here.

Increasing the wall temperature and air velocity led to a decrease in initial frost crystal size and distance. The largest frost crystal distance was measured as 0.72 mm under wall temperature -25°C and air velocity 0.5 m/s while the frost crystal distance under wall temperature -5°C and air velocity 5.0 m/s was less than 0.05 mm. Once the air velocity reached a critical level higher than 1.0 m/s, however, its influence on reducing the size and distance of initial frost crystals was limited. Increasing relative humidity had a small impact on the initial frost crystal distance but resulted in an increase in the crystal size when the frost initially formed on the cold surface. An empirical correlation of initial frost crystal distance was developed as a function of environmental parameters with a R-square value of 0.86.

The characterization of the frost crystal structure gained from Subtask 1 were used to identify the mechanisms affecting frost roughness in Subtask 2. Generally, the frost crystal type, frost crystal size, and frost crystal distribution on top of the frost layer impacted frost surface roughness. The frost crystal type might change from feather-shaped to needle-shaped, then flake-shaped or even irregular-shaped as the frost grew over time. Increasing air velocity from 0.5 to 1.5 m/s and air temperature from 6 to 16°C accelerated the change of frost crystal type from feather-shaped to irregular-shaped and produced frost crystals that appeared closer to each other. Increasing relative humidity

from 50 to 75% greatly enlarged the frost crystal size, but only slightly changed the frost crystal type during the same time scale. Increasing wall temperature from -25 to -15°C led to the initial frost crystal type changing from feather to needle crystal, which continuously influenced the ongoing process of frost formation. Eventually, feather and needle crystals with column growth pattern and large crystal size tended to create a thick and porous frost layer with a rough frost surface. On the other hand, flake and irregular crystals with plate growth patterns and small crystal size were likely to form a thin and dense frost layer with a smooth frost surface.

Due to the variation of frost crystal formation on top of the frost layer, the frost surface roughness presented diverse trends. Both frost root-mean-square height and surface skewness continuously increased initially and gradually reached maximum values. After passing through the peak values, the frost roughness started decreasing. Qualitatively, the time when the peak frost root-mean-square height appeared decreased when air velocity, air temperature, and wall temperature increased. The peak of frost root-mean-square height increased when air velocity, air temperature, and wall temperature decreased, and relative humidity increased. The frost skewness peak was enlarged when air velocity and air temperature decreased, or wall temperature and relative humidity increased.

The formation of frost surface roughness was not uniform along the cold test surface. Subtask 3 was conducted to study the variation of frost roughness over both time and locations on a flat plate under a range of environmental conditions. The experimental results showed that the frost layer in the front region of the frost surface was smoother and had a smaller equivalent sand-grain roughness than that formed in the center and rear

regions. The standard deviation of the frost equivalent sand-grain roughness was used to represent the unevenness of frost roughness over the frost surface. The time for the appearance of the frost roughness unevenness peak decreased if air temperature, relative humidity, and air velocity increased, or wall temperature decreased. A dimensionless correlation was developed to predict the appearance moment of the maximum frost roughness unevenness with a R-square value of 0.73. Moreover, an ANOVA statistical experiment was conducted on the data of the standard deviation of the frost equivalent sand-grain roughness. The results of the p-values from the ANOVA tests indicated that relative humidity and air temperature, with p-values less than 0.05, were the most important factors governing the formation of frost roughness unevenness in our study. Similar ANOVA tests were also conducted on the data of frost equivalent sand-grain roughness at the front, center, and rear regions of frost surface. The test results showed that air velocity with p-values less than 0.23 in this subtask was the dominating factor for the growth of frost equivalent sand-grain roughness in the front region of the cold plate. However, relative humidity and air temperature with p-values less than 0.26 were the key parameters for frost formed in the center and rear regions.

The experimental data also revealed that the frost formed in the downstream region was approximately homogenous and produced a nearly uniform roughness. Therefore, the average frost roughness in the center and rear regions was used to represent the average frost roughness over the surface. The average frost equivalent sand-grain roughness increased with time until it reached a maximum height and then started decreasing. The time for the appearance of the average frost equivalent sand-grain roughness peak decreased if air temperature, relative humidity, and air velocity increased,

or wall temperature decreased. The peak value of frost equivalent sand-grain roughness became higher when air temperature, relative humidity, or wall temperature was higher, or air velocity was lower. Two empirical correlations were provided for predicting the maximum frost equivalent sand-grain roughness and its appearance time.

Once the evolution of the frost surface roughness was characterized, models were developed to estimate frost roughness parameters, including frost root-mean-square height, frost surface skewness, and frost equivalent sand-grain roughness height. Environmental conditions and frost roughness parameters were expressed in dimensionless form when generating these empirical correlations. Comparing the empirical correlation developed in this study of the frost equivalent sand-grain roughness with a previous predictive model, test surface geometry was found to play an important role in frost roughness formation. The empirical correlations presented in this study were valid for wall temperatures from -20 to -5°C, air temperatures from 16 to 8°C, relative humidity from 61 to 91%, and air velocities from 0.5 to 2.5 m s^{-1}.

To further investigate the evolution of frost surface roughness, the following recommendations should be considered for future work:

1. The geometry of test surface could play a noticeable role in the growth of frost surface roughness. Exploring the influence of different surface geometries is recommended. The tests in this study were for polished aluminum flat plate under forced convection. Many heat exchangers include aluminum fins and copper tubes. The tubes present a different geometry than studied here. Thus, studying frost in a tubular geometry may show differences to what was measured here.

This kind of studies could be helpful in revealing some of the geometrical influences affecting roughness.

2. The dew point temperatures of all the cases in this study were higher than the freezing point temperature. When the dew point is above the triple point of water, the mechanism of mass transfer from ambient air to the frost surface is different compared to when the dew point is below the freezing point. An extension of this work would be to conduct similar frost roughness experiments with the dew point temperature lower than the triple point of water to gain a better understanding of frost roughness formation.
3. The effect of surface wettability on frost roughness has not yet been explored. The distribution of the initial condensate water droplet can present very different patterns from the untreated surface used here. Hydrophilic surfaces produce droplets at small contact angles and are very crowed on a surface. In contrast, hydrophobic surfaces produce droplets at large contact angles that are widely separated from each other. It would be expected that the frost forming from these surfaces would potentially have different growth rates and roughness. Thus, to better characterize frost roughness on cold substrates should include tests over a with range of surface wettability.

BIBLIOGRAPHY

[1] M. Chen and W. Rohsenow, "Heat, mass, and momentum transfer inside frosted tubes—experiment and theory," *Journal of Heat Transfer,* vol. 86, no. 3, pp. 334-340, 1964.

[2] M. A. Dietenberger, "A simple and safe takeoff or landing procedure with wing surface contaminations," *Journal of Aircraft,* vol. 21, no. 12, pp. 955-961, 1984.

[3] D. O'Neal and D. Tree, "A review of frost formation in simple geometries," *Ashrae Transactions,* vol. 91, no. 2A, pp. 267-281, 1985.

[4] A. Leoni, M. Mondot, F. Durier, R. Revellin, and P. Haberschill, "Frost formation and development on flat plate: Experimental investigation and comparison to predictive methods," *Experimental Thermal and Fluid Science,* vol. 88, pp. 220-233, 2017.

[5] L. Huang, Z. Liu, Y. Liu, and Y. Gou, "Experimental study of frost growth on a horizontal cold surface under forced convection," *Journal of mechanical science and technology,* vol. 24, no. 7, pp. 1523-1529, 2010.

[6] R. Östin and S. Andersson, "Frost growth parameters in a forced air stream," *International Journal of Heat and Mass Transfer,* vol. 34, no. 4-5, pp. 1009-1017, 1991.

[7] D. O'Neal and D. Tree, "Measurement of frost growth and density in a parallel plate geometry," *Ashrae Transactions,* vol. 90, no. 2, pp. 278-290, 1984.

[8] K.-S. Lee, W.-S. Kim, and T.-H. Lee, "A one-dimensional model for frost formation on a cold flat surface," *International Journal of Heat and Mass Transfer,* vol. 40, no. 18, pp. 4359-4365, 1997.

[9] I. Tokura, H. Saito, and K. Kishinami, "Prediction of growth rate and density of frost layer developing under forced convectionBestimmung der Wachstumsgeschwindigkeit und der Dichte von bei Zwangskonvektion entstehenden Eisschichten," *Wärme-und Stoffübertragung,* vol. 22, no. 5, pp. 285-290, 1988.

[10] A. Z. Şahin, "An experimental study on the initiation and growth of frost formation on a horizontal plate," *EXPERIMENTAL HEAT TRANSFER An International Journal,* vol. 7, no. 2, pp. 101-119, 1994.

[11] A. Lüer and H. Beer, "Frost deposition in a parallel plate channel under laminar flow conditions," *International Journal of Thermal Sciences,* vol. 39, no. 1, pp. 85-95, 2000.

[12] Y. Lee and S. Ro, "Frost formation on a vertical plate in simultaneously developing flow," *Experimental Thermal and Fluid Science,* vol. 26, no. 8, pp. 939-945, 2002.

[13] M. Kandula, "Frost growth and densification in laminar flow over flat surfaces," *International Journal of Heat and Mass Transfer,* vol. 54, no. 15-16, pp. 3719-3731, 2011.

[14] C.-H. Cheng and C.-C. Shiu, "Frost formation and frost crystal growth on a cold plate in atmospheric air flow," *International Journal of Heat and Mass Transfer,* vol. 45, no. 21, pp. 4289-4303, 2002.

[15] C. J. Hermes, R. O. Piucco, J. R. Barbosa Jr, and C. Melo, "A study of frost growth and densification on flat surfaces," *Experimental Thermal and Fluid Science,* vol. 33, no. 2, pp. 371-379, 2009.

[16] A. Z. Şahin, "Effective thermal conductivity of frost during the crystal growth period," *International Journal of Heat and Mass Transfer,* vol. 43, no. 4, pp. 539-553, 2000.

[17] X. Wu, W. Dai, W. Xu, and L. Tang, "Mesoscale investigation of frost formation on a cold surface," *Experimental thermal and fluid science,* vol. 31, no. 8, pp. 1043-1048, 2007.

[18] H. Lee, J. Shin, S. Ha, B. Choi, and J. Lee, "Frost formation on a plate with different surface hydrophilicity," *International Journal of Heat and Mass Transfer,* vol. 47, no. 22, pp. 4881-4893, 2004.

[19] Y. Hayashi, A. Aoki, S. Adachi, and K. Hori, "Study of frost properties correlating with frost formation types," *Journal of heat transfer,* vol. 99, no. 2, pp. 239-245, 1977.

[20] P. T. Brian, R. C. Reid, and Y. T. Shah, "Frost deposition on cold surfaces," *Industrial & Engineering Chemistry Fundamentals,* vol. 9, no. 3, pp. 375-380, 1970.

[21] B. Jones and J. Parker, "Frost formation with varying environmental parameters," *Journal of Heat Transfer,* vol. 97, no. 2, pp. 255-259, 1975.

[22] Y.-X. Tao, R. Besant, and K. Rezkallah, "A mathematical model for predicting the densification and growth of frost on a flat plate," *International Journal of Heat and Mass Transfer,* vol. 36, no. 2, pp. 353-363, 1993.

[23] R. Le Gall, J. Grillot, and C. Jallut, "Modelling of frost growth and densification," *International Journal of Heat and Mass Transfer,* vol. 40, no. 13, pp. 3177-3187, 1997.

[24] A. El Cheikh and A. Jacobi, "A mathematical model for frost growth and densification on flat surfaces," *International Journal of Heat and Mass Transfer,* vol. 77, pp. 604-611, 2014.

[25] F. Breque and M. Nemer, "Frosting modeling on a cold flat plate: Comparison of the different assumptions and impacts on frost growth predictions," *International Journal of Refrigeration,* vol. 69, pp. 340-360, 2016.

[26] Y. Lee and S. Ro, "Analysis of the frost growth on a flat plate by simple models of saturation and supersaturation," *Experimental Thermal and Fluid Science,* vol. 29, no. 6, pp. 685-696, 2005.

[27] K. Qu, S. Komori, and Y. Jiang, "Local variation of frost layer thickness and morphology," *International journal of thermal sciences,* vol. 45, no. 2, pp. 116-123, 2006.

[28] D. L. da Silva, C. Melo, and C. J. Hermes, "Effect of frost morphology on the thermal-hydraulic performance of fan-supplied tube-fin evaporators," *Applied Thermal Engineering,* vol. 111, pp. 1060-1068, 2017.

[29] R. Kind and M. Lawrysyn, "Aerodynamic characteristics of hoar frost roughness," *AIAA journal,* vol. 30, no. 7, pp. 1703-1707, 1992.

[30] M. Bragg, D. Heinrich, W. Valarezo, and R. McGhee, "Effect of underwing frost on a transport aircraft airfoil at flight Reynolds number," *Journal of Aircraft,* vol. 31, no. 6, pp. 1372-1379, 1994.

[31] R. Yun, Y. Kim, and M.-k. Min, "Modeling of frost growth and frost properties with airflow over a flat plate," *International Journal of Refrigeration,* vol. 25, no. 3, pp. 362-371, 2002.

[32] S. Niroomand, M. Fauchoux, and C. Simonson, "Experimental characterization of frost growth on a horizontal plate under natural convection," *Journal of Thermal Science and Engineering Applications,* vol. 11, no. 1, p. 011020, 2019.

[33] T. Miyauchi, S. T. McClain, T. Zhang, D. L. O'Neal, and J. T. Riley, "Photogrammetric Frost Roughness Measurements in Cold-Soaked Conditions," SAE Technical Paper0148-7191, 2019.

[34] M. Smith, J. Carrivick, and D. Quincey, "Structure from motion photogrammetry in physical geography," *Progress in Physical Geography,* vol. 40, no. 2, pp. 247-275, 2016.

[35] J. Cui, W. Li, Y. Liu, and Z. Jiang, "A new time-and space-dependent model for predicting frost formation," *Applied Thermal Engineering,* vol. 31, no. 4, pp. 447-457, 2011.

[36] D. Kim, C. Kim, and K.-S. Lee, "Frosting model for predicting macroscopic and local frost behaviors on a cold plate," *International Journal of Heat and Mass Transfer,* vol. 82, pp. 135-142, 2015.

[37] X. Wu, F. Chu, and Q. Ma, "Frosting model based on phase change driving force," *International Journal of Heat and Mass Transfer,* vol. 110, pp. 760-767, 2017.

[38] J. Armengol, C. Salinas, J. Xaman, and K. Ismail, "Modeling of frost formation over parallel cold plates considering a two-dimensional growth rate," *International Journal of Thermal Sciences,* vol. 104, pp. 245-256, 2016.

[39] B. Na and R. L. Webb, "A fundamental understanding of factors affecting frost nucleation," *International Journal of Heat and Mass Transfer,* vol. 46, no. 20, pp. 3797-3808, 2003.

[40] J. Shin, A. V. Tikhonov, and C. Kim, "Experimental study on frost structure on surfaces with different hydrophilicity: density and thermal conductivity," *Journal of Heat Transfer,* vol. 125, no. 1, pp. 84-94, 2003.

[41] J. Hoke, J. Georgiadis, and A. Jacobi, "Effect of substrate wettability on frost properties," *Journal of thermophysics and heat transfer,* vol. 18, no. 2, pp. 228-235, 2004.

[42] A. Adamson, "Physical Chemistry of Surfaces, 5th edn Wiley," *New York,* 1990.

[43] L. Cai, R. Wang, P. Hou, and X. Zhang, "Study on restraining frost growth at initial stage by hydrophobic coating and hygroscopic coating," *Energy and Buildings,* vol. 43, no. 5, pp. 1159-1163, 2011.

[44] Z. Liu, Y. Gou, J. Wang, and S. Cheng, "Frost formation on a super-hydrophobic surface under natural convection conditions," *International Journal of Heat and Mass Transfer,* vol. 51, no. 25, pp. 5975-5982, 2008.

[45] A. Léoni, M. Mondot, F. Durier, R. Revellin, and P. Haberschill, "State-of-the-art review of frost deposition on flat surfaces," *International Journal of Refrigeration,* vol. 68, pp. 198-217, 2016.

[46] J. Iragorry, Y.-X. Tao, and S. Jia, "A critical review of properties and models for frost formation analysis," *HVAC&R Research,* vol. 10, no. 4, pp. 393-420, 2004.

[47] J. L. Hoke, J. Georgiadis, and A. Jacobi, "The interaction between the substrate and frost layer through condensate distribution," Air Conditioning and Refrigeration Center. College of Engineering …2000.

[48] B. Na and R. L. Webb, "Mass transfer on and within a frost layer," *International Journal of Heat and Mass Transfer,* vol. 47, no. 5, pp. 899-911, 2004.

[49] Y.-X. Tao and R. Besant, "Prediction of spatial and temporal distributions of frost growth on a flat plate under forced convection," *Journal of heat transfer,* vol. 115, no. 1, pp. 278-281, 1993.

[50] M. A. Dietenberger, "Generalized correlation of the water frost thermal conductivity," *International Journal of Heat and Mass Transfer,* vol. 26, no. 4, pp. 607-619, 1983.

[51] M. Kandula, "Frost growth and densification on a flat surface in laminar flow with variable humidity," *International Communications in Heat and Mass Transfer,* vol. 39, no. 8, pp. 1030-1034, 2012.

[52] S. Negrelli, V. S. Nascimento Jr, and C. J. Hermes, "A study of the effective thermal conductivity of frost formed on parallel plate channels," *Experimental Thermal and Fluid Science,* vol. 78, pp. 301-308, 2016.

[53] C. J. Hermes, "An analytical solution to the problem of frost growth and densification on flat surfaces," *International Journal of Heat and Mass Transfer,* vol. 55, no. 23-24, pp. 7346-7351, 2012.

[54] C. J. Hermes, F. R. Loyola, and V. S. Nascimento Jr, "A semi-empirical correlation for the frost density," *International Journal of Refrigeration,* vol. 46, pp. 100-104, 2014.

[55] W. Wang, Q. Guo, W. Lu, Y. Feng, and W. Na, "A generalized simple model for predicting frost growth on cold flat plate," *international journal of refrigeration,* vol. 35, no. 2, pp. 475-486, 2012.

[56] B. Na and R. L. Webb, "New model for frost growth rate," *International Journal of Heat and Mass Transfer,* vol. 47, no. 5, pp. 925-936, 2004.

[57] H. Schneider, "Equation of the growth rate of frost forming on cooled surfaces," *International Journal of Heat and Mass Transfer,* vol. 21, no. 8, pp. 1019-1024, 1978.

[58] A. D. Sommers, C. W. Gebhart, and C. J. Hermes, "The role of surface wettability on natural convection frosting: Frost growth data and a new correlation for hydrophilic and hydrophobic surfaces," *International Journal of Heat and Mass Transfer,* vol. 122, pp. 78-88, 2018.

[59] D. Shaw and B. Mason, "XXIX. The growth of ice crystals from the vapour," *The London, Edinburgh, and Dublin Philosophical Magazine and Journal of Science,* vol. 46, no. 374, pp. 249-262, 1955.

[60] T. Kobayashi, "On the habit of snow crystals artificially produced at low pressures," *Journal of the Meteorological Society of Japan. Ser. II,* vol. 36, no. 5, pp. 193-208, 1958.

[61] T. Gonda, "The growth of small ice crystals in gases of high and low pressures," *Journal of the Meteorological Society of Japan. Ser. II,* vol. 54, no. 4, pp. 233-240, 1976.

[62] K. G. Libbrecht, "The physics of snow crystals," *Reports on progress in physics,* vol. 68, no. 4, p. 855, 2005.

[63] Y. Hayashi, K. Aoki, and H. Yuhara, "Study of frost formation based on a theoretical model of the frost layer," *Heat Transfer-Japanese Research,* vol. 6, no. 3, pp. 79-94, 1977.

[64] Y. Chen, P. Lu, C. Shen, and Q. Zhang, "Experimental study on frost formation on a cold surface in low atmospheric pressure," *Applied Thermal Engineering,* vol. 90, pp. 86-93, 2015.

[65] V. S. Nascimento Jr, F. R. Loyola, and C. J. Hermes, "A study of frost build-up on parallel plate channels," *Experimental Thermal and Fluid Science,* vol. 60, pp. 328-336, 2015.

[66] K. Kim, J.-S. Kim, and K.-S. Lee, "Characteristics of frost formation on two-dimensional fins and its empirical correlations," *International Journal of Heat and Mass Transfer,* vol. 53, no. 13-14, pp. 2670-2675, 2010.

[67] M. Song and C. Dang, "Review on the measurement and calculation of frost characteristics," *International Journal of Heat and Mass Transfer,* vol. 124, pp. 586-614, 2018.

[68] S. Lee, A. Broeren, H. Addy, R. Sills, and E. Pifer, "Development of 3D ice accretion measurement method," in *4th AIAA Atmospheric and Space Environments Conference*, 2012, p. 2938.

[69] P. Hariharan, *Optical Interferometry, 2e*. Elsevier, 2003.

[70] A.-s. Wang, B. Xie, and Z.-w. Liu, "Design of measurement system of 3D surface profile based on chromatic confocal technology," in *2017 International Conference on Optical Instruments and Technology: Optical Systems and Modern Optoelectronic Instruments*, 2018, vol. 10616, p. 1061618: International Society for Optics and Photonics.

[71] K. Mikkelsen, R. MCKNIGHT, R. RANAUDO, and J. PERKINS, P, "Icing flight research-Aerodynamic effects of ice and ice shape documentation with stereo photography," in *23rd Aerospace Sciences Meeting*, 1985, p. 468.

[72] P. Collier, L. Dixon, D. Fontana, D. Payne, and A. Pearson, "The use of close range photogrammetry for studying ice accretion on aerofoil sections," *The Photogrammetric Record,* vol. 16, no. 94, pp. 671-684, 1999.

[73] K. A. Flack and M. P. Schultz, "Review of hydraulic roughness scales in the fully rough regime," *Journal of Fluids Engineering,* vol. 132, no. 4, p. 041203, 2010.

[74] ASHRAE, "ASHRAE Handbook—HVAC Systems and Equipment," ed: ASHRAE Atlanta, GA, 2008.

[75] T. Ferreira and W. Rasband, "ImageJ user guide," *ImageJ/Fiji,* vol. 1, pp. 155-161, 2012.

[76] T. Zhang, D. L. O'Neal, and S. T. McClain, "Analysis of frost thickness and roughness growth from the perspective of frost crystal structure," *International Journal of Refrigeration,* vol. 112, pp. 314-323, 2020.

[77] A. Mason, A. PhotoScan, I. Photos, A. Photos, B. D. Cloud, and B. Mesh, "Making 3D models with photogrammetry," ed: Carleton College, 2017.